Reflective Impulse Radios: Principles and Design

Yuhui David Chen

Electrical Engineering and Computer Sciences
University of California at Berkeley

Technical Report No. UCB/EECS-2013-137
http://www.eecs.berkeley.edu/Pubs/TechRpts/2013/EECS-2013-137.html

August 4, 2013

Reflective Impulse Radios: Principles and Design

by

Yuhui Chen

A dissertation submitted in partial satisfaction of the
requirements for the degree of
Doctor of Philosophy

in

Electrical Engineeing and Computer Sciences

in the

GRADUATE DIVISION
of the
UNIVERSITY OF CALIFORNIA, BERKELEY

Committee in charge:
Professor Jan Rabaey, Chair
Professor Anant Sahai
Professor Robert Knight

Fall 2013

Reflective Impulse Radios: Principles and Design

Abstract

Reflective Impulse Radios: Principles and Design

by

Yuhui Chen
Doctor of Philosophy in Electrical Engineeing and Computer Sciences

University of California, Berkeley

Professor Jan Rabaey, Chair

Emerging wireless sensor networks display a severe asymmetry between the up and down links. An alternative communication architecture, *reflective impulse radio,* is proposed to address such design challenges. It operates from the principles of passive transmission and pulse based modulation, readily used in radio frequency identification (RFID) and ultra wide-band (UWB) technologies respectively. By employing both schemes in conjunction however, it achieves ultra low power consumption and high data rate simultaneously.

This dissertation begins by examining future wireless sensor applications and presenting the link asymmetry. The alternative architecture is then introduced and its operation principles explained. A step-by-step design procedure follows, accompanied by the implementation of a miniature biomedical implant transmitter as a design example. Potential challenges and mitigation techniques are also discussed. Key advantages of the proposed architecture include ultra low power consumption, simple circuitry (hence high reliability and low cost), and broad range of scalability. Measurement results of the biomedical example are subsequently presented, before a short conclusion is given in the end.

While originated for wireless sensor networks, the proposed architecture can be applied to many other applications facing similar communication challenges.

To the most important people in my life —
parents, wife, and daughter.

Contents

Contents ii

List of Figures iv

List of Tables vii

1 Introduction 1
- 1.1 Wireless Sensor Networks . . . 2
  - 1.1.1 Implantable Neural Transmitter . . . 2
  - 1.1.2 Link Asymmetry . . . 5
- 1.2 Thesis Outline . . . 7

2 Principles 8
- 2.1 RFID and UWB . . . 9
  - 2.1.1 RFID . . . 9
  - 2.1.2 UWB . . . 10
- 2.2 Reflective Impulse Radios . . . 14
  - 2.2.1 Principles . . . 14
  - 2.2.2 Circuit Diagram . . . 18
- 2.3 Direct Antenna Modulation . . . 19
- 2.4 Range of Applicability . . . 22
  - 2.4.1 Power Consumption . . . 22
  - 2.4.2 Hidden Power . . . 27
  - 2.4.3 Total Equivalent Power . . . 31
  - 2.4.4 Reflective Impulse Radio vs. RFID . . . 32
  - 2.4.5 Reflective Impulse Radio vs. UWB . . . 39
  - 2.4.6 Summary . . . 44

3 Design **47**
3.1 BER and Link Budget 47
3.1.1 Path Loss 48
3.1.2 SNR 50
3.1.3 Self Interference 52
3.1.4 Example 53
3.2 Antenna Switch 55
3.2.1 Switch Size and Modulation Depth 55
3.2.2 Resistive vs. Capacitive Modulation 56
3.2.3 Example 58
3.3 Pulse Generator 59
3.3.1 Delay Line Pulse Generator 61
3.3.2 Example 62
3.4 PPM Encoder 65
3.4.1 Pass Transistor PPM Encoder 65
3.4.2 Example 65
3.5 RIR Receiver 67
3.5.1 Self Interference Cancellation 69
3.5.2 Phase Noise 72
3.5.3 Suggestions for Future Research 75

4 Results **77**
4.1 System Design 78
4.1.1 Two-Phase Operation 79
4.1.2 Regulator-Transmitter Co-Design 80
4.2 Transmitter Implementation 83
4.3 Test Results 83
4.3.1 Receiver Architecture 84
4.3.2 Functional Test 85
4.3.3 Range Test 89
4.3.4 Energy Efficiency Test 93
4.4 Future Improvement 95

5 Conclusion **99**

Bibliography **102**

List of Figures

1.1 Illustration of a Future Brain Machine Interface Application [7] 3
1.2 Microscopic Images of a Neural Implant Site after 2, 4, 6 and 12 Weeks (A–D, respectively) [8] 4

2.1 Link Asymmetry in Wireless Sensor Networks 8
2.2 RFID in Use [18] 10
2.3 Block Diagram of a Simple Spark-Gap Transmitter from a 1917 Boy's Book [19] 11
2.4 Minimum Energy per Bit versus Normalized Signal Bandwidth . 13
2.5 Operating Principles of Reflective Impulse Radios 15
2.6 Spectrum of Reflective Wave 17
2.7 Block Diagram of a Reflective Impulse Transmitter 19
2.8 Direct Antenna Modulation Experiment [30] 20
2.9 Definition of Pulse Repetition Time and Number of Pulse Positions 22
2.10 Forms of Pulse Generator Output 24
2.11 Function of a PPM Encoder 25
2.12 Buffer Driver 27
2.13 Device Powering Scenarios 29
2.14 Power Flow of an RF-Powered Wireless Device 30
2.15 Transmitter Power versus Number of PPM Pulse Positions . . . 32
2.16 Reflective Impulse Radio versus RFID 34
2.17 Power Comparison between Reflective Impulse Radio and RFID 38
2.18 Reflective Impulse Radio versus UWB 40
2.19 Power Comparison: Reflective Impulse Radio vs. UWB 43
2.20 Transmitter Power Comparison among Reflective Impulse Radio, UWB and RFID 45

3.1 Carrier and Signal Power in Reflective Impulse Radio 48
3.2 Definition of Modulation Depth 49
3.3 Total Path Loss in Reflective Impulse Radios 50
3.4 Theoretical Probability of Error versus SNR for M-ary PPM [35] 52
3.5 Phase Noise before and after Interference Cancellation 53
3.6 Combined Channel and Antenna Loss versus Frequency [36] . . 54
3.7 Modulation Depth vs. Switch Resistance 57
3.8 Resistive vs. Capacitive Antenna Modulation 58
3.9 Antenna Equivalent Circuit 59
3.10 Transient Responses of Resistive and Capacitive Modulations . . 59
3.11 Device Sizing Example 60
3.12 Delay Line Example 61
3.13 Timing Diagram of a Delay Line Based Pulse Generator 62
3.14 Example of Differential Inverter and RS Flip-flip Implementation 63
3.15 Simulated Waveforms of an Example Pulse Generator 64
3.16 Simulated Pulse Width Variation and Mismatch 65
3.17 Pass Transistor PPM Encoder Schematic 66
3.18 Layout of a Pass Transistor PPM Encoder 67
3.19 Reflective Impulse Transmitter Block Diagram 68
3.20 Simplified Block Diagram of a Reflective Impulse Receiver . . . 69
3.21 Interference Suppression vs. Phase and Amplitude Imbalance [37] 70
3.22 Phase Noise Experiment with Single Path Interference 73
3.23 Phase Noise Results with Single Path Interference 74

4.1 System Diagram of the mm-scale Neural Transponder 78
4.2 Timing Diagram of the Two-Phase Operation 80
4.3 Photo of the mm-scale Neural Transponder 82
4.4 Data Transmitter Block Diagram 83
4.5 Data Transmitter Layout 84
4.6 Reflective Impulse Receiver Diagram 85
4.7 Pulse Decoder Algorithm 86
4.8 Waveforms from Direct Transmitter Measurement 86
4.9 Overlay of Pulse Waveforms 88
4.10 Pulses Received in Over-the-Air Test 88
4.11 Setup for Power Back-off Test 90
4.12 Receiver Decoder Output at Various Power Back-off Levels . . . 90
4.13 Setup for Direct Range Test 91

4.14 Receiver Decoder Output at Various Communication Distance . 92
4.15 Communication Distance vs. Reader Output Power 92
4.16 Transmitter Power Consumption vs. Data Rate 93
4.17 Reader Power Profile Example 94
4.18 Decoder Algorithm Current vs. Ideal 97

5.1 Progression of Radio: Timeline and Size Comparison [51] 101

List of Tables

1.1 Key Challenges of Implantable Neural Transmitters 5

2.1 Comparison of RFID and UWB Technologies, data sources: [18, 22, 23], *etc* 14
2.2 Device Powering Scenarios and Cost of Hidden Power 28
2.3 Example Parameters for Transmitter Power Optimization 32
2.4 UHF RFID Regulatory Status in Selected Countries and Regions [32] 33
2.5 Power Components of Reflective Impulse Transmitter and RFID Transponder 37
2.6 Example Parameters for Power Comparison 44

3.1 Simulated Pulse Width and Power Consumption of an Example Pulse Generator 64

4.1 Comparison with State-of-the-Art Neural Transmitters 96

Chapter 1

Introduction

This thesis is about another type of radios. But one may wonder that from 2G, 3G and 4G cellular to Bluetooth, Zigbee, and WiFi standards in a, b, g, n, there seem already enough wireless creations in this busy world. So —

Why another radio?

Fast forward 15 years. It is conceivable that the world we live in will be "smarter." Clothes that we wear will not only keep us warm but also monitor our heart beat, blood pressure, and glucose level. When the numbers don't read right, our doctors will be alerted immediately. Also imagine that our houses will be intelligent enough to refuse turning on the air conditioner when a window is wide open, and that society's aging infrastructure such as power cables and gas pipes can perform self diagnosis before catastrophic breakdowns occur. It will be a world where physical sensors — medical, chemical, environmental, mechanical, etc. — are pervasively deployed. Moreover, these sensors will be equipped with an ability to communicate, over wirelines but more frequently over wireless links. It will be a world with ubiquitous wireless sensor networks.

1.1 Wireless Sensor Networks

To understand the characteristics of future wireless sensor networks, it is helpful to examine one or two actual applications as a case study. We will then extract some common architectural features and design requirements applicable to most other wireless sensor networks. So it is less important which example we choose; rather the example we choose should be representative enough to illustrate the common features of other applications. And our choice is —

1.1.1 Implantable Neural Transmitter

It is reported that millions of world's population suffer from paralysis, caused by severe damage to the central nervous system. For instance, traumatic spinal cord injury alone accounts for nearly 11,000 new cases of permanent paralysis in the United States. About half of those injured suffer from quadriplegia, unable to move their muscles below the neck [1, 2].

Different directions have been taken to help quadriplegics regain their motor function. One of the approaches under research is neuroprosthesis. Proposed by Edward Schmidt in 1980 [3], the basic concept is to sense the neural signals in the brain's motor cortex, interpret from the recordings the patient's intention, then control a prosthetic device (e.g. a robot arm) to perform the intended movement. Because it bypasses the injured spinal cord altogether, this proposed approach, termed *Brain Machine Interface* or *Brain Computer Interface*, has gathered much attention in the past 10 years from various research communities [2, 4, 5, 6, 7].

Figure 1.1 provides a graphic rendering of the futuristic use scenario [7]. Controlled by the portable device on the back, the man-made prothesis restores much of the function of the gentleman's left arm. Input to the controller is sent wirelessly from the neural sensors implanted to the patient's brain. These neural signals are then mapped to the intention of the motor cortex, which moves the arm and fingers accordingly. Finally through visual and possibly other (e.g. positional and tactile) feedback, the brain will make further adjustment, closing the feedback control loop. In other words, the patient is able to control his new arm by simple thoughts — just like the most of us.

Figure 1.1: Illustration of a Future Brain Machine Interface Application [7]

Apparently the wireless interface in this neural example is more than desirable. It is unimaginable that there would be cables through skin, tissue and skull, wiring the implanted sensor to the controller. Challenges to the wireless interface, on the other hand, are not minor either. There are mainly three of them: **size**, **power**, and **data rate**.

(1) Size

Because neural sensors are implanted to the brain, they can cause damage to the surrounding tissue. It has been demonstrated that the micro motion between an electrode and brain tissue results in a scar-like sheath that isolates the electrode from the brain [8]. Over the course of several months or even weeks, the electrode collects weaker and weaker signals until it completely fails. Shown in Figure 1.2 C and D, the voids of tissue are clearly visible 6–12 weeks after initial implanting.

For the fact that neuroprosthesis is a relative young field, most neural elec-

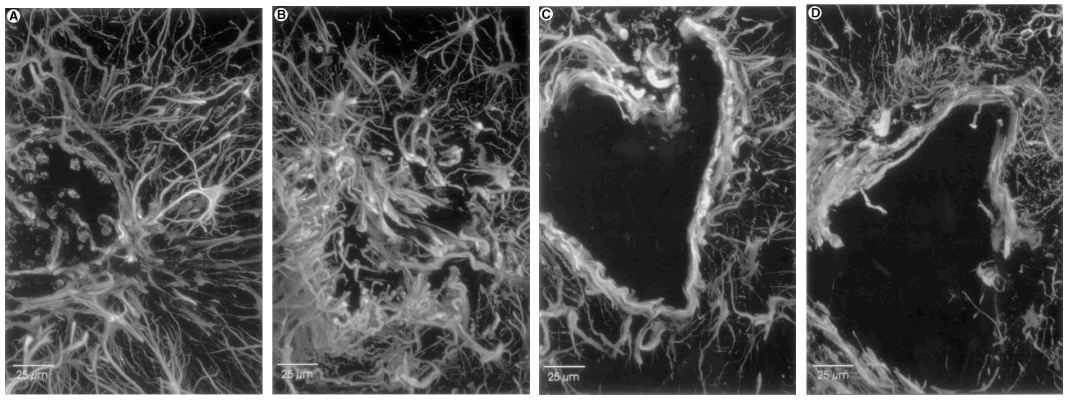

Figure 1.2: Microscopic Images of a Neural Implant Site after 2, 4, 6 and 12 Weeks (A–D, respectively) [8]

trodes are not yet equipped with the desirable wireless interface. However, early development has begun [9, 10, 11, 12]. Sizes of these wireless electrode arrays range from 4.7×5.9 mm^2 [9] to 40×50 mm^2 [11], limited primarily by the size of antenna and electronic circuits responsible for signal acquisition, data transmission and power delivery. The larger the electrode array, the more micro-motion friction it can cause. It is therefore highly desirable to significantly reduce the form factor of these arrays down to, for example, 1×1 mm^2. Another benefit of smaller electrodes is that they provide more flexibility in choosing the recording site and recording density.

(2) Power

One major implication of the smaller size is reduced amount of power available for electronic circuits. Detailed in [13], energy scavenging technologies — thermal, biochemical and mechanical — all fail to deliver meaningful power at 1x1 mm^2. Neither do current battery technologies have the energy density required for maintenance-free operation over the implant's lifetime, which should ideally be well over 10 years. The most promising approach to power delivery is through electromagnetic coupling. Constrained by the size, safety regulations and the electromagnetic characteristics of bones and brain tissue, maximum amount of power available is 5–10 μW (in DC, direct current) [13]. Note that this is the total power available to all electronics on the sensor, allowing only

a small fraction (e.g. $\leqslant$1 μW) for data communication.

(3) Data Rate

Neural signals are in the form of voltage spikes. To capture the entire waveform from a single electrode, it requires sampling rate of 15–20 kSample/s at 5–10 bits of resolution, equivalent up to 200 kbps of data rate [9, 14]. Additionally, electrodes are 200–400 μm apart [9, 14], allowing 9–25 of them in a 1x1 mm^2 area. Therefore, raw data rate from the small neural sensor can be as high as 5 Mbps. For 3D electrodes like in [14], multiple recording sites reside on a single electrode, demanding even higher data rate.

Table 1.1 below summarizes these key challenges.

Size	Power	Data Rate
1x1 mm^2	$\leqslant$1 μW	0.7–5 Mbps

Table 1.1: Key Challenges of Implantable Neural Transmitters

While above challenges exist for the implanted neural transmitter, it is important to note that the scenarios are quite different for the off-body receiver (the belt worn device in Figure 1.1), which can afford orders of magnitude more power and space. Such link asymmetry actually exists in a wide range of other wireless sensor applications — a topic for discussion in the section below.

1.1.2 Link Asymmetry

As mentioned previously, the biomedical example was chosen because it represented the architectural features and design challenges common to most other wireless sensor networks. To illustrate this, consider following two additional examples. The first is a "smart building" application for energy efficiency; the second is a "smart tire" application to enhance driving safety. As different they may seem like, it will become evident that the severe link asymmetry between the transmitter and the receiver exists in these two examples too.

Energy Efficiency. In the "smart environment" scenario [15, 16], sensors are deployed throughout a building to monitor temperature and brightness. Air conditioning and lighting will be automatically adjusted based on real-time electricity pricing while minimizing impact to building occupants' comfort level. These environmental sensors are sometimes located in hard-to-access places. They ideally need to be self sustainable for many years, requiring ultra low power consumption. On the other hand, the receiver that these sensors communicate to is often plugged into the electricity outlet, big and powerful.

Automotive. In the "smart tire" application [17], sensors are embedded along the inner liner of a tire to collect information on pressure, temperature, tire deformation, etc. Data from all four tires are transmitted towards a central coordinator to improve safety and enhance driving experience. These embedded transmitters need to be small and light-weight, so that they do not impact the balance of the tire. They also need to be energy efficient, requiring no maintenance between tire changes. Their aggregated data rate needs to be up to tens of mega bits per second (Mbps). Housed in the wheel well above the tire, the receiver on the other hand is powered directly from the drive train. Neither is its size — as long as it fits the wheel well — of primary concern. Infrequently commands need to be sent from the central coordinator to the embedded sensors. But they are on the order of kilo bits per second (kbps), if not less.

In these and other examples, a common feature is that a number of size-limited, energy-constrained wireless transmitters are connected in a star-like configuration. At the center of the star is a powerful receiver. Any systemic arrangement that can shift power and complexity burdens from a transmitter to the receiver is a much worthwhile trade. It is precisely the recognition of this tradeoff that inspired the design of *Reflective Impulse Radios*, an alternative communication architecture that promises orders of magnitude of power reduction over conventional solutions.

It is not just another radio.

1.2 Thesis Outline

This thesis is organized into five chapters.

After this introduction, principles of the proposed radio architecture will be explained in Chapter 2. Reflective Impulse Radios operate under passive transmission and pulse-based modulation schemes, combining the principles of radio frequency identification (RFID) and ultra wide-band (UWB) technologies. Main advantage of the proposed architecture is the combined benefits of both existing technologies. Another advantage is the expansion of the effective bandwidth of the antenna. All these will be detailed in Chapter 2, including a brief discussion on bidirectional communication links. Chapter 3 describes the step-by-step design procedure, accompanied in each step by the implantable transmitter example introduced earlier in this chapter. It begins with link budget estimation, followed by the design of antenna switch, pulse generator, and pulse position encoder. Design of reflective impulse receivers is treated in the end of Chapter 3. Chapter 4 exhibits actual measurement data from the neural transmitter example. Basic functions and superior performance are demonstrated. Another feature of the proposed architecture is excellent scalability, evidenced in the neural example as well. Finally, a conclusion about reflective impulse radios is given in Chapter 5.

A bibliography is included in the appendix.

Chapter 2

Principles

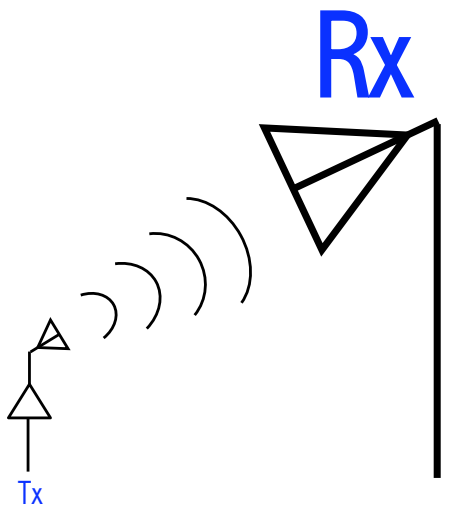

Figure 2.1: Link Asymmetry in Wireless Sensor Networks

In last chapter, a salient feature of many wireless sensor networks was displayed — there exists a severe asymmetry between the transmitter and receiver.

This can be better illustrated with the simple cartoon in Figure 2.1. While the small transmitter ("Tx") is energy starved, the receiver ("Rx") is large and powerful. The design objective therefore is to minimize the power consumption of the transmitter, even at the expense of the receiver.

There exist two architectures that handle the Tx-Rx tradeoff reasonably well: radio frequency identification (RFID) and impulse ultra wide-band (UWB) radios. This chapter will first examine the advantages and disadvantages of these two technologies, then introduce an alternative reflective impulse radio (RIR) architecture, which combines the operations — and the benefits — of RFID and UWB. Comparisons will later be drawn to specify a range of applicability within which the proposed architecture achieves better performance than both RFID and UWB. Finally, by directly modulating the antenna, the RIR radio also extends the effective bandwidth of the antenna, a phenomenon to be described later in this chapter.

2.1 RFID and UWB

2.1.1 RFID

Radio frequency identification (RFID) is a technology that allows an object, the so-called "tag", to be identified without making physical contact to the detector, or the "reader" (Figure 2.2). In most systems, the tag is completely passive, carrying no battery or other power sources. Its manufacturing cost can therefore be very low and its form factor be very flexible. Typical applications of RFID include inventory management, ticketing, security, transportation, and beyond.

A passive RFID tag receives its power from the reader via electromagnetic coupling (including electric-only and/or magnetic-only coupling in near field). Data are transmitted from the tag to the reader via a technique termed *"backscattering,"* also referred as *"load modulation"* in near field coupling. By modulating the antenna's impedance, the tag changes the reflected radio wave at the reader's side without actively transmitting an RF signal. It therefore

Figure 2.2: RFID in Use [18]

needs no mixer or power amplifier, significantly reducing its cost, complexity and power consumption. A major shortcoming of RFID however is limited data rate. A tag typically stores several bytes to a few kilo-bytes of data, transmitted over half to several seconds of time [18], far short of the Mbps data rate required by emerging wireless sensor applications.

2.1.2 UWB

The history of what is known today as "ultra wide-band" or UWB can be traced all the way back to the times of Heinrich Hertz (1857-1894) and Guglielmo Marconi (1874-1937). Both gentlemen experimented something called "spark-gap radios," which sent out a pulse of electromagnetic wave every time the transmitter sparked (Figure 2.3). Because sparks existed only in short time durations, their frequency-domain footprint had quite wide bandwidth (hence UWB). Beyond lab experiments, these early-day radios found their use in commercial applications too. In a famous incident, the spark-gap receiver on RMS Titanic failed to hear the warning messages from another steamship due to these radios' inherently poor interference rejection, partially responsible

for her tragic sinking in 1912 [19].

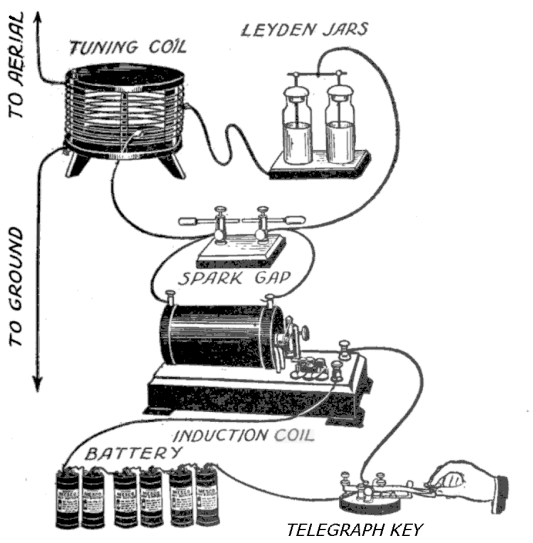

Figure 2.3: Block Diagram of a Simple Spark-Gap Transmitter from a 1917 Boy's Book [19]

Modern-day UWB impulse radios are proposed for short-range communications only. Their spectral emissions are also regulated below other radios' noise floor to avoid the interference issue. From theoretic and practical points of view, an impulse transmitter can achieve low power consumption because of following two reasons:

(1) it trades spectral efficiency for energy efficiency;

(2) it operates under heavy duty cycle.

Both points will now be elaborated.

From information theory, Shannon's channel capacity theorem states that

$$C = B \times \log_2 \left(1 + \frac{E_b \times R}{N_0 \times B}\right) \tag{2.1}$$

where C is the channel capacity, B the signal bandwidth, E_b is the energy per bit received, R the information data rate, and finally N_0 the noise spectral density, which is assumed additive and white Gaussian in the theorem [20]. Please note that although E_b is the energy per bit at the receiver side, it is generated by the transmitter hence costs power consumption to the transmitter, not the receiver. Given that

$$C \geqslant R \tag{2.2}$$

it can be derived that

$$\frac{E_b}{N_0} \geqslant \frac{B}{R}\left(2^{\frac{R}{B}} - 1\right) \tag{2.3}$$

Now define

$$\left(\frac{E_b}{N_0}\right)_{min} \triangleq \frac{B}{R}\left(2^{\frac{R}{B}} - 1\right) \tag{2.4}$$

In above Equation (2.4), the left term $\left(\frac{E_b}{N_0}\right)_{min}$ is the minimum amount of energy per bit (normalized to noise). $\frac{B}{R}$ on the right side is the signal bandwidth normalized to information data rate. This relation is plotted in Figure 2.4. As can be seen, the minimum energy per bit decreases when the normalized bandwidth increases. In other words, there exists a tradeoff between energy efficiency and spectral efficiency. The energy per bit value of the dotted asymptote in Figure 2.4 is $\ln 2$ ($= 0.69$), the absolute minimum demanded by the Shannon Theorem.

Above energy-bandwidth tradeoff addresses the core advantage of impulse UWB transmitters. Narrow-band radios typically require a bandwidth that is only a fraction of the data rate, corresponding to the steep portion of the curve in Figure 2.4. An impulse transmitter, on the other hand, sends signals in the form of narrow pulses hence takes up much wider bandwidth. The required transmission energy, according to Figure 2.4, is much lower. Although a UWB receiver usually consumes considerably higher power in synchronizing, correlating and detecting those narrow pulses, it is again the power of the transmitter that is of utmost concern for future wireless sensor applications. The receiver is much larger and can afford more power.

The other reason why impulse UWB transmitters achieve low power consumption is a practical one. Because a UWB transmitter sends signals in short pulses, most of its circuits can be shut off during the time when it is not

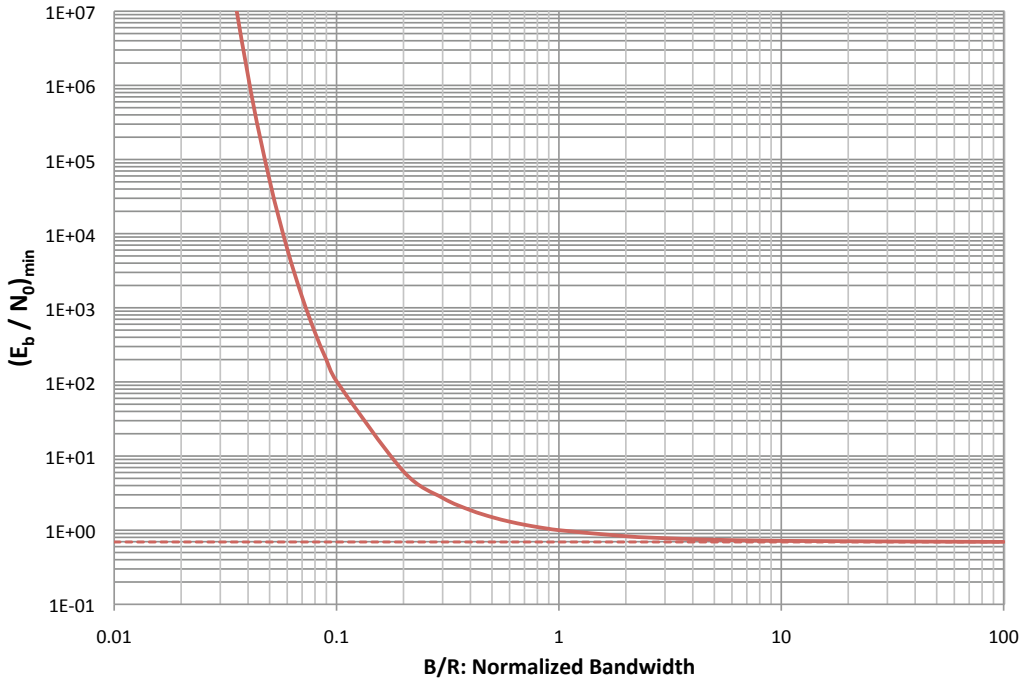

Figure 2.4: Minimum Energy per Bit versus Normalized Signal Bandwidth

transmitting. Narrow-band transmitters, on the other hand, need to keep all elements — oscillator, mixer, power amplifier — continuously on. This difference in duty cycle contributes to significant power saving on the transmitter side, especially when the data rate is relatively low in comparison to the signal bandwidth (again, the flat portion of the curve in Figure 2.4).

With both theoretical and practical reasons for high energy efficiency, an impulse UWB transmitter still consumes more power than an RFID transponder, because it is after all an active transmitter that employs an active power amplifier. Its competitive advantage on the other hand is the substantially higher data rate, making it comparable to an RFID transponder on the energy per bit basis, as summarized in Table 2.1. As we later on derive the mathematical models of their power consumption in Section 2.4, comparative results in Table 2.1 will be further corroborated.

	Power	Data Rate
RFID	<5 μW	up to several hundred kbps
UWB	>0.6 mW	up to 500 Mbps

Table 2.1: Comparison of RFID and UWB Technologies, data sources: [18, 22, 23], *etc*

2.2 Reflective Impulse Radios

Comparing Table 2.1 above to Table 1.1 in Chapter 1, one may quickly realize that neither RFID nor UWB satisfies the requirements for implantable neural applications. Even for other wireless sensor networks in general, it is highly desirable to combine the low power feature of RFID with the high data rate of UWB. The question is —

How?

2.2.1 Principles

Reflective Impulse Radio (RIR) is an alternative wireless communication architecture. It combines the operations and advantages of RFID and UWB, achieving high data rate and low power consumption simultaneously. Its operating principles are now detailed.

Figure 2.5 illustrates the simple operation of a reflective impulse transmitter. The solid black wave on the top represents a single-tone, continuous-wave sinusoid incident on the transmitter's antenna. This wave is typically generated by the receiver or "reader" in RFID terminology. Also similar to an RFID tag, there is a switch across the transmitter antenna. The red rectangle waveform represents the control signal of the antenna switch. When the switch is turned on and off, there are different waves reflected back from the antenna, shown as gray dotted curves in Figure 2.5. At the on-state (from t_1 to t_2 and from t_3 to t_4) for example, the antenna is mismatched to the rest of the transmitter circuit. Therefore majority of the incident wave is reflected back to the receiver. At the off-state (at $t < t_1$, from t_2 to t_3, and $t > t_4$), antenna is better matched to the circuit hence less wave is reflected back. (Please note

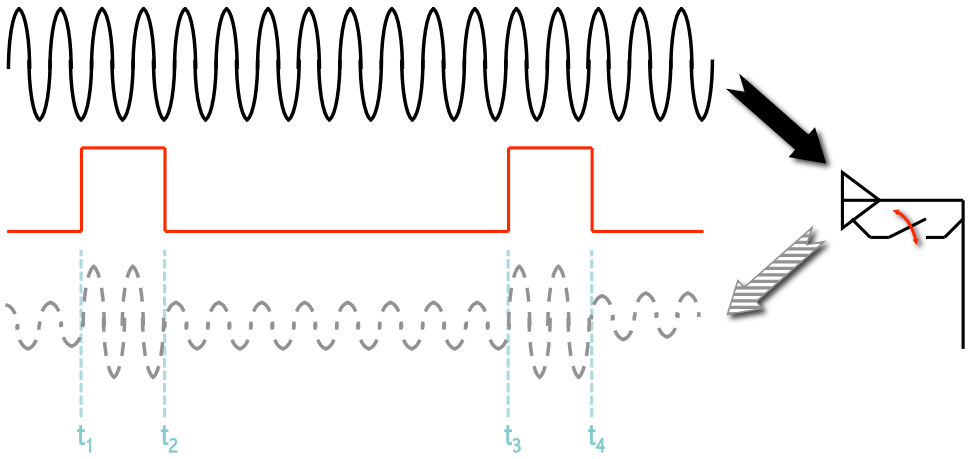

Figure 2.5: Operating Principles of Reflective Impulse Radios

that even under perfect power matching conditions, there is still 50% power of the incident wave getting reflected.) By modulating the timing of the on-off signal, one can encode base-band data into this passive radio transmitter.

Above description deviates little from the backscattering operation of an RFID tag. Key difference however exists in the width of the control signal in Figure 2.5. In an RFID systems, narrow-band modulation schemes (such as Amplitude Shift Keying ASK, Frequency Shift Keying FSK, Phase Shift Keying PSK) are employed. Therefore the control signal's on-time duration ($[t_1, t_2]$ and $[t_3, t_4]$) is rather long. In a reflective impulse radio (RIR), the on-time is much shorter. It is in fact so short that the red waveform in Figure 2.5 is more like a sequence of narrow pulses (they are drawn as wide rectangles only for the convenience of illustration). The spectral bandwidth of the control signal far exceeds the information data rate, to take advantage the energy-bandwidth tradeoff in Equation (2.4). As a result the receiver of an RIR radio requires much broader bandwidth than that of an RFID.

One may wonder — what prevents an RFID from operating with shorter on-time durations? The answer is spectral regulation, which will be discussed in length in Section 2.4.4 "Reflective Impulse Radio vs. RFID." In essence, to ensure coexistence of multiple radio systems, spectral regulation mandates that

the transmitted power from each radio should be either high power at narrow bandwidth or low power at wide bandwidth. There is no allowance for the "middle ground;" or cross-radio interference will occur. It is also worth mentioning that multiple proposals have been made in recent years that effectively expand the bandwidth of conventional RFIDs. In [24, 25, 26] for example, code division multiple access (CDMA) transmission schemes were proposed for active and semi-active RFID tags to avoid channel collision when there was a need to access a large number of tags simultaneously. While the bandwidth of these systems was indeed made larger than those with conventional coding schemes (e.g. Manchester), their purpose was to manage media access control (MAC) as opposed to power efficiency. As a matter of fact the complexity of CDMA encoding prevents those tags from operating completely passively, losing their power appeal for energy-constrained systems. This and other aspects of the difference between RFID and RIR will be further discussed in Section 2.4.4, where mathematical comparisons between their power consumption and data rate will be provided as well.

Let us now analyze the spectral content of the reflective wave. The gray curve in Figure 2.5 is composed of two parts superimposed: a constant-amplitude sinusoid and a pulsed sinusoid (Figure 2.6a). Spectral representation of the first sinusoid is simply an impulse function at the frequency of the incident carrier (the gray-color impulse in Figure 2.6c, where f_C denotes carrier frequency). The pulsed sinusoid on the other hand can be further decomposed to the product of another constant-amplitude sinusoid and a rectangle wave that pulsates between 0 and 1 (Figure 2.6b). Spectral representation of the constant-amplitude sinusoid is again another impulse; that of the rectangle wave is a $sinc(x)$ $(= sin(x)/x)$ function. Because multiplication in the time domain corresponds to convolution in the frequency domain, spectrum of the pulsed sinusoid is therefore the same *sinc* function from the rectangle wave but with its center shifted to f_C (gray lobes in Figure 2.6c). Frequency parameters in Figure 2.6c can be related to time parameters in Figure 2.5 by the following equation

$$... = f_2 - f_1 = f_1 - f_C = f_C - f_{-1} = ... = \frac{1}{t_2 - t_1} = \frac{1}{t_4 - t_3} = ... \qquad (2.5)$$

Finally the black impulse in Figure 2.6c, coincident with the gray impulse described earlier, represents the solid-black incident wave in Figure 2.5.

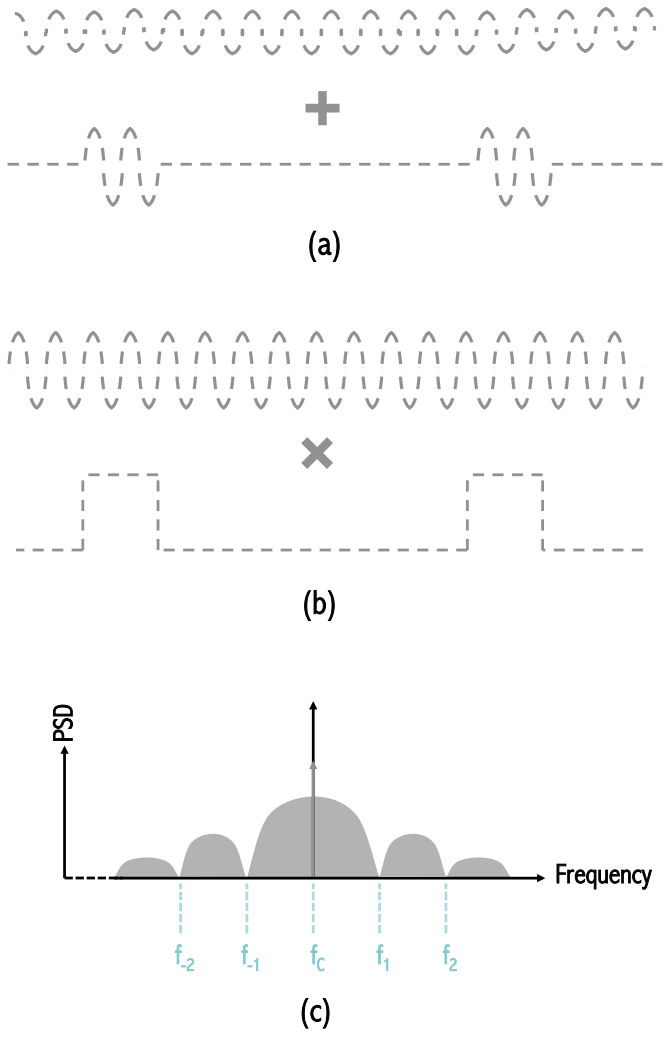

Figure 2.6: Spectrum of Reflective Wave

From above description of reflective impulse radios (RIR), it can be readily seen that the proposed architecture highly resembles that of an RFID radio. The passive transmission feature is fully preserved. Circuit power of a RIR transmitter can therefore be very low. The spectral content of the proposed architecture, on the other hand, resembles that of a UWB radio. In other words, an RIR radio combines the benefits of low power consumption (of RFID) and

high data rate (of UWB), substantially reducing the energy per bit consumed for data transmission.

Finally, on modulation schemes, the proposed architecture is amenable to various pulse-based signaling. Among those applicable however, Pulse Position Modulation (PPM) demonstrates several attractive features. First, a single pulse in PPM represents multiple bits of information, reducing the activity factor and the dynamic power of the circuit. Second, PPM encoding and pulse generation are amenable to simple digital implementation. Finally, the orthogonal signaling of PPM requires less energy per bit than its non-orthogonal counterparts (for example, Pulse Amplitude Modulation) [27], further improving the power efficiency. A quantitative analysis of these attributes of PPM will be offered in Chapter 3.

2.2.2 Circuit Diagram

The basic block diagram of a reflective impulse transmitter is shown in Figure 2.7. From right to left, it consists of an antenna and a metal-oxide-semiconductor (MOS) switch. Size of the antenna switch is typically large, requiring a buffer driver to its left. Signal to the driver is determined by the base-band data via the PPM encoder. Besides base-band data, inputs to the encoder also include a sequence of short pulses generated by the pulse generator, the last block in Figure 2.7. Finally the pulse generator may also contain a timer, which can be further synchronized to the system clock to its left.

What is shown in above Figure 2.7 are the basic elements of a reflective impulse transmitter. Additional features and variations can be added to enhance its sophistication. When the size allows for example, multiple antenna switches can be placed across the geometry of the antenna to make a more effective short circuit when the switches are turned on. Additionally, instead of shorting across the antenna, the switch can have a resistor and/or a capacitor in series when it provides a deeper modulation depth, defined as the difference in reflection between the on and off states of the antenna switch. The topic of resistive versus capacitive modulation will be discussed in Chapter 3. Finally other circuit functions such as start-up and power gating can be desirable, depending on the specific requirements as well as the design of rest of the system.

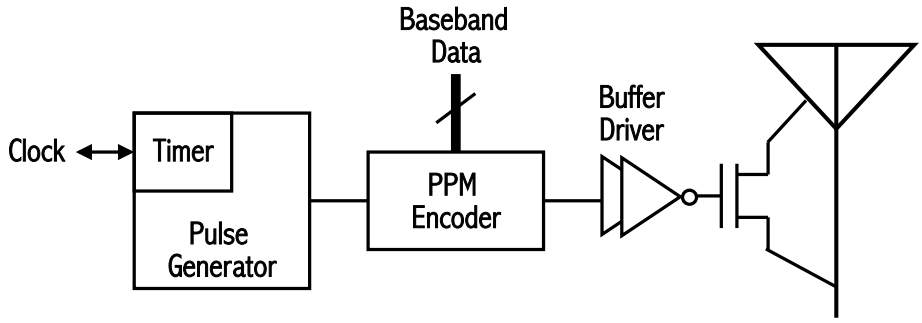

Figure 2.7: Block Diagram of a Reflective Impulse Transmitter

Details of implementation issues are again the subject of next chapter.

2.3 Direct Antenna Modulation

Given that the RIR radio is a hybrid of RFID and UWB, following question arises naturally for the antenna in Figure 2.7 — should its bandwidth be as narrow as RFID or as wide as UWB? At the first glance, one may suppose that it needs to be wide-banded, since the reflected wave has a quite broad spectral spread after all ...

Interestingly, it has been proven that when an antenna is directly switched on and off like in a reflective impulse radio, its effective bandwidth can be substantially extended from its inherent bandwidth [28, 29, 30]. In other words, the antenna does not necessarily need to be wide-banded. This is particularly good news for wireless sensor applications, where the size of broad-band antennas is not always affordable. Such bandwidth extension technique is referred in literature as *Direct Antenna Modulation*, or DAM.

Figure 2.8 describes an experiment carried out by Yao and Wang in 2004 [30]. There were two cases in comparison. In the first case, a *conventional* transmitter was used where the digital base-band signal was mixed with a radio frequency (RF) carrier, then fed to the antenna (Figure 2.8a). Inherent band-

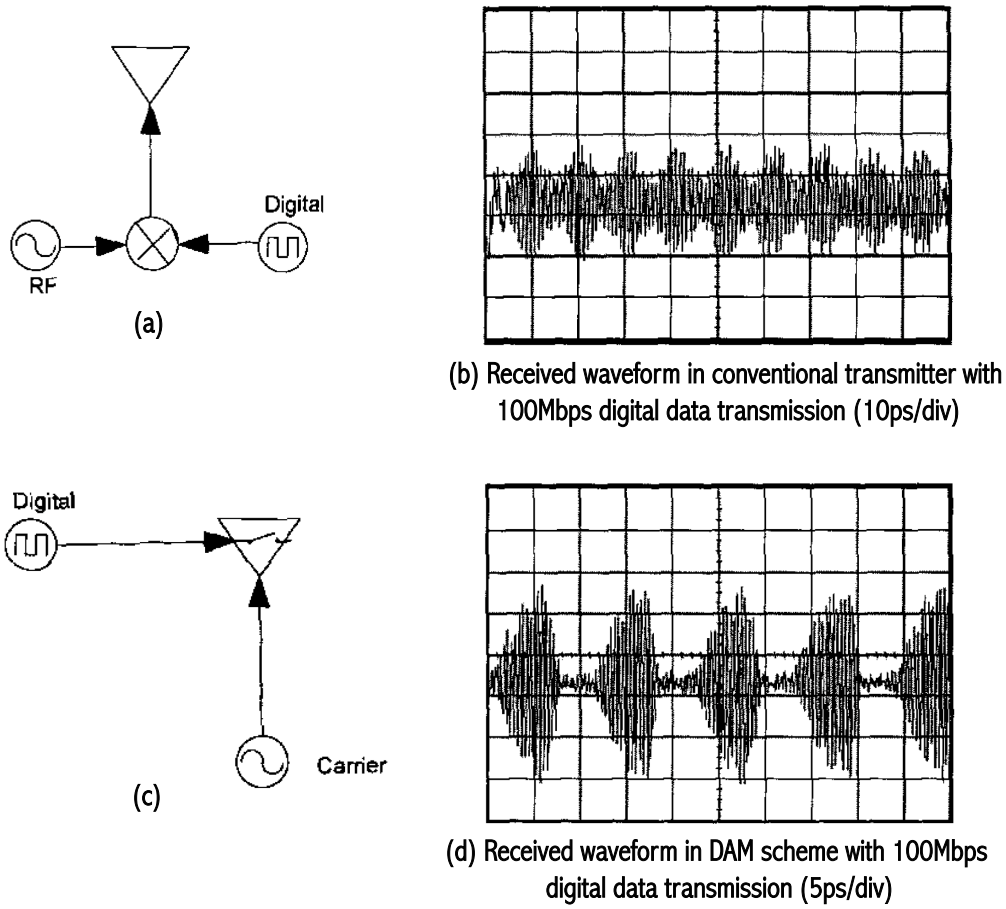

Figure 2.8: Direct Antenna Modulation Experiment [30]

width of the antenna was 30MHz. Therefore, when the base-band data rate reached 100Mbps, the received waveform displayed severe dispersion (Figure 2.8b). In the second case, the antenna, carrier and base-band signals were all identical to those in the first case. The mixer however was replaced by a switch across the antenna (Figure 2.8c). While the RF carrier was fed directly to the antenna, the base band signal was used to turn on and off the antenna switch. As a result, the received waveform showed far less dispersion (Figure 2.8d, please note different time scale between (b) and (d)). The 30MHz-bandwidth antenna was capable of transmitting 100Mbps signals in the

second case. Its effective bandwidth was reportedly extended by more than 10 times (400MHz/30MHz).

Reasons for above bandwidth extension can be conveniently explained from the equivalent circuit perspective. Suppose that an antenna is modeled by a resonant circuit with certain parallel resistance R_0. Bandwidth of the resonant circuit, hence that of the antenna, is inversely proportional to R_0:

$$B \propto \frac{Z_0}{R_0} \tag{2.6}$$

where B is the bandwidth and Z_0 is the characteristic impedance of the resonant circuit. In the conventional case, R_0 is what is inherent to the antenna. In the Direct Antenna Modulation case however, the antenna switch typically has an on-resistance substantially lower than R_0, boosting the bandwidth during the time when the switch is on. The bandwidth at switch off time should remain narrow, as long as the switch's off-resistance is much larger than R_0. This difference in bandwidth at on and off states can be readily observed in Figure 2.8. While the rise time of waveforms in (b) and (d) was comparable (note that the antenna switch was turned off during rise time), the falling in (d) was far sharper than (b). Authors of the original experiment believed this caused by asymmetric turn-on and -off characteristics of Schottky diodes [30]. Similar postulation was held in [28, 29]. While characteristics of switching devices can certainly impact that of the antenna, it is our belief that above asymmetry is fundamentally caused by circuit topology.

To verify above analysis, the experiment in Figure 2.8 can be repeated with CMOS switches instead of Schottky diodes. CMOS switches have relatively symmetric turn-on and -off characteristics and can thus minimize their impact on the rise and fall time of the waveforms. Furthermore it would have been desirable to repeat the experiment for the case of passive transmission. While this is not explicitly carried out either, the total system test in Chapter 4 will verify that such bandwidth extension effect does exist for passive transmitters too. Finally the receiver antenna still needs to be broadband to accommodate the wide bandwidth of the reflected signal. But as stated at the beginning of this chapter, the receiver can afford larger space than the transmitter, helping relieve a big part of the design challenge.

2.4 Range of Applicability

A hybrid of RFID and UWB, the reflective impulse radio seems to combine the best of both worlds. Is it really better than RFID and UWB under all conditions? The answer is No. At very low data rate (e.g. kbps), it turns out that RFID still holds an edge. At very high data rate (e.g. Gbps), reflective impulse radio's advantage over UWB also diminishes. Between these two extremes however, there still exists a broad range of applications where the new architecture is truly advantageous and more applicable than both RFID and UWB. This section will explore such range of applicability.

2.4.1 Power Consumption

One criterion for comparing different radios is the power consumption of their transmitters. Before making any comparison however, let us first evaluate the power consumption of the reflective impulse transmitter.

From Figure 2.7, there are clearly three components to the transmitter's total power consumption P_{tx}: pulse generator (P_{pg}), PPM encoder (P_{enc}), and buffer driver (P_{buf})

$$P_{tx} = P_{pg} + P_{enc} + P_{buf} \tag{2.7}$$

To find each term's relation to the data rate, let us define two more parameters T_{pr}, pulse repetition time, and M, number of pulse positions per T_{pr}. This is illustrated in Figure 2.9. Within every period of T_{pr}, there are M possible positions that a pulse can take ($M = 8$ in this example).

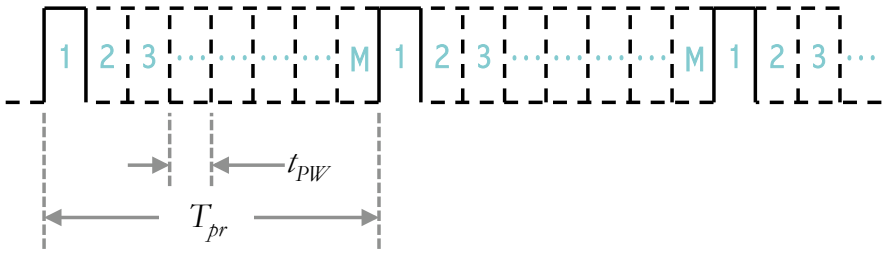

Figure 2.9: Definition of Pulse Repetition Time and Number of Pulse Positions

Given that one and only one pulse gets transmitted every T_{pr}, each pulse obviously represents $\log_2 M$ bits of base-band data. The (raw) data rate R is simply the ratio of the two

$$R = \frac{\log_2 M}{T_{pr}} \tag{2.8}$$

Finally, time width t_{PW} of each pulse is

$$t_{PW} = \frac{T_{pr}}{M} \tag{2.9}$$

With above parameters defined, we can now evaluate the power consumption of each of the components in Equation (2.7). The purpose of this exercise is **not** to compute any numeric results, which obviously depend on implementation specifics such as gate capacitances and switch resistance, etc. Rather, we are interested in deriving each power component's qualitative dependance on a few key parameters such as R and M above. These dependencies will not only help with our design optimization but also illustrate the comparative advantage of reflective impulse radios relative to RFID and UWB.

$\mathbf{P_{pg}}$: Power of Pulse Generator

There are multiple ways of implementing a pulse generator (for example a closed-loop oscillators or an open-loop delay line). Similarly its output can take either of the forms in Figure 2.10.

It is important to realize that although outputs in (a) and (b) look differently in Figure 2.10, they actually consume similar amount of dynamic power. There is only one output in (a), charged and discharged M times within the cycle time of T_{pr}. There are M outputs in (b) but each is charged and discharged only once per T_{pr}. So the dynamic circuit power of both (a) and (b) is

$$P_{pg} = \frac{M \times C_u \times V_{DD}^2}{T_{pr}} \tag{2.10}$$

where C_u is the capacitance associated with each output and V_{DD} is the supply

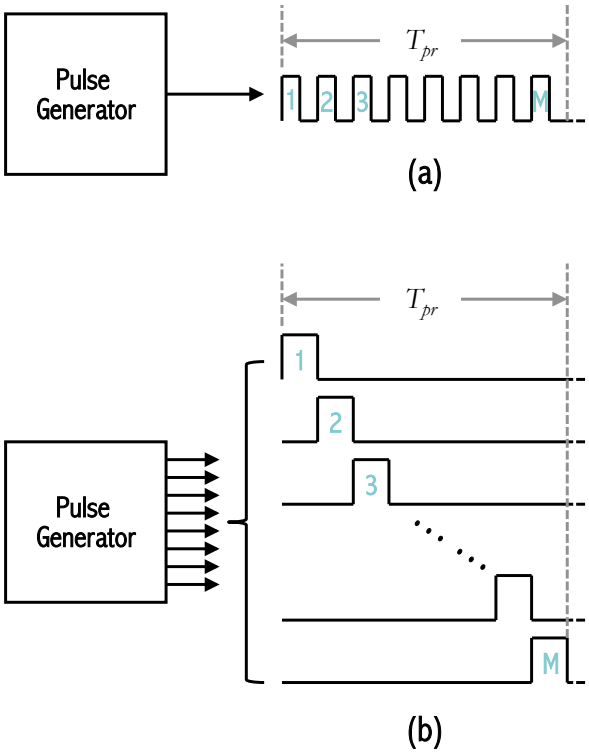

Figure 2.10: Forms of Pulse Generator Output

voltage. Replace T_{pr} with Equation (2.8)

$$P_{pg} = \frac{M \times R \times C_u \times V_{DD}^2}{\log_2 M} \tag{2.11}$$

Several simplifications were made in above derivation. First, same node capacitance was assumed for cases (a) and (b). Besides the reason that C_u is indeed comparable in both implementations, more importantly the purpose of this derivation is not to compare the two implementations but to expose P_{pg}'s dependance on R and M, which turns out to be identical between the two cases, as demonstrated in Equation (2.11). The second simplification was that only dynamic circuit power was included in Equations (2.10) and (2.11). When properly designed, the overall power consumption of a pulse generator

should be dominated by the dynamic power. Static power, including leakage and bias, should be minor by comparison. Finally the V_{DD} above refers to the main supply of the transmitter as opposed to the oscillator or delay line sub-block, because level shifter and logic driver can often consume more power than the oscillator or delay line itself.

To summarize, Equation (2.11) shows that the power consumption of a pulse generator scales linearly with the radio's data rate, and inversely logarithmically with the number of PPM pulse positions.

$\mathbf{P_{enc}}$: Power of PPM Encoder

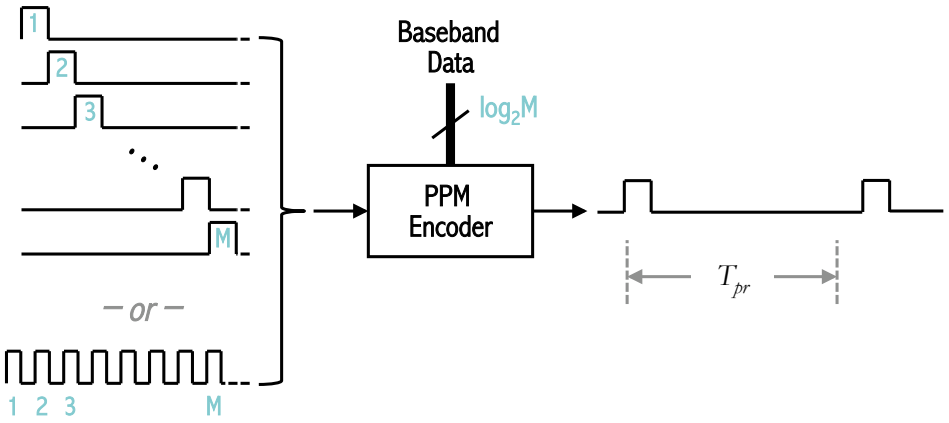

Figure 2.11: Function of a PPM Encoder

Purpose of the PPM encoder is to select an output pulse based on the $\log_2 M$ bits of base-band data (Figure 2.11). Its input can be either an array of M different pulses or a continuous clock. A simple and energy efficient way to implement the encoder is using switches. While the design details will be discussed in Chapter 3 (Figure 3.17), it is not difficult to conceive that the encoder will include M parallel paths, each consisting of $\log_2 M$ pass transistors (when pre-encoders are used, the number of series transistors can be a fraction

of $\log_2 M$). So the total number of pass transistors is

$$N = M \times \log_2 M \tag{2.12}$$

Assume further that gate capacitance of each pass transistor is C_t and that baseband data are completely random therefore have on average 50% possibility for each gate to switch within each cycle of T_{pr}. Total power consumption of the PPM encoder is then

$$P_{enc} = \frac{50\% \times N \times C_t \times V_{DD}^2}{T_{pr}} = \frac{M \times R \times C_t \times V_{DD}^2}{2} \tag{2.13}$$

Again Equation (2.8) was used in above derivation.

While it was a topic for discussion in the pulse generator section, the issue of dynamic versus static power is less controversial in a PPM encoder. By the virtue of switch-based logic, there is no leakage (neglecting gate leakage) or other forms of static power dissipation in the encoder.

Again to summarize, Equation (2.13) shows that the power consumption of a PPM encoder is proportional to both the data rate and the number of PPM pulse positions.

$\mathbf{P_{buf}}$: Power of Buffer Driver

Power of the buffer driver is easier to estimate, in the light of following recognition — when the circuit is properly designed, its dynamic power should far exceed the static power.

Assume that total gate capacitance of the buffer driver, including that of the antenna switch, is C_x. Within each period of T_{pr}, there is one pulse driven to the gate. Total power consumption is thus

$$P_{buf} = \frac{C_x \times V_{DD}^2}{T_{pr}} = \frac{R \times C_x \times V_{DD}^2}{\log_2 M} \tag{2.14}$$

Like the pulse generator, power of the buffer driver is proportional to the data rate, but inversely proportional to the logarithm of the number of pulse positions.

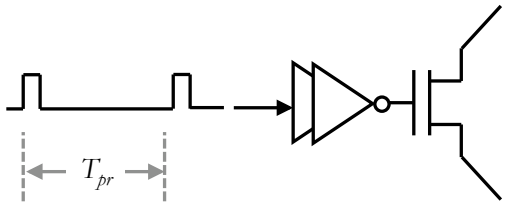

Figure 2.12: Buffer Driver

Total circuit power of the reflective impulse transmitter is the sum of all three power components above

$$P_{tx} = \frac{M \times R \times C_u \times V_{DD}^2}{\log_2 M} + \frac{M \times R \times C_t \times V_{DD}^2}{2} + \frac{R \times C_x \times V_{DD}^2}{\log_2 M} \quad (2.15)$$

2.4.2 Hidden Power

While above calculation may seem complete, does it include all the power that a reflective impulse transmitter consumes? Maybe not, especially when one compares it with an active transmitter.

A reflective transmitter requires that the receiver (the "reader") continuously radiates a radio wave. This is obviously not needed by an active transmitter. So to make a fair comparison, we need to capture this "hidden" power of the reflective impulse transmitter and include it in the overall power calculation. How to account for the hidden power actually depends on the way the transmitter (and rest of the wireless device) is powered. There can be multiple scenarios as summarized in Table 2.2 and Figure 2.13.

Results in Table 2.2 are now explained.

In the first scenario, the wireless device is powered by a battery, or an energy scavenger, or some other non-RF sources. The incoming radio wave required by a reflective transmitter in this case does not decrease the amount of power available to the device. In other words, there is no cost to have the receiver transmit a continuous wave. Therefore the "hidden" power is free, or 0. In scenario 2A, the device is equipped with an RF-to-DC regulator and is

Scenario	Powering Method	Cost of Hidden Power
1	non-RF sources	0
2A	RF source at different frequency than communication where power at individual band is limited	0
2B	RF source at different frequency than communication where total power limited	$\Delta P_{RF} \times \eta$
3	RF source at same frequency as communication	$P_{RF} \times \eta \times \delta$

Table 2.2: Device Powering Scenarios and Cost of Hidden Power

powered by a wireless source. For efficiency or other considerations however, the frequency for RF powering is different than the one for communication. It is conceivable for example, that power is delivered via inductive coupling at kHz frequencies while data on the other hand are transmitted at MHz or even GHz range to support any meaningful data rate. Because these frequencies belong to different spectral bands, from the spectrum regulation point of view, the amount of power at the communication band does not reduced the allowed power at the powering band. The hidden power is also 0 in this scenario. Next on the list, scenario 2B is almost identical to 2A, except that the amount of power at the communication band also affects the allowed power at the powering band. One of such examples is the biomedical implant application introduced in Chapter 1. To prevent RF waves from heating the human body, power over *all* frequency bands is subject to a congregated limit. In this case, the amount of power used for data communication reduces the amount of power available for RF power delivery, even at a different frequency. Assume that ΔP_{RF} is the reduction in RF power available for power delivery and η is the efficiency of the RF-DC regulator. Cost of the "hidden" power P_c is then

$$P_c = \Delta P_{RF} \times \eta \tag{2.16}$$

Please note that η is necessary in above equation because so far in all our calculations power is assumed at DC.

Finally in scenario 3, not only the device is powered by an RF source but it is also at the same frequency band as data communication. This is further illustrated in Figure 2.14. Suppose that total incoming power for both powering

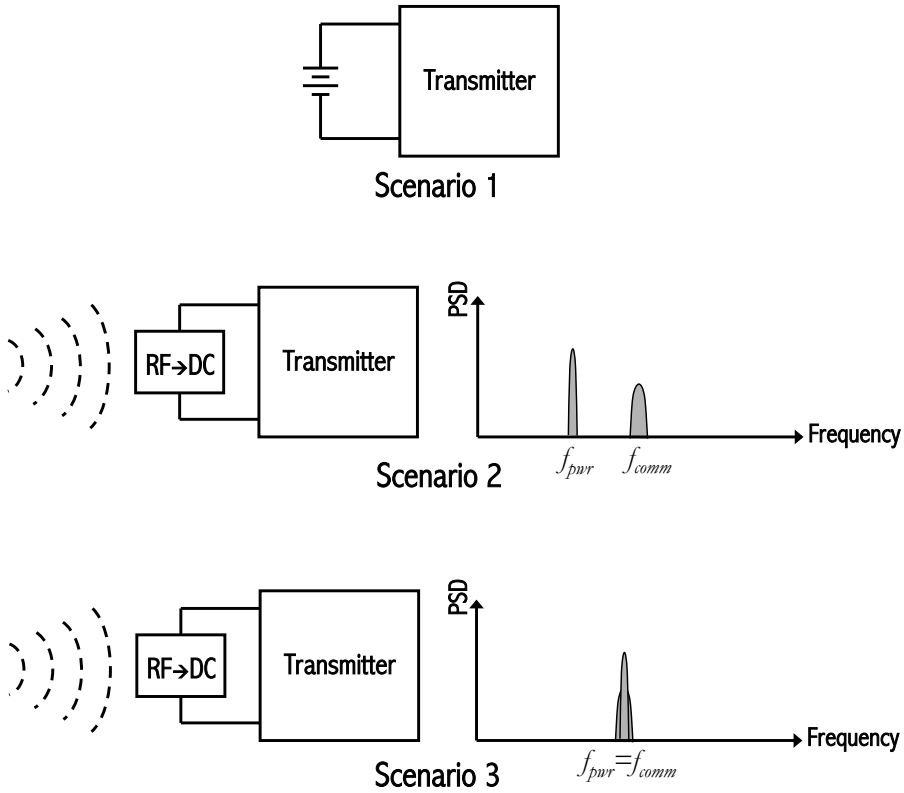

Figure 2.13: Device Powering Scenarios

and communication is P_{RF}. After the RF-DC regulator, which has an efficiency of η, the amount of power becomes P_{DC}, delivered to the transmitter (P_{tx}) and to rest of the system (P_{other}). When the transmitter transmits, it closes the switch across the antenna and reflects much of the incident wave back to the receiver. Lack of an input source, the RF-DC regulator can no longer collect power during those incidences. Assume that the transmitter turns on the antenna switch with a duty cycle δ. The "hidden power" is then

$$P_c = P_{RF} \times \eta \times \delta \tag{2.17}$$

Apparently

$$\delta = \frac{1}{M} \tag{2.18}$$

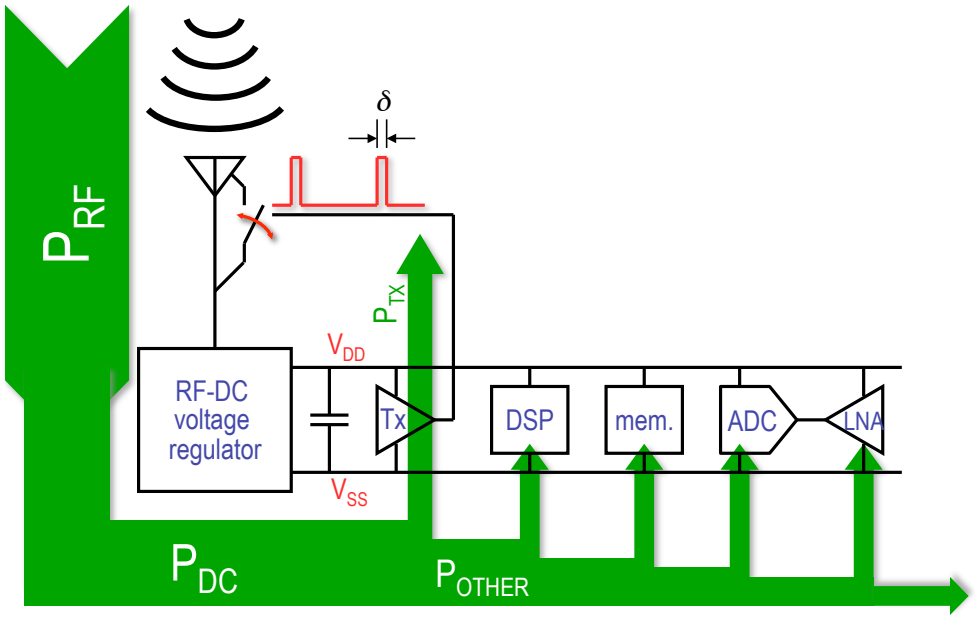

Figure 2.14: Power Flow of an RF-Powered Wireless Device

where M is the number of PPM pulse positions introduced previously. Subsequently

$$P_c = \frac{P_{RF} \times \eta}{M} \tag{2.19}$$

Besides what is listed in Table 2.2, there obviously exist other varieties of powering scenarios. Even at the same frequency, the power radiated from the receiver can for example be phased with different amplitude for powering and for communication. In fact, one of such phased strategies will be presented in Chapter 3. But no matter how sophisticated the strategy is, it can always be decomposed to a combination of the scenarios in Table 2.2, allowing its hidden power to be rather conveniently computed.

2.4.3 Total Equivalent Power

With both the apparent and hidden power identified in Equations (2.15) and (2.19), total power consumption of a reflective impulse transmitter can now be summarized

$$P_T = P_{tx} + P_c = R \cdot V_{DD}^2 \left(\frac{M \cdot C_u}{\log_2 M} + \frac{M \cdot C_t}{2} \right) + \left(\frac{R \cdot C_x \cdot V_{DD}^2}{\log_2 M} + \frac{P_{RF} \cdot \eta}{M} \right) \tag{2.20}$$

Obviously, items in the first bracket in Equation (2.20) increase with M, while those in the second bracket decrease with M. There therefore must exist an optimal value of M at which the power of the transmitter is minimum. It is also obvious that this optimal M depends on following groups of parameters:

(1) C_u, C_t and C_x, which are in turn determined by fabrication technologies and device characteristics;

(2) R, which is an application requirement;

(3) V_{DD} and η, which depend on system specifications and the design of the RF-DC regulator. Actually in our calculation, η also includes efficiency of the antenna and the antenna-regulator matching coefficient;

(4) P_{RF}, which is subject to regulations and link budget and will be discussed more in next chapter.

While all above parameters can vary substantially from applications and implementations, as an example Figure 2.15 plots transmitter power versus the number of pulse positions. Parameters used in this example are listed in Table 2.3. As can be seen, when M increases, the hidden part of the total power decreases, obvious from Equation (2.19). The trend with the circuit power, on the other hand, is not monotonic. While the third term in Equation (2.15) dominates for small values of M, the first two terms become substantial as M becomes larger. Combining the hidden and circuit power, the total transmitter power displays a minimum at around $M = 64$, when the amplitudes of these two constituents are about equal.

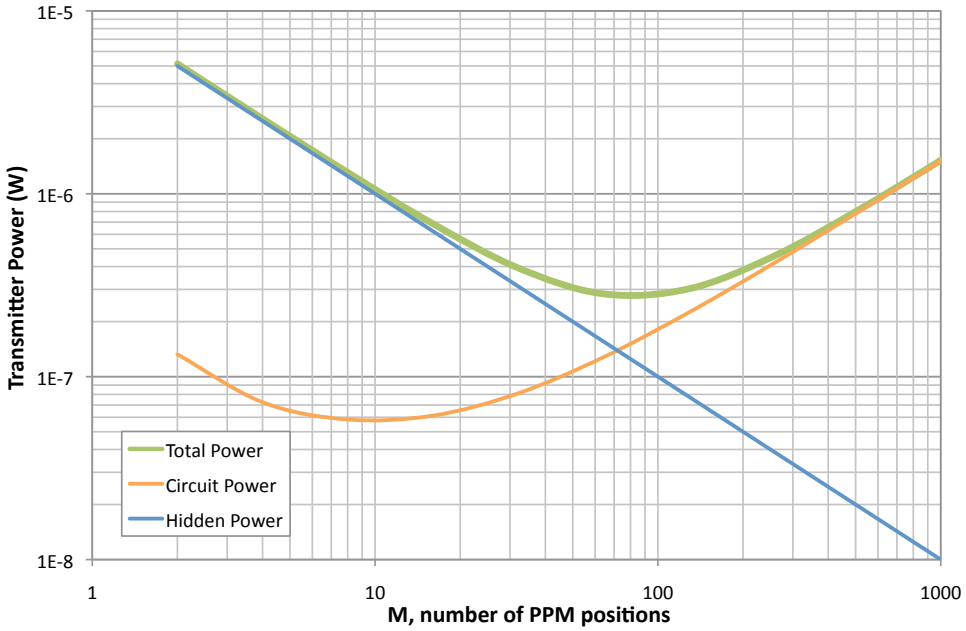

Figure 2.15: Transmitter Power versus Number of PPM Pulse Positions

C_u	C_t	C_x	R	V_{DD}	η	P_{RF}
$10fF$	$10fF$	$500fF$	1Mbps	0.5V	10%	$100\mu W$

Table 2.3: Example Parameters for Transmitter Power Optimization

2.4.4 Reflective Impulse Radio vs. RFID

As introduced at the beginning of the chapter, radio frequency identification (RFID) is a technology that allows a physical object to be identified without making physical contact. To ensure inter-operabability, there is a full set of regulations and standards specifying how this technology should be implemented. Spectral bandwidth for instance, is one of the parameters strictly regulated. Table 2.4 lists the regulatory status for operating ultrahigh frequency (UHF) RFID in selected countries and regions [32]. Most countries allow only 2MHz of bandwidth. China allows 4MHz; and the United States seems the most generous with 26MHz of allocation. However attention should be paid to the FHSS

(frequency hopping spread spectrum) required in both countries. For example, the maximum bandwidth of each hopping channel in the United States is only 500kHz [33].

Country/Region	**Frequency**	**Technique**
China	840.5-844.5 MHz	FHSS
	920.5-924.5 MHz	FHSS
Europe	865.6-867.6 MHz	
India	865-867 MHz	
Japan	952-954 MHz	LBT
USA	902-928 MHz	FHSS

Table 2.4: UHF RFID Regulatory Status in Selected Countries and Regions [32]

One may wonder: *why are all RFIDs narrow-band?* Answers to this question can actually lead to the fundamental difference between the reflective impulse radio and RFID.

The narrow-band limitation on RFID can be understood from two different angles: spectrum sharing and circuit implementation. First, for various wireless communications to coexist, each radio is allowed only a sliver of spectrum. It will otherwise cause interference to other radios. An interesting exception occurred in February 2002 when the Federal Communications Committee (FCC) in the United States allowed ultra wide-band communications only if the transmitted power is so low that it is under the noise floor of other narrow-band radios [34]. The principle of spectrum sharing has since been revised to: either high power within narrow bandwidth, or low power over broad bandwidth. **There is no room for the "middle ground" between the two**. RFID requires high power (for powering the tag) and can therefore operate only within narrow band. The second reason for RFID's narrow band is for circuit implementation. Conventional wisdom is to operate the tag at low clock frequency — whether the clock is generated by the tag itself or derived from amplitude modulation of the carrier — to conserve circuit power. Bandwidth

of the backscattered signal is therefore rather narrow. Appearing reasonable in their own ways, these two justifications for narrow band collaborate and reinforce each other.

The reflective impulse radio challenges above justifications. It argues that higher clock frequency does not necessarily translate to higher circuit power — the proportionality between power and frequency no longer holds when the clock operates with duty cycles. This is indeed how UWB achieves high energy efficiency. Additionally, the reflective impulse radio combines both scenarios of spectrum sharing. While the high power carrier occupies very narrow bandwidth, the reflected signal is ultra wide-band with much lower power. As each component causes no interference to other wireless systems, the combination of the two should not either. One can thus design the spectral profile of the new radio to meet existing regulations such as the FCC.

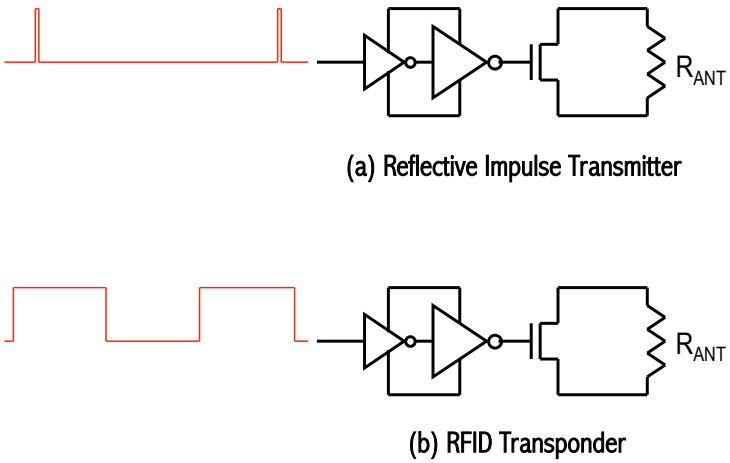

Figure 2.16: Reflective Impulse Radio versus RFID

Let us now construct a case for comparison between RFID and the reflective impulse radio. Due to its narrow bandwidth, the RFID is usually limited to modulation schemes such as ASK (amplitude shift keying), FSK (frequency shift keying), and PSK (phase shift keying) [18]. To the contrary, a reflective impulse radio supports pulse-based modulations like PPM, extending its signal

bandwidth far beyond what is specified in Table 2.4. This is illustrated in Figure 2.16. Drawn identically, both transmitters have similar buffer drivers and antenna switches. Even the antennas, depending on the data rate, can be the same — thanks to the benefit of bandwidth extension by Direct Antenna Modulation. What is different however are the signals fed from the left. Input to the reflective impulse transmitter's buffer driver is a sequence of narrow pulses; that to the RFID transponder is a rectangular wave with comparable on- and off-time. This difference in signal modulation has obvious consequences not only in the radios' maximum achievable data rate, but also in their power consumption.

To quantify the comparison in Figure 2.16, let us make following two assumptions:

(1) the RFID transponder uses on-off keying (OOK), a special type of ASK modulation, as it is not only among of the simplest to implement and one of the most popular modulation schemes used in RFID but also its power efficiency is among the highest in RFID. Results with other possible module schemes will be briefly addressed at the end of this section too;

(2) to minimize its power consumption, the RFID transponder operates with following duty cycle schedule: when it is active, the transponder transmits at the maximum data rate that its bandwidth allows; it is then deactivated after all data are sent. Note that this is different type of duty cycling from what is described in UWB. In UWB, the transmitter shuts off after each pulse; here the transmitter shuts off after a group of data. Duty cycling occurs at the symbol level and the packet level, respectively.

With above two assumptions, the RFID transponder under analysis should represent one of the simplest and most energy efficient RFID transmitters.

Before performing power analysis however, let us first derive the duty cycle described in the second assumption above. Suppose that the maximum bandwidth of the RFID is B_{Max}. Its transponder's minimum on- and off-time (similar to t_{PW} in the reflective impulse radio) is then

$$t_{Min} = \frac{2}{B_{Max}} \tag{2.21}$$

Because each on and off pulse represents one bit in OOK, the maximum data rate of RFID is

$$R_{Max} = \frac{1}{t_{Min}} = \frac{B_{Max}}{2} \tag{2.22}$$

Duty cycle D_T of the transponder is thus

$$D_T = \frac{R}{R_{Max}} = \frac{2R}{B_{Max}} \tag{2.23}$$

where R is the actual averaged data rate.

Like the reflective impulse radio, there are also four components in an RFID transponder's power consumption.

The first component is the timer, equivalent to P_{pg} in Equation (2.11). Under the previous assumption that the RFID transponder operates at maximum bandwidth, this part of the power consumption is

$$P'_{pg} = C_u \times V_{DD}^2 \times \frac{1}{t_{Min}} = C_u \times V_{DD}^2 \times \frac{B_{Max}}{2} \tag{2.24}$$

The second part is the encoder. For OOK, it is a simple *nand* gate, operating under duty cycle D_T

$$P'_{dec} = 50\% \times C_t \times V_{DD}^2 \times \frac{1}{2t_{Min}} \times D_T = \frac{C_t \times V_{DD}^2 \times R}{4} \tag{2.25}$$

The 50% factor above comes again from the assumption that base-band data are completely random thus have on average 50% possibility of making a logic transition. The third power component is the buffer driver, also operating under duty cycle D_T

$$P'_{buf} = 50\% \times C_x \times V_{DD}^2 \times \frac{1}{2t_{Min}} \times D_T = \frac{C_x \times V_{DD}^2 \times R}{4} \tag{2.26}$$

Finally the "hidden" power is

$$P'_c = 50\% \times D_T \times P_{RF} \times \eta = \frac{R \times P_{RF} \times \eta}{B_{Max}} \tag{2.27}$$

Table 2.5 lists all four equations above, next to those from the reflective impulse radio. It is not obvious at the first glance which radio is more power efficient. The encoder power of RFID for example, is guaranteed lower than that of the reflective impulse transmitter. Indeed, the overall power consumption of an RFID transponder can be lower, albeit only at rather low data rate. This will become more evident after the analysis below.

	Reflective Impulse Tx	**RFID Transponder**
Timer	$C_u \times V_{DD}^2 \times \frac{R \times M}{\log_2 M}$	$C_u \times V_{DD}^2 \times \frac{B_{Max}}{2}$
Encoder	$C_t \times V_{DD}^2 \times R \times \frac{M}{2}$	$C_t \times V_{DD}^2 \times R \times \frac{1}{4}$
Buffer Driver	$C_x \times V_{DD}^2 \times R \times \frac{1}{\log_2 M}$	$C_x \times V_{DD}^2 \times R \times \frac{1}{4}$
Hidden Power	$P_{RF} \times \eta \times \frac{1}{M}$	$P_{RF} \times \eta \times \frac{R}{B_{Max}}$

Table 2.5: Power Components of Reflective Impulse Transmitter and RFID Transponder

Let us again use the parameters in Table 2.3 for power comparison between the reflective impulse radio and RFID. The additional parameter, B_{Max}, is set to 2MHz (from Table 2.4). Figure 2.17 plots the total power consumption of an RFID transponder (red) and a reflective impulse transmitter (green, where the number of PPM pulse positions is optimized for each data rate). At less than 2kbps, power of the reflective impulse radio is dominated by its "hidden" power and is as much as 75% higher than that of the RFID. As the data rate increases however, RFID's power starts to overpass and the difference between the two radios grows. Then at 1Mbps and beyond, the OOK-modulated RFID system fails to support the data rate, while the new radio continues to scale up towards 20Mbps.

Let us now discuss the maximum data rate of RFID and the reflective impulse radio, respectively. The 1Mbps for RFID in Figure 2.17 is clearly limited by its maximum bandwidth (2MHz) and its simple modulation scheme (OOK).

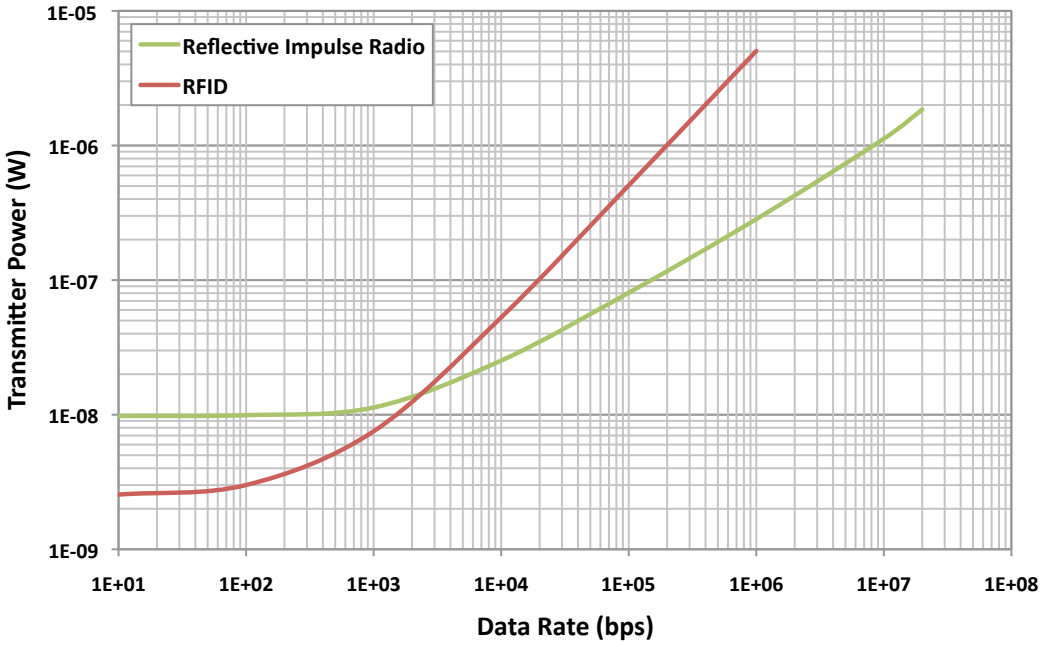

Figure 2.17: Power Comparison between Reflective Impulse Radio and RFID

The 20Mbps of the reflective impulse radio, on the other hand, is primarily limited by the signal to noise ratio (SNR) required to reliably decode the narrow pulses at the receiver side. While quantitative analysis of link budget and SNR is the first topic of next chapter, qualitatively speaking the lower the data rate is, the larger the pulse width is, hence the more energy per pulse there is to decode it. For the actual bio-implant example, calculations in Chapter 3 will show that given all practical parameters for path loss, noise figure, modulation depth, maximum radiation power from the reader, etc., the SNR is about 24dB at 1Mbps. At 20Mbps, the SNR is about 10dB, corresponding to a bit error rate (BER) of 10^{-4}. Graphical relation between SNR and BER is plotted in Figure 3.4 (of next chapter). For other practical examples, the maximum data rate of the reflective impulse radio can of course be much higher or lower than 20Mbps.

Above comparison is based on the sole criterion that the data rates of re-

flective impulse radio and RFID are identical. All other parameters are allowed to vary. As a result the RFID transmits more energy per bit. Can its energy efficiency be improved, by for instance changing from OOK to ASK with lower modulation depth and at the same time allowing the RF-to-DC regulator to continue harvesting energy while data are simultaneously transmitted? The answer is probably. Such improvements can indeed move the crossover point in Figure 2.17 towards a higher data rate, albeit not fundamentally change the conclusion that the reflective impulse radio is more efficient at higher data rate. Moreover, RF-to-DC regulators typically operate with a lower conversion efficiency when the RF input amplitude is low [13]. Finally, unlike the PPM of the reflective impulse radio, ASK is a non-orthogonal modulation scheme that requires higher transmitted energy per bit for same bit error rate (BER) [20]. Therefore further improvement to the RFID transponder's energy efficiency is probable but limited.

2.4.5 Reflective Impulse Radio vs. UWB

Unlike its reflective counterpart, an UWB impulse radio employs an active transmitter that sends out the pulsating waves all by itself. There is no need for receiver-generated carriers, at least not for communication purposes. Instead the carrier is generated by the transmitter too, shown as narrow pulses in Figure 2.18b. Consequently, there exists another difference between the two radios in that an UWB transmitter employs a power amplifier (PA) in place of the antenna switch. V_{DDx} is the extra supply voltage for the PA, which typically consumes significant amount of energy. It is worth noting that there are many flavors of UWB impulse transmitters (from the "spark-gap" in 1917 to its many modern-day variants). The one in Figure 2.18b is possibly the simplest and the most energy efficient. In other words, the case in Figure 2.18 is set up such that the reflective impulse radio is comparing against the most efficient kind of UWB radios. Let us now compare the power consumption of these two transmitters, on the basis of **same data rate** and **equal transmitted energy per bit**. If the reflective transmitter wins the competition from the UWB transmitter in Figure 2.18b, it should win all other UWB transmitters by even larger margins.

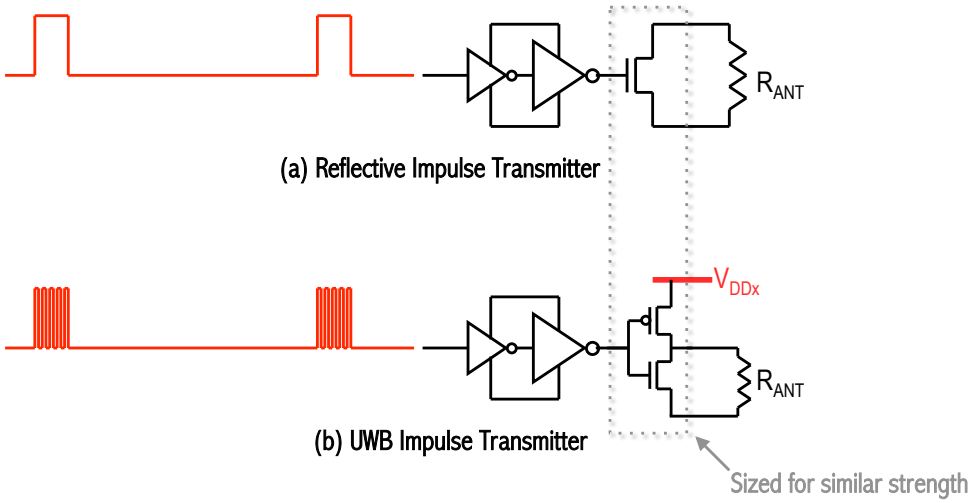

Figure 2.18: Reflective Impulse Radio versus UWB

On the basis of same data rate, envelope of the waveform in Figure 2.18 (b) matches the pulse wave in (a). Beneath the envelope is the high frequency carrier. Clearly the UWB transmitter incurs more power both in its pulse generator and in its buffer driver (assuming that the inverter PA in (b) is sized for comparable strength as the antenna switch in (a), requiring similar buffer drivers). Consumption by the PPM encoder on the other hand should be same. To quantify the differences in pulse generator and buffer driver, assume that f_C is the carrier frequency and t_{PW} is the pulse width. The new pulse generator power is

$$P''_{pg} = C_u \times V_{DD}^2 \times f_C = P_{pg} \times f_C \times t_{PW} \tag{2.28}$$

where P_{pg} is the pulse generator power of the reflective impulse radio in Equation (2.11). Similarly the new buffer driver power is

$$P''_{buf} = P_{buf} \times f_C \times t_{PW} \tag{2.29}$$

where P_{buf} is the buffer driver power of the reflective impulse radio in Equation (2.14). Apparently

$$f_C \times t_{PW} > 1 \tag{2.30}$$

therefore

$$P''_{pg} > P_{pg} \tag{2.31}$$

$$P''_{buf} > P_{buf} \tag{2.32}$$

In words, an UWB transmitter consumes more power in two of its three circuit components. Power in the third component is comparable. Total circuit power of an UWB transmitter is therefore still higher than that of a reflective impulse transmitter.

A reflective impulse transmitter, as previously mentioned, has certain "hidden power" not present in an active transmitter. The UWB transmitter on the other hand has an additional component, namely the PA. So the last step in our comparison is to compute this additional power of the UWB transmitter then compare it to P_c in Equation (2.19). This can be done by quantifying the earlier assumption that both transmitters need to transmit equal amount of energy per bit. Given same PPM modulation, equal energy per bit also means equal energy per pulse.

Assume that same antenna is used in both Figure 2.18 (a) and (b) and that its equivalent resistance is R_{ANT}. Further assume that resistance of the antenna switch in (a) and that of the PA in (b) are both much lower than R_{ANT} (to maximize modulation depth and power efficiency respectively). "Transmitted" energy per pulse by the reflective impulse transmitter is

$$E_{p,a} = \frac{1}{2} \times P_{RF} \times t_{PW} \tag{2.33}$$

The $\frac{1}{2}$ factor above comes from the fact that even under perfect power matching conditions, 50% of incoming RF power is reflected back. Supplied by V_{DDx}, the inverter PA in the UWB transmitter transmits following amount of energy per pulse

$$E_{p,b} = \frac{V_{DDx}^2}{2 \times R_{ANT}} \times t_{PW} \tag{2.34}$$

The $\frac{1}{2}$ factor in Equation (2.34) comes from the fact that V_{DDx} is the peak, instead of RMS (root square mean), of the RF wave. Equating $E_{p,a}$ to $E_{p,b}$,

$$V_{DDx} = \sqrt{P_{RF} \times R_{ANT}} \tag{2.35}$$

The extra power consumed by V_{DDx} is thus

$$P''_c = \frac{V_{DDx}^2}{R_{ANT}} \times \delta = \frac{V_{DDx}^2}{R_{ANT} \times M} = \frac{P_{RF}}{M} \tag{2.36}$$

where δ is the pulse duty cycle defined in Equation (2.18).

Comparing Equation (2.36) to (2.19),

$$P_c'' = \frac{P_c}{\eta} \tag{2.37}$$

As previously discussed, η includes not only the efficiency of the RF-DC regulator, but also the efficiency of the antenna (which is at best 50%) and the antenna-regulator matching coefficient. Therefore

$$\eta \ll 50\% \tag{2.38}$$

$$P_c'' \gg P_c \times 2 \tag{2.39}$$

Apparently the extra power of an UWB transmitter is more than twice the hidden power of the reflective impulse transmitter. Adding this to the results from circuit power, it can be concluded that all included, **a UWB transmitter is less energy efficient than a reflective impulse transmitter.**

To quantitatively illustrate above difference in power consumption, same example in Table 2.3 is used, with additional assumptions that the carrier frequency f_C is $500M$Hz and that the number of pulse positions M is 64 (optimum from Figure 2.15). The results are shown in Figure 2.19. Out of four components of the total power consumption, three of them (P_c, P_{buf} and P_{pg}) increase dramatically from the reflective impulse transmitter to the UWB transmitter. The fourth component (P_{enc}) is unchanged. Overall, the total power consumption differs by more than 10 times.

Above analysis concludes our comparison of power consumption. As a conclusion is only as good as its assumptions, there are of course other ways to make the comparison. One can for example assume that the two radios have totally different spectral profile and different number of PPM positions while maintaining same data rate and same transmitted energy per bit. The calculation will be more intricate, although not entirely intractable, and more assumptions need to be made about the circuit parameters. And in the end, the conclusion that a passive transmitter is more energy efficient than its active counterpart should still hold.

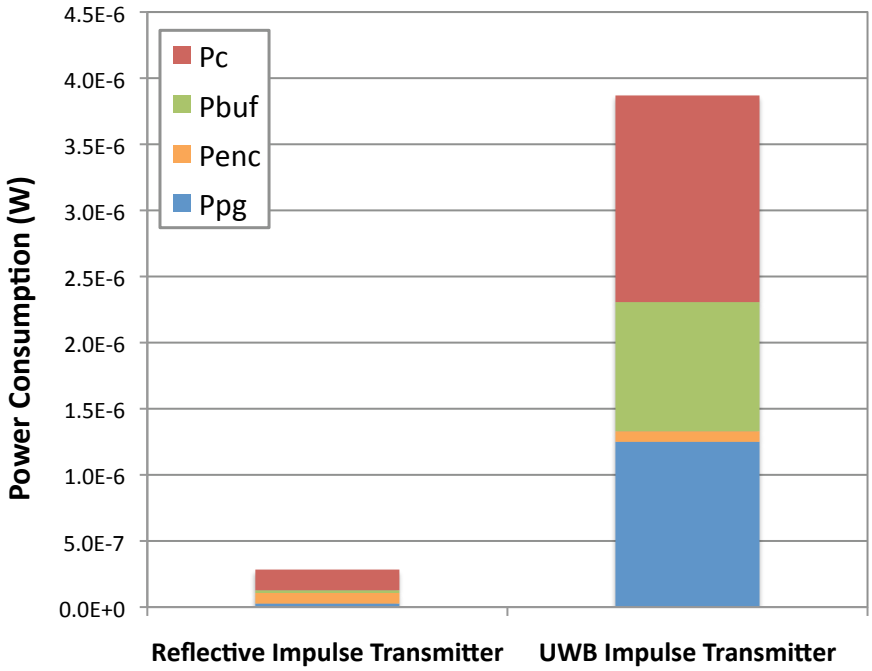

Figure 2.19: Power Comparison: Reflective Impulse Radio vs. UWB

Finally, although power is of our primary interest, there are obviously other differences between the reflective impulse radio and UWB. One of them is the antenna bandwidth, which is to the reflective radio's advantage as explained in the Direct Antenna Modulation section. Another difference is carrier accuracy. Generated by the high-power receiver, the carrier signal in the reflective impulse radio is much better controlled. In cases where multiple radios exist, this can be an important asset in combating interference. Regarding interference, the reflective radio does suffer from the additional jammer created by itself. Its receiver needs to discern the weak reflected signal in the midst of a loud echo of the carrier. Although the receiver can afford higher power and larger space than the transmitter, the existence of this self interference does complicate the receiver design quite substantially and some of the mitigation schemes will be discussed in Chapter 3. Finally there are applications where the RF radiation is severely limited and/or channel loss is prohibitively high. It is then necessary to employ an active radio architecture even if it demands much higher power

consumption.

2.4.6 Summary

Since the reflective impulse radio is a hybrid of UWB and RFID, let us now plot all three radios on the same chart and define a range of applicability where the new architecture holds some significant advantage. Same set of parameters is carried over from previous examples and repeated in Table 2.6. The competitive results are shown in Figure 2.20.

C_u	C_t	C_x	V_{DD}	η	P_{RF}	B_{Max}	f_C
$10f$F	$10f$F	$500f$F	0.5V	10%	100μW	2MHz	500MHz

Table 2.6: Example Parameters for Power Comparison

As discussed in the previous section, RFID (red) has the lowest transmitter power at very low data rate. This is largely due to the very low duty cycle that it gets to enjoy. After the data rate passes a few kbps, the reflective impulse radio (green) becomes the most energy efficient. It is however interesting to observe that as data rate increases, the difference between RFID and the reflective impulse radio increases, while that between UWB (blue) and the reflective impulse radio actually decreases. The increase in the first part is because the "hidden" power becomes a growing portion of the total consumption — with a larger pulse width, RFID certainly incurs more hidden power than its impulse counterpart. The decrease in the second part is due to the shrinking value of pulse width t_{PW}. To support increasing data rate, pulse width needs to shrink. So does the difference factor $f_C \times t_{PW}$ between the circuit power of UWB and the reflective impulse radio. But as the product $f_C \times t_{PW}$ is always larger than unity and η is always less than 100%, UWB always consumes more energy hence the blue curve in Figure 2.20 stays always atop of the green. Finally Figure 2.20 shows that UWB has a higher maximum data rate (100Mbps) than that of the reflective impulse radio (20Mbps) and of RFID (1Mbps). This data rate extension is due to the fact that the active transmitter of UWB suffers the path loss only once while its reflection-based counterparts suffer twice (from

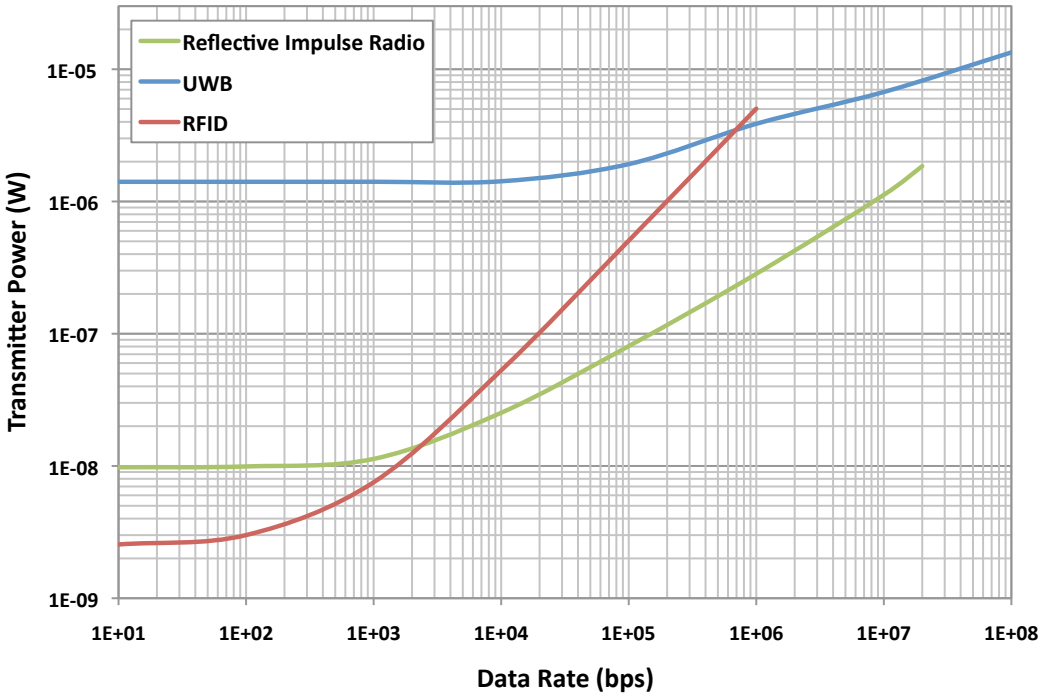

Figure 2.20: Transmitter Power Comparison among Reflective Impulse Radio, UWB and RFID

the reader to the passive transmitter then back to the reader). Therefore, in a radiation power limited environment like the bio-implant example, the active UWB radio can have larger SNR hence support higher data rate.

In summary the range where the proposed reflective impulse radio has over 50 % power advantage is **between 10kbps and 20Mbps**, covering over three decades of data rate and a broad space of wireless sensor network applications.

While the new radio's range of applicability appears broad in above analysis, be reminded that it is based on the specific example in Table 2.6. Same analysis can be performed on different sets of parameters, which will likely conclude on a different but, very possibly, similar range of applicability. Additionally, above analysis only takes power into account. Mentioned in Section 2.4.4, there exist

applications where the wireless link budget is insufficient to support any kind of passive transmission. One is then left with no choice but to employ an active transmitter architecture such as UWB.

Chapter 3

Design

With the analysis of reflective impulse radios (RIR) in Chapter 2, let us now practice the design of the new radio. Step by step, we will go over the entire implementation procedure in the following order:

– BER and link budget;
– Antenna switch;
– Pulse generator;
– PPM encoder;
– RIR receiver.

The implantable neural transmitter was introduced in previous chapters as an example of future wireless sensor networks. We will continue to use it in this chapter as a design example to illustrate the design procedure at every step. By the end of this chapter a complete neural transmitter will be presented, the test results of which will be later reported in Chapter 4.

3.1 BER and Link Budget

Every radio design begins with link budget assessment. Not only does it determine the appropriate transmit power and receiver sensitivity, but also decides — in the case of Reflective Impulse Radios — whether it is feasible

to deploy the new radio architecture for a specific application. Obviously the ultimate factors are the bit error rate (BER) and signal to noise ratio (SNR). So together with signal propagation and path loss, sources of noise and interference will be discussed in this section as well.

3.1.1 Path Loss

Assume that power of the carrier radiated by the receiver is P_{rx} (Figure 3.1). What is P_{sig}, power of the signal reflected back from the transmitter? There are actually four components in the overall path loss:

(1) *channel loss*, which accounts for the propagation loss between transmitter and receiver antennas;

(2) *transmitter antenna "gain"*, which is in reality a loss factor for electrically small antennas;

(3) *modulation depth*, which is defined in Chapter 2 as the difference in reflection between the on and off states of the antenna switch; and finally

(4) *front end loss of the receiver*, including receiver antenna loss, insertion loss of its matching network, and any impedance mismatch in the front end.

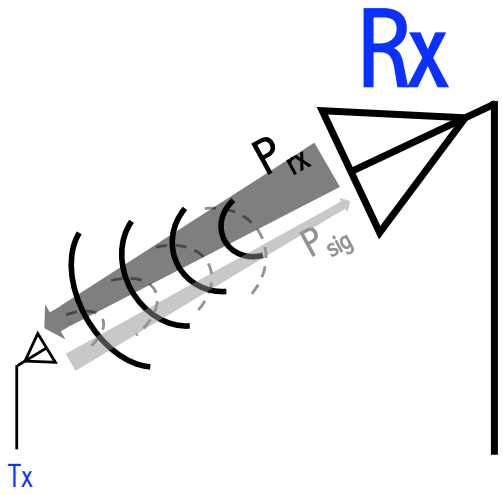

Figure 3.1: Carrier and Signal Power in Reflective Impulse Radio

Among all four components above, modulation depth is probably the least intuitive. It is a parameter that measures the effectiveness of reflection. For instance, when the carrier comes incident to the transmitter antenna, at least half of its power is reflected back towards the receiver (even if the antenna and circuit are perfectly power matched). When the switch turns on, more power is reflected. Therefore a meaningful measure of signal strength is **not** the amplitude of the reflected wave itself, but the amplitude **difference** between the two cases. Such difference is defined as "modulation depth" (Figure 3.2). Please note that this definition differs slightly from the "modulation index" (often referred as modulation depth too) in the conventional AM (amplitude modulation) context. In the reflective impulse radio case, modulation depth is limited below 50%; the modulation index in an AM radio can be as high as 100%. Additionally, the phase difference between the two states can also be utilized for signal detection and a similar modulation depth can be defined.

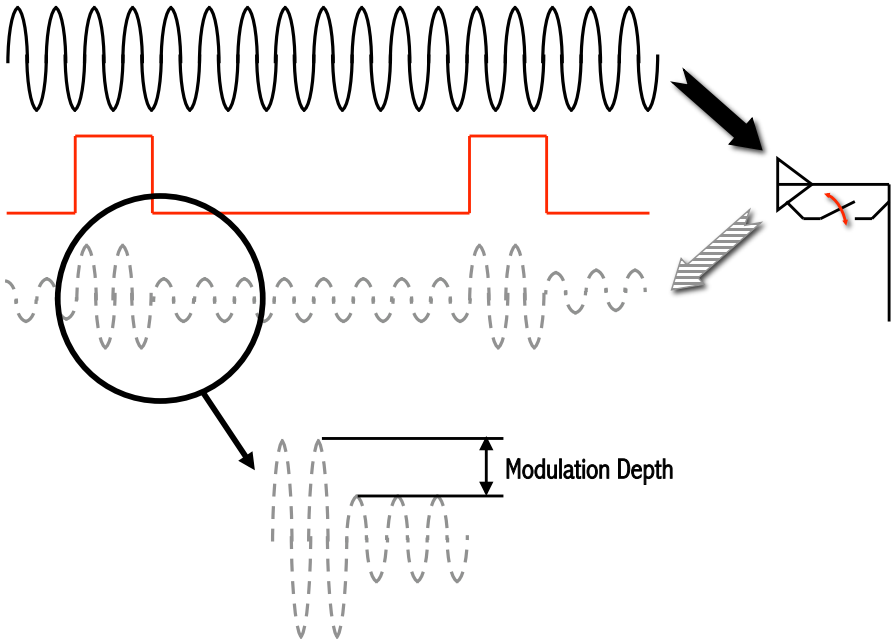

Figure 3.2: Definition of Modulation Depth

Figure 3.3 summarizes the path loss breakdown in a Reflective Impulse

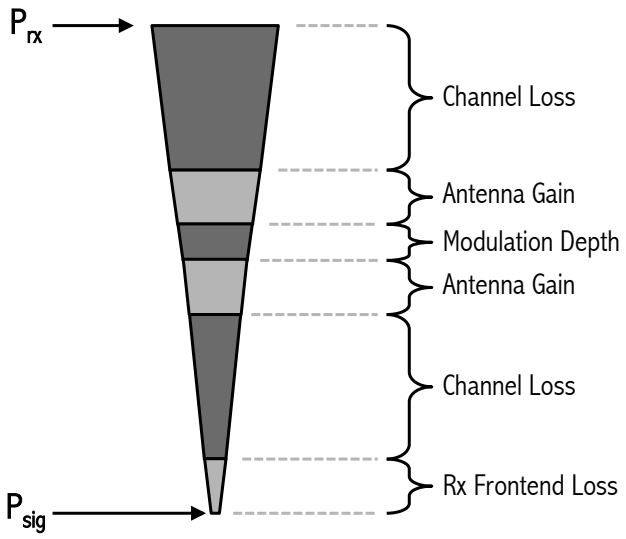

Figure 3.3: Total Path Loss in Reflective Impulse Radios

Radio. Channel loss and antenna gain appear twice, because of round-trip propagation of the wave — first from the receiver to the transmitter then back from the transmitter to the receiver. Define that the carrier power is P_{rx} and power of the signal reflected back to the receiver antenna is P_{sig},

$$\frac{P_{rx}}{P_{sig}} = \frac{1}{L_c^2 \times G_{tx}^2 \times d_M \times L_{rx}} \tag{3.1}$$

where L_c is the channel loss, G_{tx} the transmitter's antenna gain, d_M the modulation depth, and L_{rx} the receiver front end loss.

3.1.2 SNR

While Equation (3.1) may seem straightforward, the parameter P_{sig} deserves more explanation. Unlike the continuous-time carrier, the data signal is reflected in pulses. Its instantaneous power therefore varies over time. P_{sig} in Equation (3.1) is clearly the power within each short pulse. As each pulse represents $\log_2 M$ bits of data, it results in following calculation for energy per

bit:

$$E_b = \frac{P_{sig} \times t_{PW}}{\log_2 M} \tag{3.2}$$

where t_{PW} is the pulse width and M is the number of PPM positions per cycle.

Now that the signal energy is calculated, let's now compute the noise power. Suppose that there is only thermal noise (sources of additional noise will be discussed in next section), its variance is

$$E_{tn} = k_B \times T \tag{3.3}$$

where k_B is the Boltzmann's constant (in joules per kelvin) and T is the absolute temperature (in kelvins). To account for additional noise above the thermal noise floor, a new parameter F_n is defined as the overall noise factor. Total noise variance is then

$$E_n = E_{tn} \times F_n = k_B \times T \times F_n \tag{3.4}$$

SNR at the reflective impulse receiver is

$$SNR = \frac{E_b}{E_n} = \frac{P_{sig} \times t_{PW}}{\log_2 M \times k_B \times T \times F_n} \tag{3.5}$$

From Equations (2.8) and (2.9) in last chapter,

$$t_{PW} = \frac{log_2 M}{M \times R} \tag{3.6}$$

Therefore

$$SNR = \frac{P_{sig}}{M \times R \times k_B \times T \times F_n} \tag{3.7}$$

The convenience of SNR is that one can now relate it to expected system performance. Figure 3.4 shows the theoretical relation between SNR and the probability of error for M-ary pulse position modulated (PPM) radios [35]. As SNR increases, the error probability decreases. For the error probability to be far below 10^{-1}, SNR should be much larger than 5dB. In such strong-SNR regime, a larger M (number of PPM positions per cycle) results in lower error probability, although at a diminishing rate. According to Equation (3.7) on the other hand, to reduce the error probability for a given M, one has to either reduce path loss, improve receiver noise factor, or lower the communication data rate. Depending on the design, these can be difficult tradeoffs.

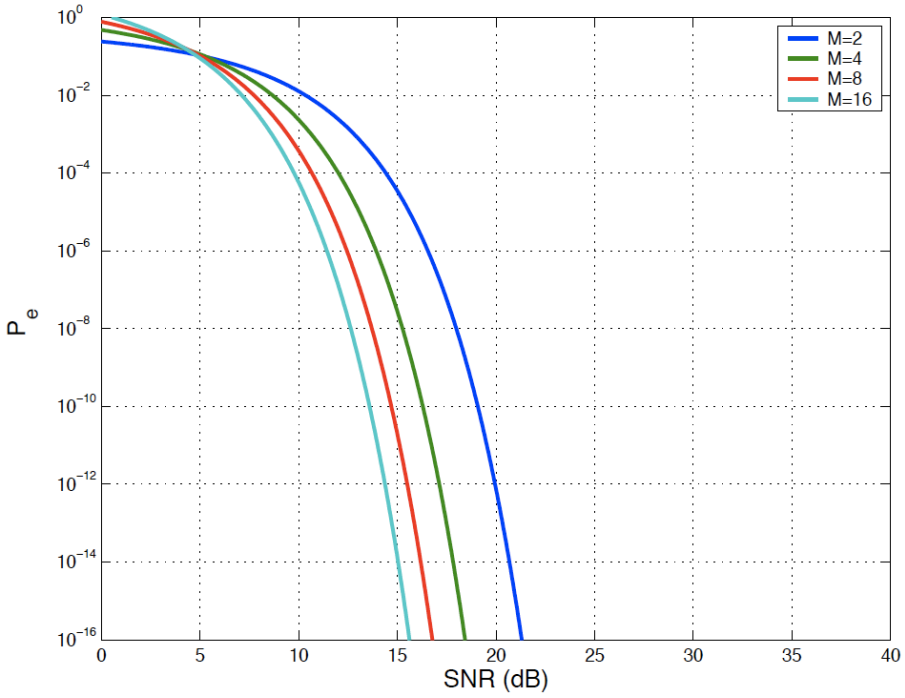

Figure 3.4: Theoretical Probability of Error versus SNR for M-ary PPM [35]

3.1.3 Self Interference

Like all other radios, a Reflective Impulse Radio is subject to interferences. There is however an additional source, self interference, which is unique to reflection-based radios and can cause substantial noise increase above the thermal limit in Equation (3.3). This self interference comes from the high power carrier of the receiver. Unlike that of an active radio, the receiver of a reflection-based radio needs to illuminate the transmitter by radiating a single-tone carrier, which will inevitably leak to the receive path and interfere with the weak signal received. Given that the interference is self generated, the receiver typically contains an interference cancellation block that effectively suppresses the self interference.

While the design of an RIR receiver will be discussed in last section of this chapter, it is important to realize that the abovementioned interference can-

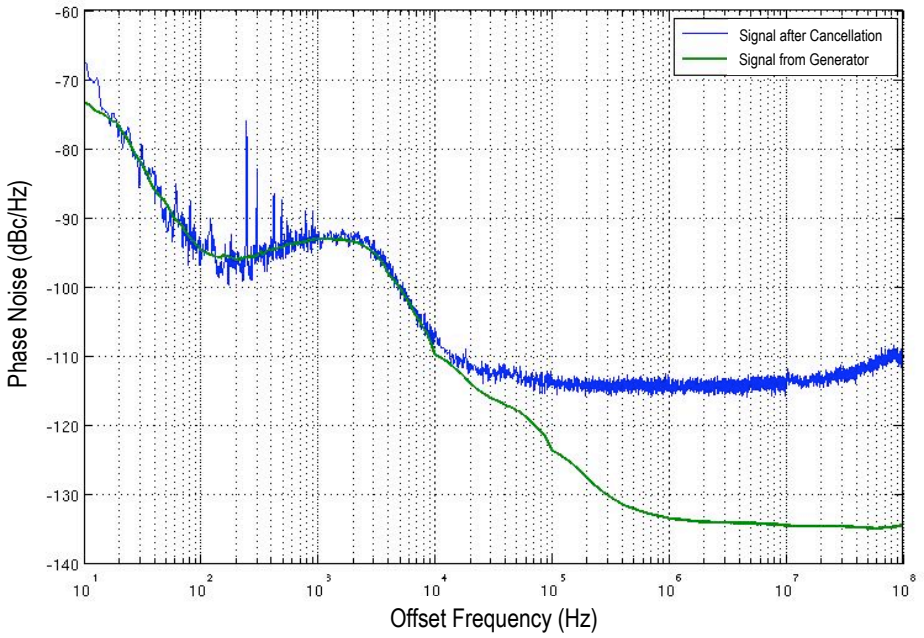

Figure 3.5: Phase Noise before and after Interference Cancellation

cellation is only partially effective in removing the phase noise of the carrier. As an example, Figure 3.5 shows the measured phase noise before and after interference cancellation. At low offset frequencies (below $10kHz$), phase noise is suppressed as much as the carrier itself, resulting in same readings on the dBc/Hz basis. At higher offset frequencies however, phase noise after interference cancellation is as much as $25dB$ above the level before cancellation. Since an RIR radio occupies broad signal bandwidth, one should indeed be concerned by the elevated noise floor at high offset frequencies. This will be further discussed in the "RIR Receiver" section towards the end of this chapter.

3.1.4 Example

Let us now exercise link budget assessment on the implantable neural example.

For safety reasons, the amount of radio power that humans may be exposed to is strictly regulated. Analysis and simulation in [13] reveal that the maximum power allowed for the mm-size neural implant is $56mW$, or $17.5dBm$. Moreover, Figure 3.6 shows the combined channel and antenna loss at different tissue thickness [36]. At the maximum thickness, the combined loss is $-32dB$ at the optimal frequency around $500MHz$.

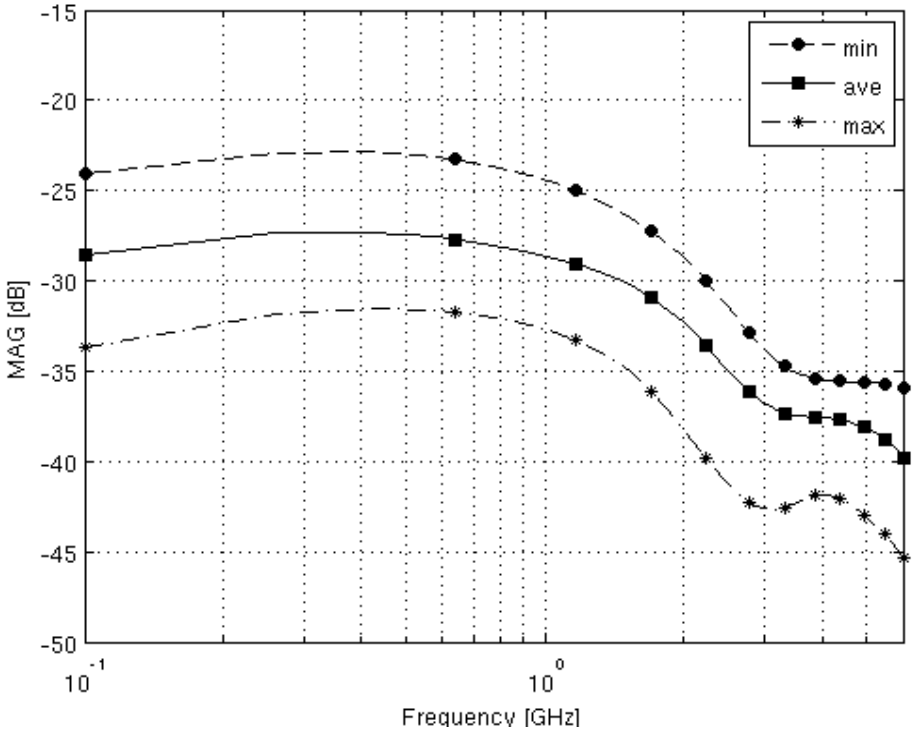

Figure 3.6: Combined Channel and Antenna Loss versus Frequency [36]

Adding above information to parameters in Equation (3.1): $P_{rx} = 56mW$ and $L_c \times G_{tx} = 10^{-3.2}$. Moreover assume that for the first order: $d_m = 20\%$ and $L_{rx} = -3dB$. Therefore

$$P_{sig} = P_{rx} \times L_c^2 \times G_{tx}^2 \times d_M \times L_{rx} = 2.22nW = -56.5dBm \qquad (3.8)$$

To compute SNR using Equation (3.7), let's further assume that $M = 8$, $R =$ 1Mbps, and $F_n = 29$dB. While the phase noise difference is only 20dB in Figure 3.5 (at 1MHz offset), please note that F_n denotes the overall noise level relative to the thermal limit instead of the pre-cancellation signal generator. In other words, phase noise of the signal generator is accounted for in F_n calculation as well. Therefore

$$SNR = \frac{2.22 \times 10^{-9}}{8 \times 10^{6} \times 1.38 \times 10^{-23} \times 300 \times 10^{2}} = 24dB \tag{3.9}$$

Referring above SNR value to Figure 3.4, one can clearly conclude that there is sufficient margin in the link budget, which not only proves the feasibility of employing the Reflective Impulse Radio architecture for the neural application but also allows margins for error in path loss estimation. Moreover, since the link margin is so large, it provides the possibility of cutting back P_{rx} during the communication phase (by for example $15dB$) to increase P_{rx} during the powering phase. This is indeed how the neural example is implemented and the details and advantages of such 2-phase operation will be discussed in Chapter 4.

3.2 Antenna Switch

Main function of the antenna switch is to modulate the antenna impedance with sufficient modulation depth on the reflected signal. Its design constraint on the other hand is limited device size so that the power consumption of its driver is contained. In this section we will first examine the analytical relation between switch size and modulation depth, then discuss the tradeoff between resistive versus capacitive modulation, followed by the neural design example.

3.2.1 Switch Size and Modulation Depth

The on- and off-resistance of a CMOS switch is obviously a function of its size, or channel width. Given the device type however, the ratio of the two resistances is often fixed. Define that the on-resistance is R_{ON} and that the

ratio between off- and on-resistance is r. Then,

$$R_{OFF} = R_{ON} \times r \tag{3.10}$$

Further assume that the antenna impedance is Z_A. The modulation depth d_M is proportional to the difference of the two reflection coefficients. Mathematically

$$d_M = \frac{1}{2} \times \left| \left| \frac{R_{ON} - Z_A^*}{R_{ON} + Z_A} \right|^2 - \left| \frac{r \times R_{ON} - Z_A^*}{r \times R_{ON} + Z_A} \right|^2 \right| \tag{3.11}$$

where Z_A^* is the complex conjugate of Z_A. One can further verify that $d_M \leq 0.5$ for all values of R_{ON} and r in above expression.

While it may not be obvious from Equation (3.11), there actually exists an optimal R_{ON} which maximizes d_M. This is illustrated in Figure 3.7 below. The maximum is achieved when the on-resistance is matched to antenna impedance and the off-resistance provides a good open-circuit (or when the off-resistance is matched to the antenna and the on-resistance provides a good short-circuit).

3.2.2 Resistive vs. Capacitive Modulation

In above analysis, it was assumed that the switch only modulated the resistive part of the antenna impedance. How about the reactive part? One can imagine that there for example can be a capacitor in series with the switch so that when the switch turns on and off the reactive part of the antenna changes as well. Through similar analysis in Section 3.2.1, it can be derived that reactive modulation is equally effective in achieving the maximum modulation depth. Moreover, same percentage change on the reactive part can result in larger increase in modulation depth. This is shown in Figure 3.8. Both y-axes are in relative signal amplitude, which is proportional to modulation depth. However, note that the resistance x-axis (bottom) is in a logarithmic scale but the capacitance x-axis (top) is in a linear scale. While it takes only 50% capacitance change to reach the maximum signal amplitude, same effect requires two orders of magnitude's change in resistance.

Figure 3.8 seems to suggest that capacitive modulation is the favorable approach. Unfortunately there is a major drawback to it: slow transient re-

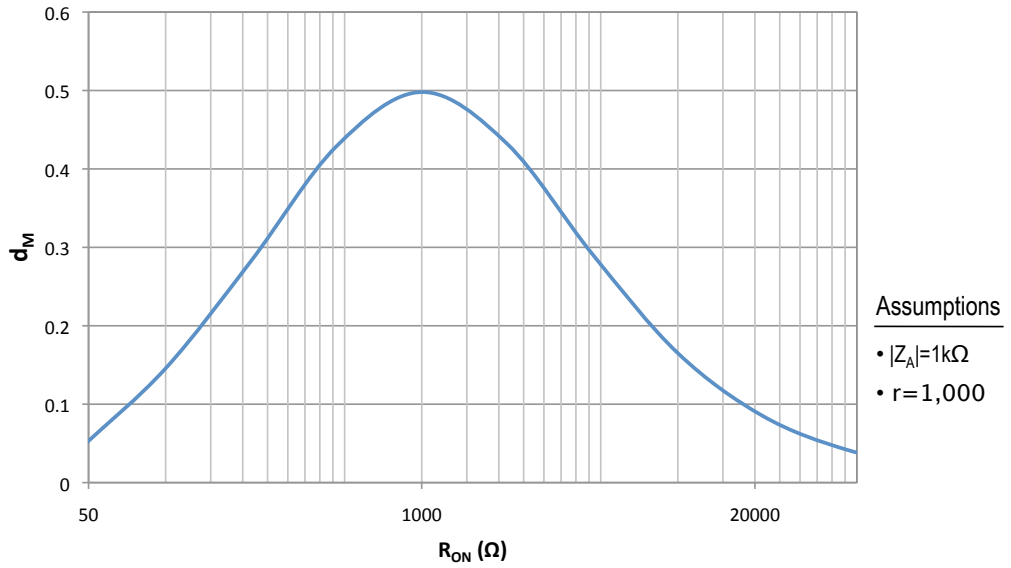

Figure 3.7: Modulation Depth vs. Switch Resistance

sponse. Recall from *Section 2.3 Direct Antenna Modulation* that an antenna can be modeled as a simple resonant tank (Figure 3.9). Changing the capacitance C_A re-tunes the tank's resonant frequency. But as long as the resistance R_A is relatively large, the tank remains to have a high quality factor (Q) and a slow transient response. Contrarily, shorting R_A does not change the tank's resonant frequency. Rather it brings down the quality factor hence speeds up the transient response. This is perfectly equivalent to the bandwidth extension effect of direct antenna modulation in Section 2.3. In Figure 3.10, the left half is the waveforms from capacitive modulation; the right half is from resistive modulation, which apparently has faster response to the switch signal. Moreover even in the resistive case, one can notice that the response is slower at the switch's turn-off instance (second edge) than the turn-on instance (first edge). At the turn-on instance, the resonant tank returns from a low-Q state to the high-Q state, causing the slower response that was also observed and explained in Section 2.3.

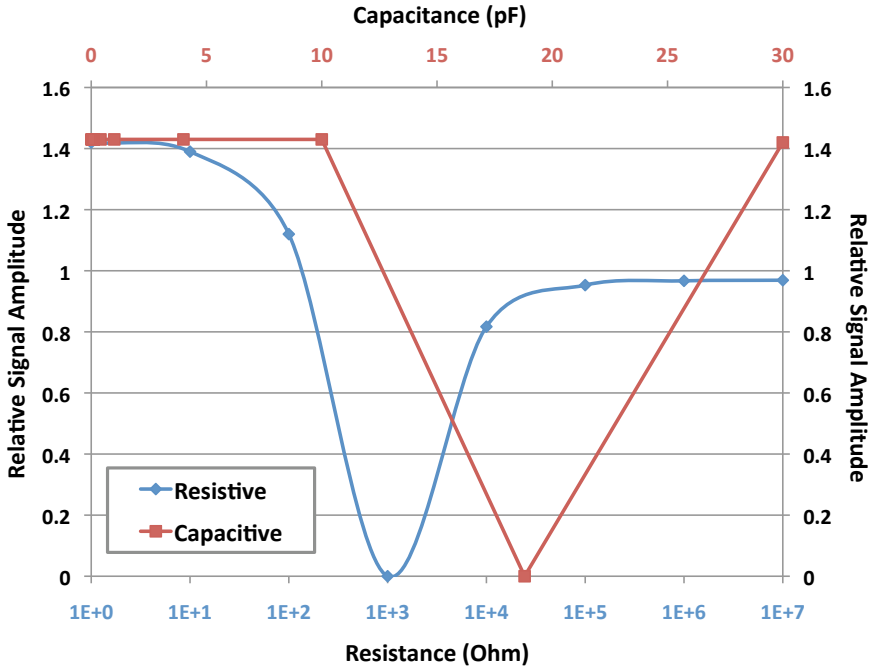

Figure 3.8: Resistive vs. Capacitive Antenna Modulation

3.2.3 Example

There are two choices to be made in the design of the antenna switch. The first is device type, which is related to the parameter r in Equation (3.11); the second is device size, related to R_{ON}. While device types depend very much on the fabrication technology, in general a larger r is preferred for the same device geometry. As for device sizing, Figure 3.7 already showed that there exists an optimal size, which maximizes the modulation depth hence the signal strength. For example, Figure 3.11 plots signal amplitude versus device type and channel width from an example technology. There is clearly an optimal width for each device type. Furthermore, the maximum signal amplitude is higher on the three LP devices in dotted lines than the one GP device in red solid line, although at the expense of much larger device sizes. To trade (marginal) signal loss for (substantial) power savings, the solid-line type was chosen and 10μm was decided to be the final channel width.

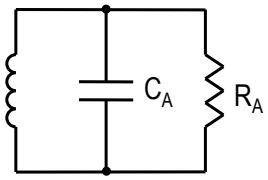

Figure 3.9: Antenna Equivalent Circuit

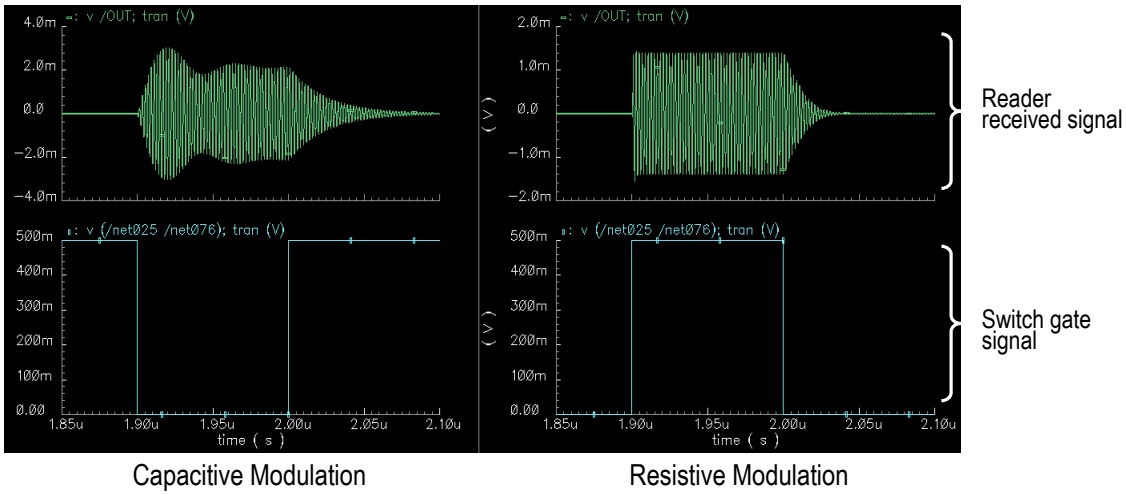

Figure 3.10: Transient Responses of Resistive and Capacitive Modulations

3.3 Pulse Generator

Purpose of the pulse generator is to generate a sequence of pulses with sufficient timing accuracy. Due to stringent power and size limitations however, off-chip references and phase lock loops are obviously infeasible. Ring oscillators and delay lines, although less accurate, become the preferred choice.

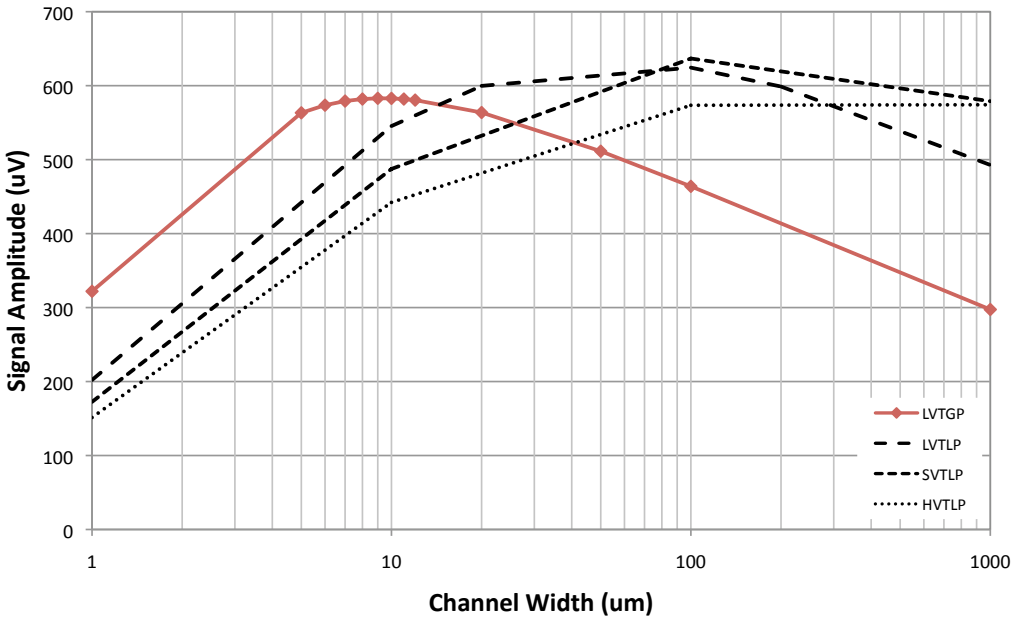

Figure 3.11: Device Sizing Example

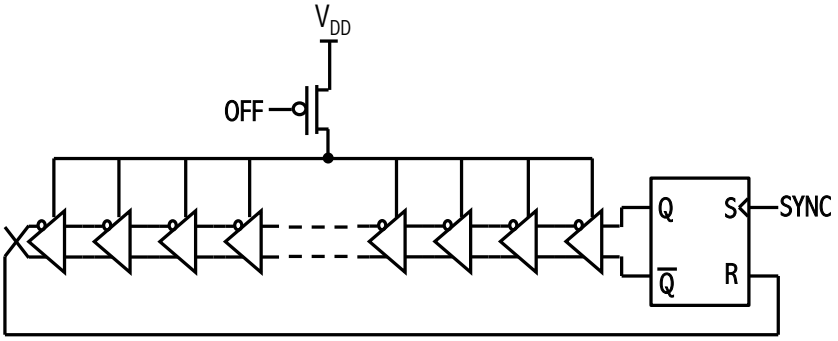

Figure 3.12: Delay Line Example

3.3.1 Delay Line Pulse Generator

Together with some combinational logic gates, an open-loop delay line makes a simple and power efficient pulse generator. Figure 3.12 shows such a design, made of an RS flip-flop and a series of differential logic inverters. Note that the flip-flop's S input is edge sensitive while its R input is level sensitive. The use of differential inverters instead of single-ended ones does not only reduce the number of stages for same output phases but also improves device matching. Finally the header switch connected to voltage rail V_{DD} is for power gating.

Let us now briefly go over the operation of the design in Figure 3.12. At the beginning of each cycle, the $SYNC$ (for *synchronize*) signal issues a 0-to-1 edge, asserting the flip-flop's output Q and de-asserting $\overline{Q}$. These changes then ripple through the inverter chain and reach to the last output, which asserts the flip-flop input R. Consequently both outputs of the flip-flop flip their polarities and propagate the changes once again through the inverter chain. At the end of the propagation, the flip-flop's R input is de-asserted, waiting for the next positive edge on $SYNC$.

Although efficient, a delay line lacks the timing accuracy of an off-chip crystal or even an on-chip L-C resonator. Yet it is still applicable to the reflective impulse radio architecture **only** because the receiver can afford the power and size to track the systemic and random variations in pulse timing. On the other

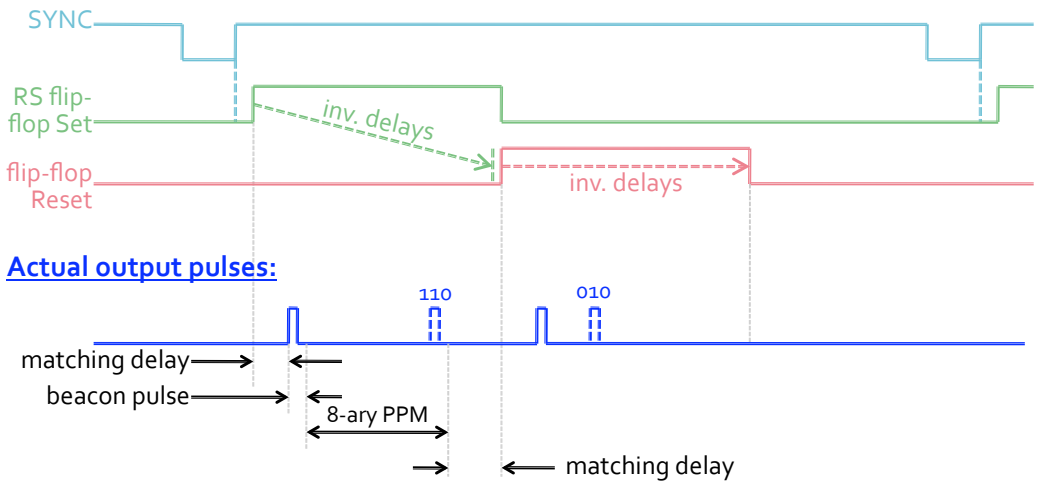

Figure 3.13: Timing Diagram of a Delay Line Based Pulse Generator

hand, simple techniques such as beacon pulses can prove useful in helping the receiver track those variations. These extra beacons not only signal the beginning of a transmission cycle but also provide a reference on expected pulse width. Their circuit overhead is also marginal. Figure 3.13 shows the timing diagram of a delay line based pulse generator where one beacon pulse is added to every half cycle of a transmission session, during which 3 bits (8-ary PPM) are transmitted. Please also note the detail that each beacon pulse also includes a fixed amount of off time (of one pulse width long in this example), which helps separate the beacon from actual data transmission.

3.3.2 Example

There are two elements in the delay line in Figure 3.12: differential inverter and RS flip-flop. Figure 3.14 shows an example of each implementation. There apparently need multiple inverters in cascade. Subsequently an edge combiner takes its inputs from two adjacent inverters and generates a narrow pulse output. Assume that the two differential outputs of the x^{th} inverter are Out_x^+ and

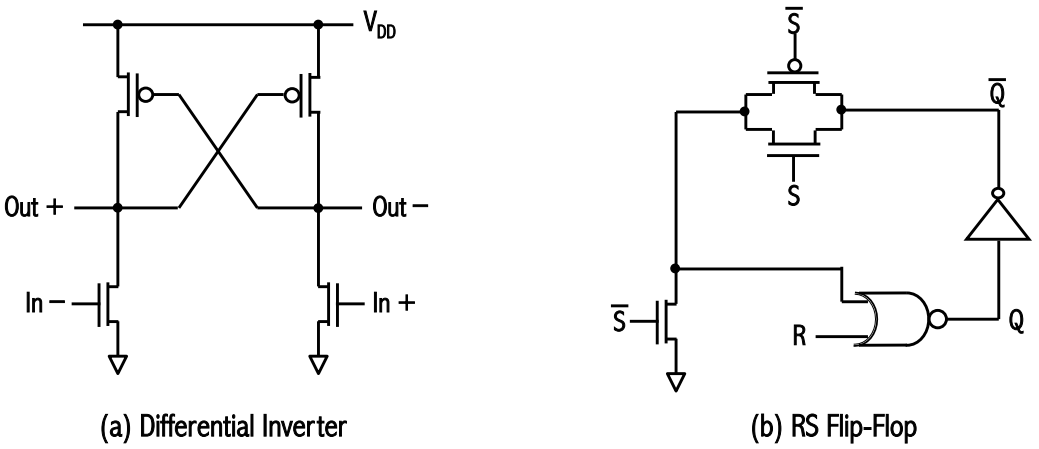

Figure 3.14: Example of Differential Inverter and RS Flip-flip Implementation

Out_x^-. The logic equation for the edge combiner is then

$$Pulse_x = \overline{\overline{Out_{x-1}^+} \cdot \overline{Out_{x-1}^-} \cdot \overline{Out_x^+} \cdot \overline{Out_x^-}} \tag{3.12}$$

Obviously Equation (3.12) can be implemented with some simple inverters and NAND gates.

Besides schematic design, it is also important to pay attention to the layout of the pulse generator. Systemic mismatch between different inverter stages should be minimized, if not eliminated. Similarly loading and driving strength of each inverter should be made as identical as possible. It is therefore necessary to add several dummy stages at the beginning and end of the inverter chain. Latencies caused by these dummy stages are labeled as "matching delay" in Figure 3.13.

Finally, several simulation results are reported in a series of figures and table below. Figure 3.15 shows the simulated waveforms (post layout) of the example design. Five pulse outputs are plotted together with the $SYNC$ input, which initiates each data transmission cycle. Table 3.1 summarizes the pulse generator's performance over process and supply corners. Power consumption under the worse case is 140nW, a reasonable fraction of the 1μW budget for the entire transmitter. In the typical process case with the nominal supply of

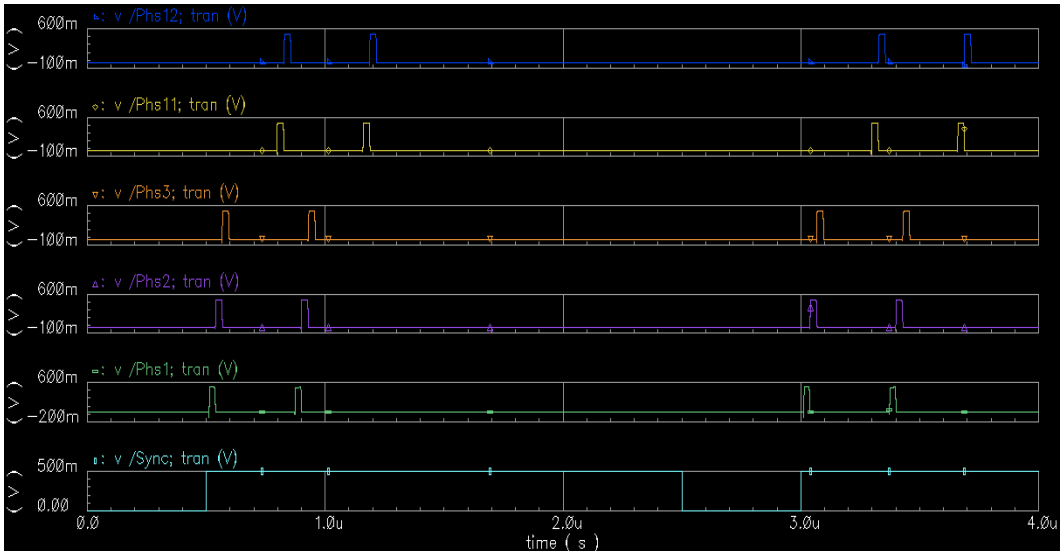

Figure 3.15: Simulated Waveforms of an Example Pulse Generator

500mV, Figure 3.16 shows the variation in pulse width caused by thermal noise, as well as pulse width mismatch between beacon and data pulses. Thermal induced variation is approximately ±2% while the standard deviation of pulse mismatch is almost 10% of pulse width.

	Pulse Width	Power Consumption
Slow, $V_{DD} = 450mV$	70 ns	44 nW
Typical, $V_{DD} = 500mV$	28 ns	83 nW
Fast, $V_{DD} = 550mV$	14 ns	140 nW

Table 3.1: Simulated Pulse Width and Power Consumption of an Example Pulse Generator

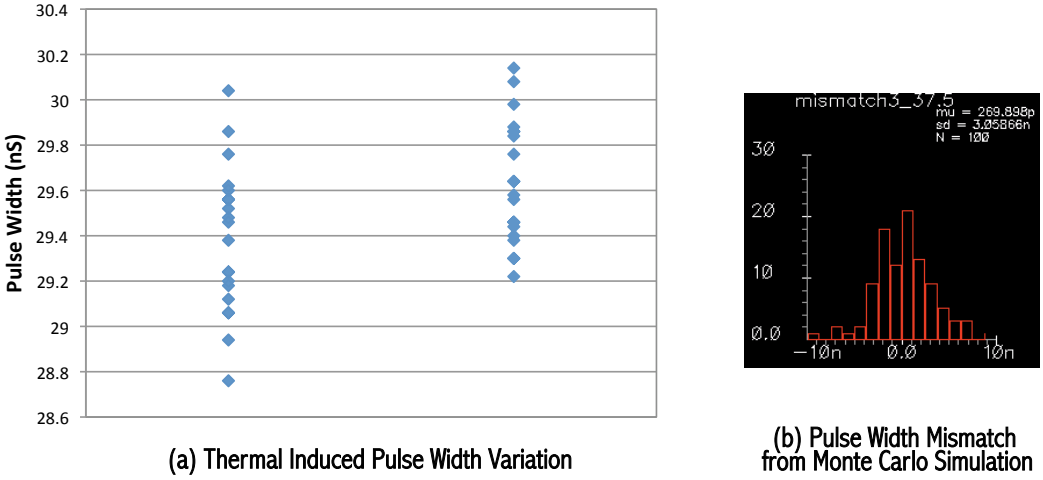

Figure 3.16: Simulated Pulse Width Variation and Mismatch

3.4 PPM Encoder

3.4.1 Pass Transistor PPM Encoder

As mentioned previously in Chapter 2, a simple and energy efficient approach to implementing the pulse position modulation (PPM) encoder is using pass transistor logic. Figure 3.17 shows its schematic (for an 8-ary PPM example). Inputs $Q1$–$Q3$ and $\overline{Q1}$–$\overline{Q3}$ represent a 3-bit base band signal. The other inputs are $Pulse0$–$Pulse7$ from the pulse generator. Based on the 3 base-band bits, one of the 8 input pulses is selected and sent to the output.

3.4.2 Example

Although the number of transistors seems vast ($6 \times 8 = 48$) in Figure 3.17, layout of the entire PPM encoder can be fairly compact. Every 3 transistors in series can be placed on a single active stripe, since no contact is needed in between. Figure 3.18 shows an example of the layout. Total area of all active

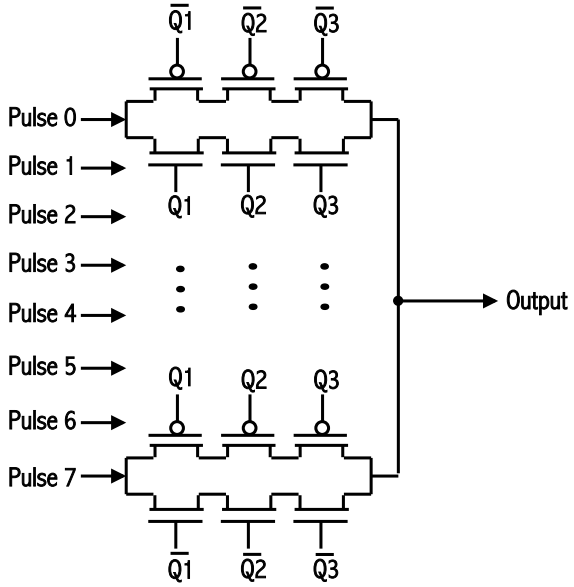

Figure 3.17: Pass Transistor PPM Encoder Schematic

devices is actually smaller than the area for interconnects, where one layer of poly and two layers of metal are readily employed. Additionally, thanks to its passive nature, the power consumption of the PPM encoder is nearly negligible (<5nW). The simulated propagation delay is less than 10ns, far shorter than the approximately 1μs allocated (half cycle of a transmission session).

Now that all key elements of a reflective impulse transmitter have been reviewed, we can construct the block diagram of the entire transmitter (Figure 3.19). Except for the off-chip antenna (in gray), all other circuits are integrated on chip. This design in Figure 3.19 was actually implemented and fabricated. Detailed test results will be reported in Chapter 4.

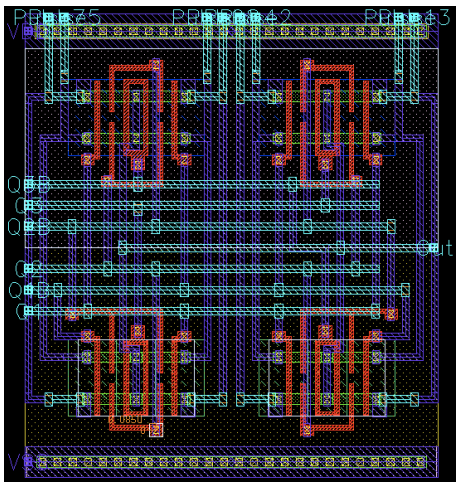

Figure 3.18: Layout of a Pass Transistor PPM Encoder

3.5 RIR Receiver

From the beginning of the thesis, a point has been made that the emphasis of future sensor network applications is on the transmitter side. No radio however is complete without a receiver. In this last section of the chapter, we will also explore the design of a reflective impulse receiver.

Figure 3.20 below shows a simplified receiver diagram. For the first pass, let us ignore the circuits in blue. The signal generator on the left generates a continuous wave sinusoid, which is subsequently amplified by the Power Amplifier (PA). The circulator in the middle is a critical component in the system. On one hand, it passes the PA output to the matching network, then to the antenna. On the other hand, it — in the ideal case — prevents the PA output from leaking into the Low Noise Amplifier (LNA). Likewise, when the received signal travels from the antenna through the matching network, a good circulator passes most of the signal towards the LNA, with little leakage back to the PA. Finally the signal is amplified by the LNA then sampled by an Analog-to-Digital Converter (ADC), ready to be post processed for data recognition.

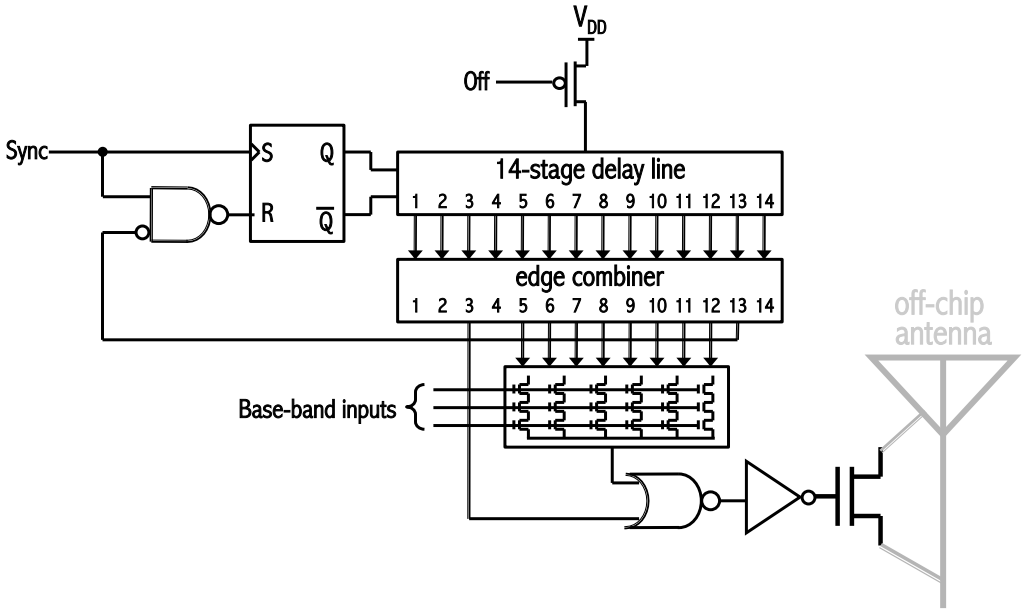

Figure 3.19: Reflective Impulse Transmitter Block Diagram

Please note that Figure 3.20 is only a simplified example of many possible configurations. The ADC's anti-aliasing filter for instance is not shown. Moreover, there can be a mixer after the LNA when the ADC sampling speed is not high enough for the carrier frequency. Circulators and directional couplers are often inter-changeable, depending on the device model and product specification. However the operation principle of these varieties should all be similar.

While it may appear simple, there is a major challenge in Figure 3.20, coming from the fact that the continuous wave carrier is easily 70dB or higher than the received signal. Any leakage from the carrier becomes a strong interference that needs to be substantially suppressed before reaching the LNA and saturating its linearity range. The circuits in blue are for that exact purpose.

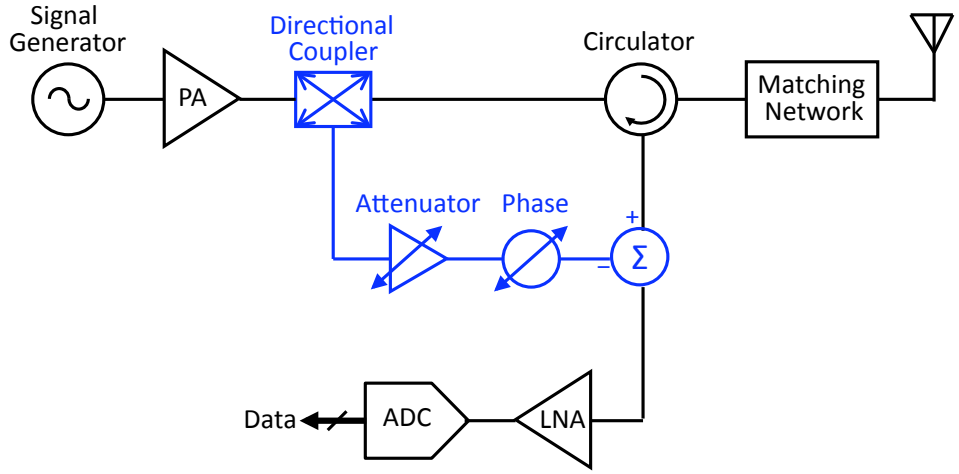

Figure 3.20: Simplified Block Diagram of a Reflective Impulse Receiver

3.5.1 Self Interference Cancellation

Purpose of the circuits highlighted in blue color in Figure 3.20 is for self interference cancellation (it is referred "self" because the interference is generated by the receiver itself instead of any external sources). Its operation is relatively simple. The directional coupler first diverts a small fraction of the carrier through the programmable attenuator and programmable phase shifter. The output of the shifter is therefore a sinusoid with any desired phase and amplitude. This sinusoid then joins the circulator output, which contains the undesirable interference, at the power combiner with "+" and "−" signs. When the programmable sinusoid matches the phase and amplitude of the interference, a great portion of the self interference can be canceled out, leaving a relatively clean signal to the input of the LNA.

The effectiveness of self interference cancellation is clearly a function of the resolutions of the programmable attenuator and phase shifter. This relation is plotted in Figure 3.21 from a similar system used for image rejection applications [37]. With 1dB of amplitude imbalance and 10° of phase imbalance for example, 20dB of interference suppression can be expected. If the resolutions improve to 0.1dB and 0.1°, the cancellation effect can exceed 40dB.

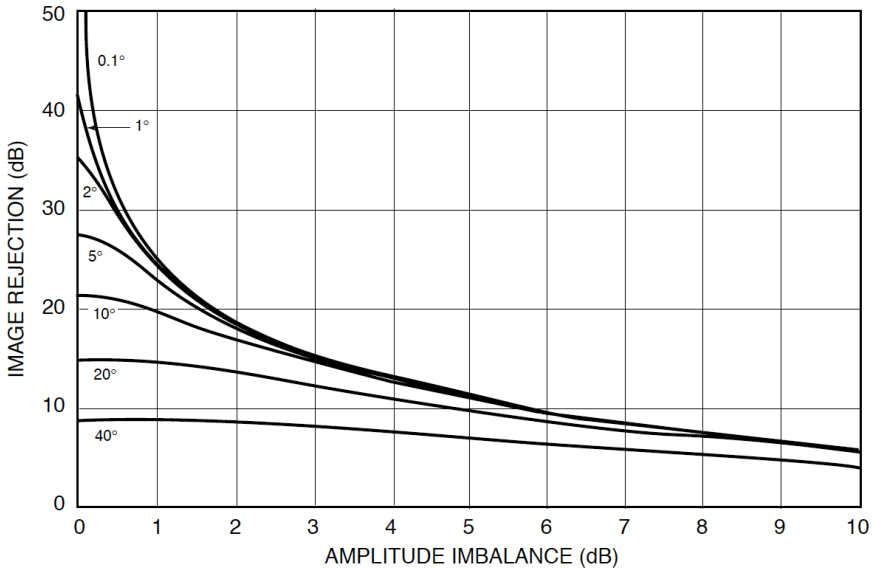

Figure 3.21: Interference Suppression vs. Phase and Amplitude Imbalance [37]

Let us now take a step back and re-examine where exactly the self interference comes from. There are actually three distinctive paths that the carrier can leak to the circulator's output. The first is the less-than-ideal isolation of the circulator in Figure 3.20. The second is the impedance mismatch between the circulator and the matching network. The fraction of the carrier that gets reflected back at this interface re-enters the circulator and appears at its output. The last path is the impedance mismatch between the matching network and antenna. Similar to the second path, the reflection at this interface travels back through the matching network and the circulator with little attenuation and becomes a source of interference.

Given that there are three leakage paths of self interference, naturally arises this question — *can they be cancelled by a single cancellation loop, like the one in Figure 3.21?* Fortunately the answer is *yes*. And following is the proof.

Using recursive derivation, suppose at first that there are only two interferences of same frequency but different phase and amplitude. The sum of the

two is then

$$A_1 \times sin(\omega t + \phi_1) + A_2 \times sin(\omega t + \phi_2)$$

From basic trigonometry

$$sin\alpha + sin\beta = 2sin\frac{\alpha+\beta}{2}cos\frac{\alpha-\beta}{2}$$

Therefore

$$\begin{aligned}
&A_1 \times sin(\omega t + \phi_1) + A_2 \times sin(\omega t + \phi_2) \\
&\quad = \tfrac{A_1+A_2}{2}[sin(\omega t + \phi_1) + sin(\omega t + \phi_2)] + \tfrac{A_1-A_2}{2}[sin(\omega t + \phi_1) - sin(\omega t + \phi_2)] \\
&\quad = (A_1 + A_2)cos(\tfrac{\phi_1-\phi_2}{2})sin(\omega t + \tfrac{\phi_1+\phi_2}{2}) + (A_1 - A_2)sin(\tfrac{\phi_1-\phi_2}{2})cos(\omega t + \tfrac{\phi_1+\phi_2}{2})
\end{aligned}$$

Now define

$$\begin{aligned}
(A_1 + A_2)cos(\frac{\phi_1 - \phi_2}{2}) &\triangleq Y_1 \\
(A_1 - A_2)sin(\frac{\phi_1 - \phi_2}{2}) &\triangleq Y_2
\end{aligned}$$

Note that both Y_1 and Y_2 are constants, independent of frequency or time. Then the combination of the two is also a constant:

$$\sqrt{Y_1^2 + Y_2^2}$$

Let

$$\varphi \triangleq arccos\frac{Y_1}{\sqrt{Y_1^2 + Y_2^2}}$$

Then

$$\begin{aligned}
& A_1 \times sin(\omega t + \phi_1) + A_2 \times sin(\omega t + \phi_2) \\
= \;& Y_1 sin(\omega t + \frac{\phi_1 + \phi_2}{2}) + Y_2 cos(\omega t + \frac{\phi_1 + \phi_2}{2}) \\
= \;& \sqrt{Y_1^2 + Y_2^2} \times [cos\varphi sin(\omega t + \frac{\phi_1 + \phi_2}{2}) + sin\varphi cos(\omega t + \frac{\phi_1 + \phi_2}{2})] \\
= \;& \sqrt{Y_1^2 + Y_2^2} \times sin(\omega t + \frac{\phi_1 + \phi_2}{2} + \varphi) \qquad (3.13)
\end{aligned}$$

Equation (3.13) proves that the sum of two sinusoids of identical frequency is still a sinusoid of the same frequency. By the rule of recursion, one can easily

prove that the sum of three, four, ... and more sinusoids is still a sinusoid, as long as they have the same frequency. Therefore, a single cancellation loop like the one in Figure 3.20 is sufficient in suppressing all interferences combined from multiple paths.

3.5.2 Phase Noise

Above analysis shows that a single cancellation loop is sufficient in canceling all interference combined from multiple paths. The situation with phase noise on the other hand is less fortunate. There are two reasons responsible for the bad news. First, by the nature of random process, phase noise at different time instances does not correlate. Second, when the bandwidth of any front end device (antenna, matching network or circulator) is narrower than that of the reflected signal, phase noise from different paths displays different spectral characteristics. These two aspects will be explained below in greater detail.

First consider the experiment in Figure 3.22. It resembles the receiver diagram in Figure 3.20 but with some modifications. Power of the single-tone carrier from the signal generator is first split between the top branch with a programmable attenuator and the bottom branch with a fixed attenuator and a programmable phase shifter. These two branches then reunite at the hybrid power combiner like the one in Figure 3.20 and are subsequently amplified by a cascade of LNAs. The final output is sent for measurement.

For carrier cancellation to occur, the amplitude of the top and bottom branch obviously has to match. Their phase, on the other hand, can be 0°, or ±360°, ±720° ... apart. This was indeed verified in experiment. As long as the phase difference was a multiple of 360° (including 0 and negative multiples), carrier cancellation of identical effectiveness was observed. What may appear as a surprise however is their different effect on phase noise. The simulation result, which was also verified by hardware test, is shown in Figure 3.23. For better focus on the main issue, no additional noise other than the signal generator's phase noise was included in this simulation. As can be seen, phase noise cancellation is achieved across the broad bandwidth **only** when the phase difference is 0°. For all other cases (±360°, ±720°, and ±1080°), cancellation is limited to below 1MHz of offset frequency. At increasingly higher frequencies,

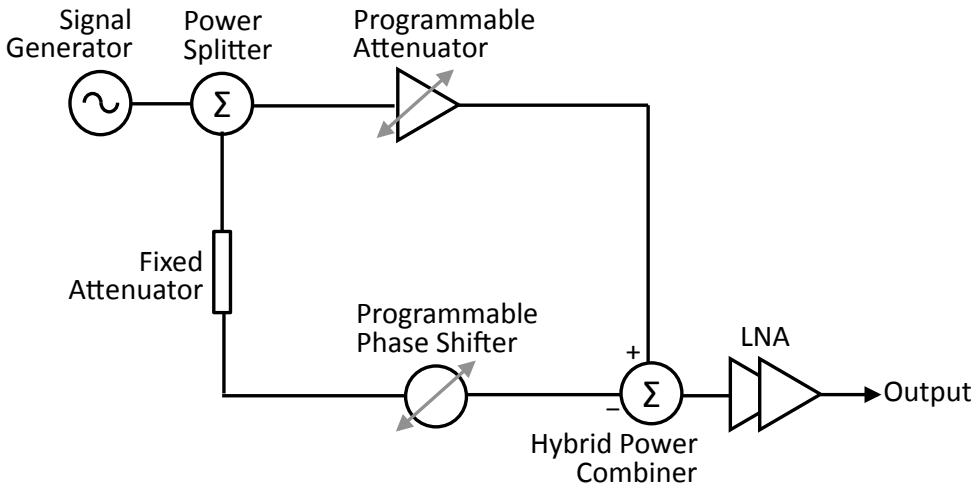

Figure 3.22: Phase Noise Experiment with Single Path Interference

the effect of cancellation degrades.

What is the reason for Figure 3.23? It is the lack of correlation of phase noise at different time instances. Indeed the level of its self correlation is a function of the offset frequency. Imagine phase noise as a small phase modulation on top of the large carrier. When the modulation speed is slow (low offset frequencies), the phase at one time instance is more likely correlated with that at next carrier cycle (for the 360° case), or that of two cycles before or after (the ±720° case). Phase noise is therefore more likely to be canceled. When the modulation speed is fast (high offset frequencies), phases are less correlated and canceling phase noise with a delayed version of itself is less possible. On the other hand, when there is no delay at all (the 0° case), phase noise is cancelled to the same effectiveness as carrier cancellation and across the broad frequency range.

In the experiment above, there at least existed a 0° case where the carrier and its phase noise were both cancelled. However the difference between Figures 3.22 and 3.20 is that there are 3, instead of 1, interference paths in an actual reflective impulse receiver. One may thus wonder whether there still exists such a "magic" 0° case that cancels both interference and its phase noise.

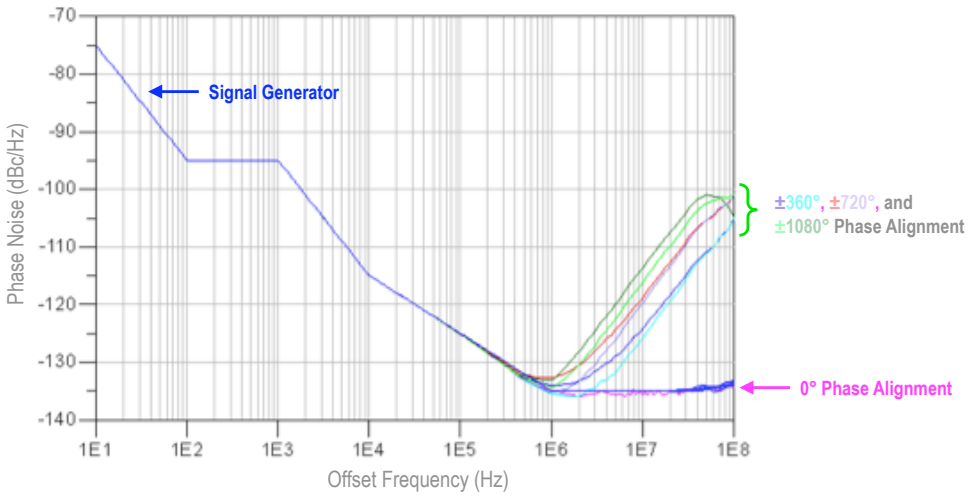

Figure 3.23: Phase Noise Results with Single Path Interference

The answer unfortunately is no; not with a single cancellation loop like Figure 3.20. At the point where all three interference paths re-unite, each has its own phase noise with different time delay from the source, uncorrelated with each other. Furthermore, the blue loop has its own phase adjusted for interference cancellation, not aligned with any of the three paths. The net result is little phase noise cancellation beyond 10kHz, already demonstrated in Figure 3.5.

Actually lack of noise correlation is only partially responsible for the result in Figure 3.5. The other part is the bandwidth limitation of the receiver front end, which is also a fundamental difference between the reflective impulse receiver and an RFID reader. Imagine for instance that the received signal has a bandwidth of 10MHz but the matching network has only 1MHz. There will obviously be loss of signal. But additionally phase noise of the interference returning from the circulator-matching network interface will have a different spectral characteristic than that leaked directly from the circulator. In other words, the matching network will "color" the phase noise beyond its bandwidth, which will certainly make noise cancellation even less possible.

In summary, phase noise is difficult to cancel across the broad frequency

band. Unfortunately broad bandwidth is what is required for reflective impulse radios. There are simple and complex ways to mitigate the problem. One can for example add a band pass filter after the signal generator to tame the phase noise from its source, although narrow-band filters with a sharp roll-off often have high insertion loss too. More complex schemes will be discussed in the next section for future research.

Finally before we conclude on phase noise, it is also worthwhile to point out that in all above discussions we have referred all noise associated with the signal generator as its phase noise. That is convenient, but not necessarily all precise. Note that in both Figures 3.5 and 3.23, the generator's curve has approximately two slopes to it — the first is roughly a $1/f$ slope (where f represents offset frequency) up to 1MHz; from 1MHz and beyond, the slope is relatively flat. In a more strict sense, only the first part is qualified as "phase noise", stemming from the signal generator's internal clock reference. The flat portion is sometimes referred as "pedestal noise", caused by the amplification stage after the reference. Due to its broad bandwidth, a reflective impulse radio often lands majority of its signal on the flat portion of the noise curve. So strictly speaking, it is the pedestal noise that one should combat against in designing an RIR receiver.

3.5.3 Suggestions for Future Research

Mentioned previously, the receiver of a reflective impulse radio resembles that of an RFID. There is however a key difference in signal bandwidth, which in turn affects their noise performance. Additionally, for the purpose of neural (and other) applications, it is much desired to also contain the size and power of the receiver to a form factor wearable by future patients (recall the belt unit in Figure 1.1). This last section of the chapter ventures some thoughts in that direction.

First, downsizing the receiver requires a high level of integration, which poses a great number of challenges but also offers some opportunities for improvement. For example, one reason for the phase noise problem is the existence of multiple interference paths. A potential solution is therefore multiple cancellation loops, each with its own programmable attenuator and programmable

phase shifter. While this is hardly probable with all discrete components, the possibility with integrated circuits, especially with sophisticated equalization and signal processing techniques, is not zero. Integrated implementation of course prefers the signal in the I (in-phase) and Q (quadrature) format instead of amplitude and phase. But it is not unimaginable that one may be able to measure the delay and amplitude of each interference path using some technique similar to channel equalization then set the programmable I and Q factors accordingly. Requirements on complexity and resolution, among other issues, are certainly to be examined. However doesn't an integrated circuit work at its best when handling complex computation problems?

Second, there are significant challenges to realizing a highly integrated receiver. A quality signal source is one of them. Even with the aid of an external crystal reference, the phase noise of an integrated clock is relatively high. Adding a band pass filter can help, as long as its insertion loss does not offset the benefit of out-band attenuation. Either as a resonator or as a filter, novel MEMS devices like [38] and [39] may offer some unique assistance.

Finally, components such as circulator and directional coupler may better be left off-chip. However, instead of using them off the shelf, one should also explore the feasibility of optimization and customization for at least following two reasons. First, off-the-shelf components often have their performance tradeoffs (e.g. a circulator's bandwidth vs. insertion loss and isolation) readily designed for other generic applications. Second and more importantly, customization offers another degree of freedom to solving some of the challenging problems. As previously mentioned, the other cause of the phase noise problem is the bandwidth limitation of front-end devices like the matching network. It has to be narrow band because of the large impedance ratio between the antenna and the circulator, which has the industry standard 50Ω for general compatibility. When the circulator's impedance also becomes a design variable, new opportunities may emerge in taming the phase noise of a reflective impulse receiver.

Chapter 4

Results

The design example in Chapter 3 was actually fabricated into an integrated circuit. This chapter reports measurement results from the test chip. In fact this chip integrates not only the data transmitter but also a wireless power rectifier. Together with an off-chip miniature antenna, it constitutes a completely self-contained and energy-neutral system that achieves record level of power efficiency and size reduction, providing promise for mm-scale wireless neural sensors.

In this chapter, we will first review the architectural design of the entire system. The close interaction between the data transmitter and power regulator makes it necessary to co-design these two parts at both architectural and circuit levels so that the overall system performance is optimized. We will then examine the implementation of the data transmitter itself. Subsequently, measurement results of the transmitter's power consumption, data rate, and communication distance are all presented. Opportunities for future improvements are also proposed in the end.

4.1 System Design

The primary goal of the prototype system is to demonstrate the feasibility of a mm-scale wireless neural transponder. The term "transponder" refers to the fact that it contains a power regulator and a data transmitter but not the signal acquisition function. Figure 4.1 shows the system diagram, consisting of a CMOS chip underneath a two-loop antenna made of a micro PCB (printed circuit board). They are assembled together using flip-chip technologies. The overall dimension is approximately $1\times1\times1$ mm^3. From left to right in Figure 4.1, the transponder includes a tuning capacitor that resonates with the antenna, an on/off switch for antenna modulation, a RF to DC converter, an energy storage capacitor, and a DC to DC regulator including its voltage references. In the middle of the diagram, there are two components: a synchronizer, the purpose of which will be detailed in next section, and a power-on reset block, which ensures that during the initial start-up all circuits are shut off until the regulator output is fully charged. Finally down below, there is the data transmitter TX.

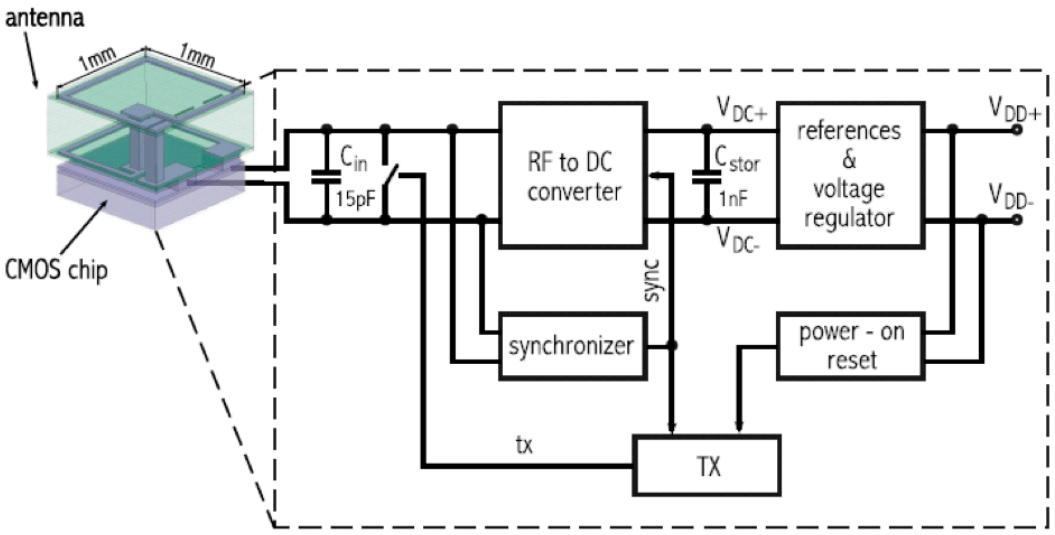

Figure 4.1: System Diagram of the mm-scale Neural Transponder

4.1.1 Two-Phase Operation

In the link budget analysis in Chapter 3, it was discovered that there is sufficient margin in the SNR, allowing a reduction in the carrier power during data transmission. Such reduction in power has substantial advantages. First, it exposes the brain to a reduced level of electromagnetic radiation. But more importantly, it provides a viable solution to a critical challenge in the neural transponder system design — power delivery.

For health and safety reasons, the amount of radiation that the human brain can be exposed to is strictly regulated, imposing two significant challenges to power delivery. First, it limits the amount of RF energy available for rectification. Second and less obviously, the efficiency of RF-to-DC rectification is proportional to the RF amplitude [40]. When the carrier power is low, the rectifier's DC output is lower by an even larger factor. This is obviously undesirable.

A solution to above power delivery challenge is the two-phase operation, enabled by the large link margin in data communication. Additionally it is important to note that safety regulations mentioned above are designed to limit temperature rise on biological tissues hence regulate the electromagnetic exposure on a time averaged basis [41, 42]. As long as the average RF power remains same, a degree of design freedom can be had in how that power is spread over a period of time.

Figure 4.2 shows the details of the two-phase operation. During the power phase, the incident carrier power is set to a relatively high level for efficient RF-to-DC rectification. During the communication phase on the other hand, $P_{carrier}$ is reduced to a substantially lower level, barely enough for data transmission. Indeed $P_{carrier}$ has become so low in this prototype system that it is impractical to rectify this power during the communication phase. Actual duration of the power phase is 600 ns; that of the communication phase is 2.4 μs. An on-chip circuit ("synchronizer" in Figure 4.1) has been designed to detect the change in power level then generate the "*sync*" signal. Data are transmitted only when *sync* is high; the transmitter is turned off when *sync* is low.

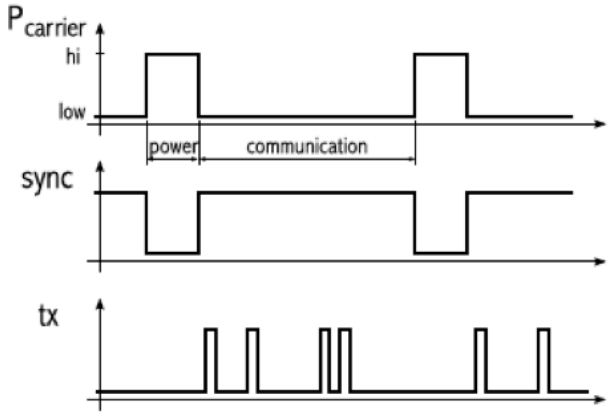

Figure 4.2: Timing Diagram of the Two-Phase Operation

4.1.2 Regulator-Transmitter Co-Design

Above two-phase operation illustrates an example where the design margin in data transmitter helps to solve a critical issue in power delivery. There are other cases throughout the system that call for such intimate interaction in the design practice.

(1) Parallel Impedance

Reflective Impulse Radios transmit information by modulating the antenna between the on- and off-states. Since the switch is in parallel with the RF-to-DC converter and the synchronizer (Figure 4.1), its off-state impedance is upper bounded by the other two components as well. The input impedance of the synchronizer is typically very high hence negligible; that of the converter however is comparable to the antenna, limiting the effective modulation depth.

Once again the two-phase operation offers a relief to the problem. Because there are two phases for distinctive functions, the RF-to-DC converter is now allowed to be disconnected from the antenna during the communication phase. The switch off-state impedance is no longer constrained by the parallel components, boosting the modulation depth and signal strength.

(2) Supply Induced Timing Variations

Since the data transmitter is powered by the voltage regulator, ripples and noise on the supply rail inevitably introduce variations to the transmitter's timing performance, especially in its pulse width. The first type of variation is systematic. Because the regulator's output capacitor is charged during the power phase then discharged during the communication phase, the voltage across it displays a periodic ripple. As a result pulses sent earlier in the communication phase are narrower than those sent later. The second type of variation is random. Any noise on the supply rail obviously affects the timing and pulse width of the transmitter.

A simple solution to the supply problem is to use as much as possible decoupling capacitance. Location and layout of decoupling capacitors are equally important too. Additionally, minimizing the transmitter's power consumption not only conserves energy but also reduces the ripple on the supply rail hence improves timing uniformity of the transmitter itself. In a way, it is one stone with two birds. Finally the addition of beacon pulses helps the decoder to calibrate and address the variation issue from the receiver side.

(3) Time Scale

Reported previously, the power phase's duration is 600 ns and the communication phase's duration is 2.4 μs. How were they designed? There are a multitude of factors involved.

First, the total period (3 μs) should be far less than the averaging time constant specified in health and safety regulations [41, 42]. Second, the communication phase's duration should be long enough to accommodate supply and process induced timing variations (fortunately there is little variation in temperature for the implanted neural application). Third, as there are a fixed number of pulses per cycle, the total time period should be short enough to support the communication throughput. Fourth, it is desirable to operate the power phase with a small duty cycle, so that the carrier amplitude can be high and power rectification efficiency can be decent. On the other hand however, it always takes finite time to enter and exit the power phase. This time overhead can be significant when the period is short and power duty cycle is small.

Needless to say, the final design choice was a balancing act of all factors considered.

(4) Power On Reset

Purpose of the Power On Reset function is to shut down the transmitter during initial power up. Otherwise, not only would the transmitter malfunction; the power regulator could also hang at an intermediate level, unable to charge to the full voltage potential. When the Power On Reset signal is high, the transmitter's head switch is turned off, allowing only nA of leakage current to be drawn from the power regulator.

(5) Test and Verification

The close interaction between power delivery and data communication is also required during the test and verification stage of the system. It involves the details of voltage trimming, SYNC threshold setting, front-end characterization, etc.

Figure 4.3 below shows the photograph of the mm-scale neural transponder next to a US cent, under a microscope. What is seen from this top view is the transponder's micro PCB antenna.

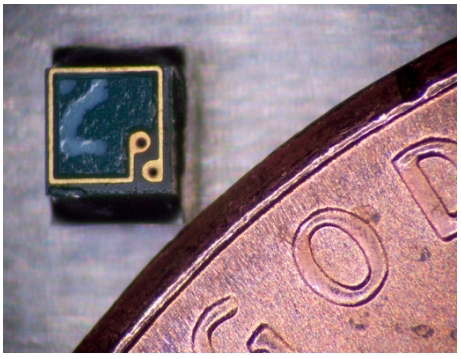

Figure 4.3: Photo of the mm-scale Neural Transponder

4.2 Transmitter Implementation

Figure 4.4 shows the actual implementation of the data transmitter. Compared with Figure 3.19, the only addition is the 3-stage LFSR (Linear Feedback Shift Register) for generating pseudo-random data patterns to emulate the base band input. Figure 4.5 shows the layout of the data transmitter. All components included, its total area is smaller than $30\mu m \times 80\mu m$.

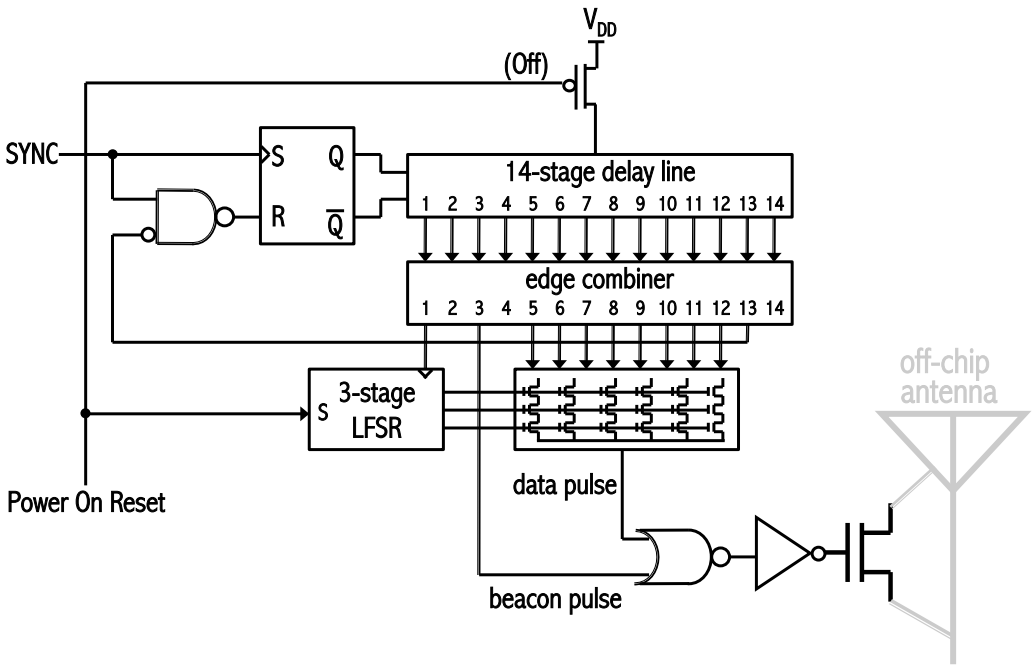

Figure 4.4: Data Transmitter Block Diagram

4.3 Test Results

Detailed test results including basic functions, communication range and energy efficiency will be reported in this section. But first, let us review the receiver architecture to understand how the transmitter is tested.

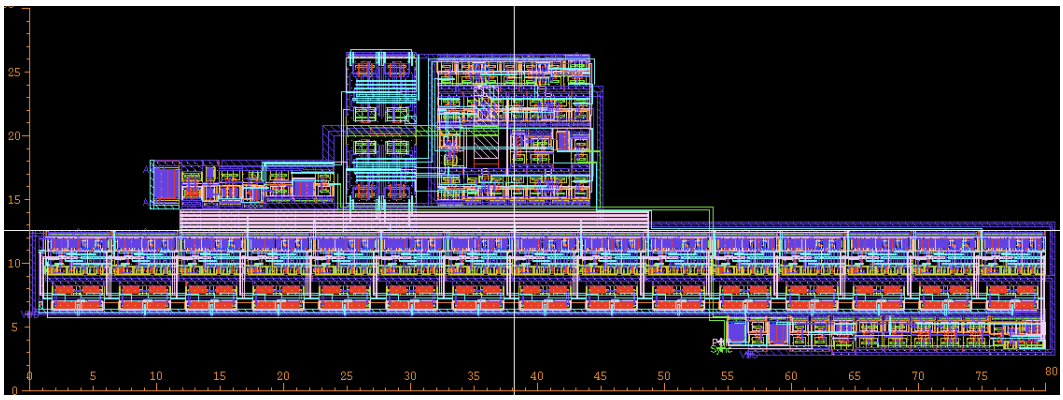

Figure 4.5: Data Transmitter Layout

4.3.1 Receiver Architecture

Figure 4.6 shows the receiver diagram, assembled from off-the-shelf discrete components. Compared with the simplified version in Figure 3.20, much detail has been added.

From the top left side, the vector signal generator generates a single-tone carrier, which is split into two separate paths. The upper path goes directly to a SPDT (single pole double throw) switch ZYSWA; the lower path is first attenuated then amplified by a PA (power amplifier). The switch's output is therefore a signal alternating between two levels of amplitude, corresponding to the system's two-phase operation. In the center of the diagram, there is a pulse generator, controlling the polarity of the ZYSWA switch. To the right of the switch is the self jammer cancellation readily introduced in Figure 3.20.

Continuing in Figure 4.6, when the carrier signal is reflected back by the transmitter, it returns through the antenna on the top right corner. After the matching network, circulator and hybrid power combiner, the received signal reaches another SPDT switch, controlled by the same pulse generator in the center. The purpose of this second switch is to prevent the LNA (low noise amplifiers) from saturating at the power phase. Subsequently through a limiter (for protection), LNA and an anti-aliasing filter, the received signal is sampled by a high-speed digital oscilloscope, serving the function of data acquisition in

this particular design. Numeric data output from the oscilloscope are finally processed in MATLab using simple energy detection (illustrated in Figure 4.7) in search for actual pulse positions.

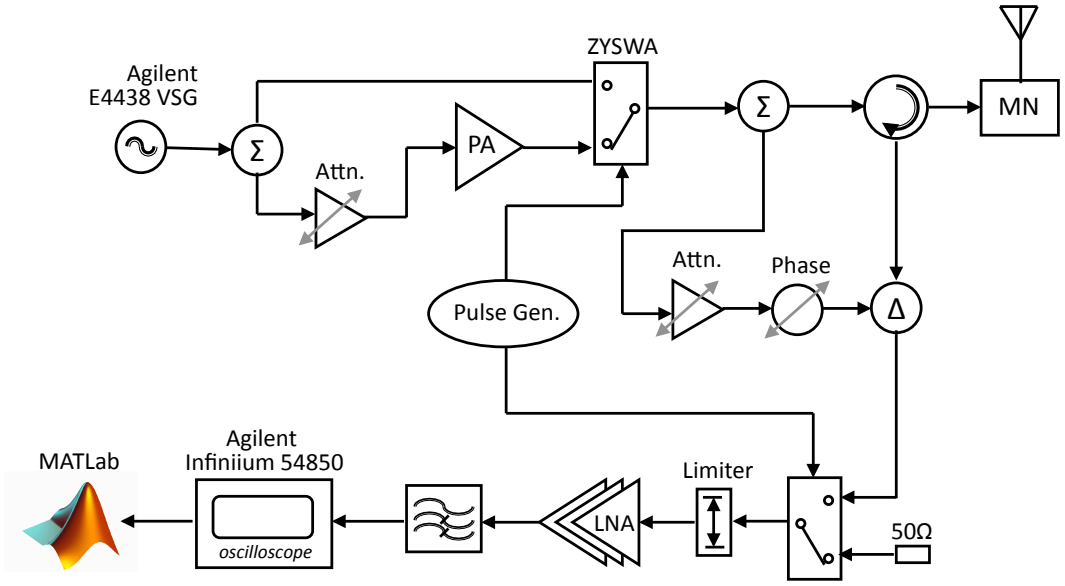

Figure 4.6: Reflective Impulse Receiver Diagram

Obviously the receiver in Figure 4.6 is not intended for use in the portable neural application envisioned in Figure 1.1. Rather it serves as a test bench for evaluating the transmitter. On the other hand, experience gained from designing this prototype system provides valuable reference for those that endeavor to redesign the receiver in a form factor and power profile suitable for portable applications. These experiences (and lessons learnt) will be reported towards the end of this chapter.

4.3.2 Functional Test

For functional testing purposes, additional circuits (drivers with a separate supply rail) were included in the neural transponder chip. Figure 4.8 shows the

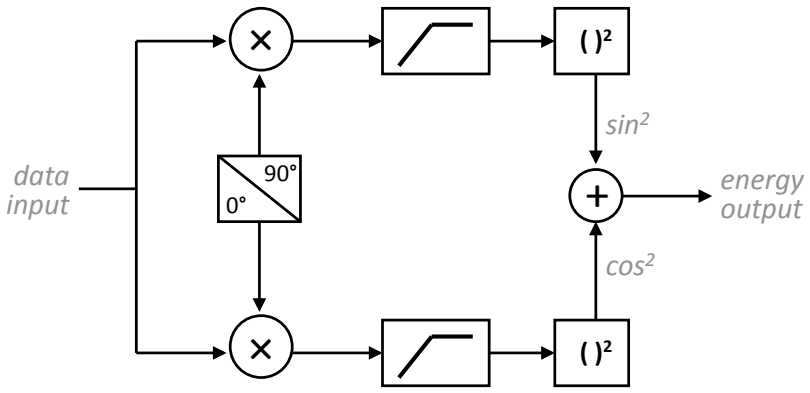

Figure 4.7: Pulse Decoder Algorithm

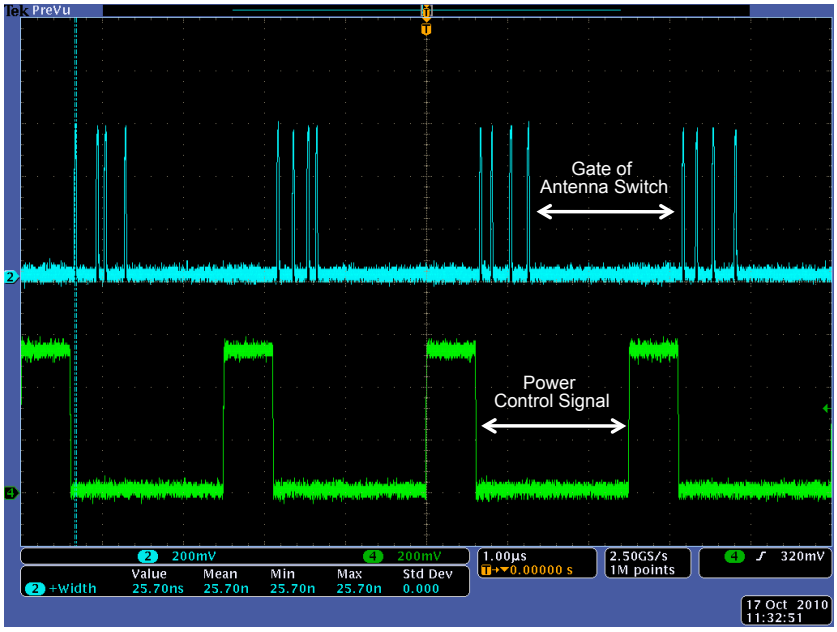

Figure 4.8: Waveforms from Direct Transmitter Measurement

waveforms measured at the gate of the antenna switch (top light blue trace). The bottom green trace is the output of the pulse generator in Figure 4.6. When it is high, the system is in the power phase; when it becomes low, the system enters the communication phase. As expected from Figures 3.13 and 4.2, there exist four pulses to the antenna switch within each communication phase. The first and third pulses are beacons; the second and fourth are data. A closer inspection will reveal that the beacons occupy a fixed position with respect to the falling edge of the power control signal. Data pulses on the other hand have variable positions, where base-band information is encoded.

There is however one difference. In Figures 3.13 and 4.2, the antenna pulses spread across the entire duration of the communication phase. In Figure 4.8, they seem to exist in only the early half. The reason for this difference is process and voltage variations. The transponder was designed such that the pulses would take up the entire duration at the slowest process corner and lowest supply voltage. The device measured for Figure 4.8 is under somewhat typical condition with a nominal supply. Therefore its pulses are shorter and they finish earlier.

To reveal further details about the beacon and data pulses, more waveforms were taken with the oscilloscope in the continuous trigger mode (Figure 4.9). What is shown is hence an overlay of a large number of captures at various time instances. It now becomes evident that the two beacons indeed always occupy a fixed position. Any data pulse on the other hand can take up one of the seven positions evenly and successively spaced, where the actual position is determined by the base-band output from the 3-stage LFSR in Figure 4.4 (a 3-stage LFSR generates seven, instead of eight, pseudo-random numbers because the all-0 case would result in a deadlock and is thus disallowed).

Let us now compare the waveforms in Figure 4.9 with what is captured from actual radio tests. Figure 4.10 shows the overlay of multiple outputs from the MATLab decoder, colored for different time instances. The over-the-air test was carried out with about 1 mm distance between the transmit and receive antennas. Identical to Figure 4.9, all beacon pulses collapse to a fixed position; data pulses on the other hand spread across seven successive time slots. The time scale in Figures 4.9 and 4.10 also matches. In summary: **the basic function of the reflective impulse radio is proven.**

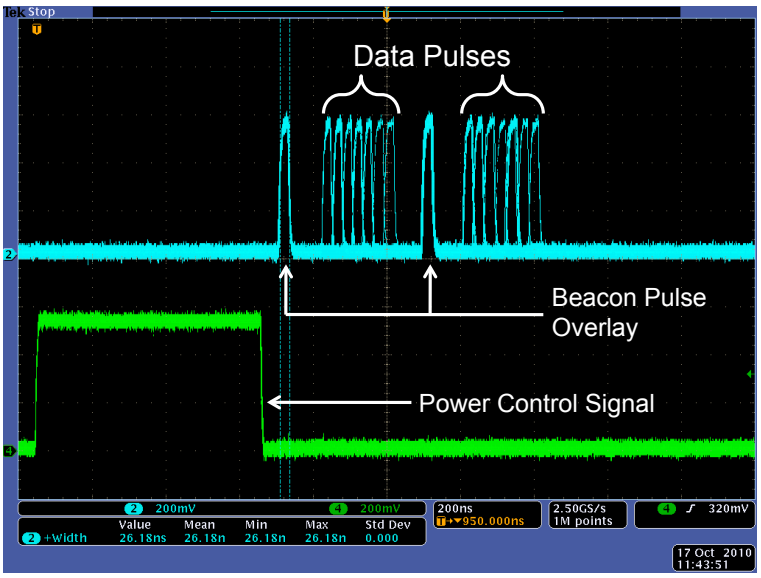

Figure 4.9: Overlay of Pulse Waveforms

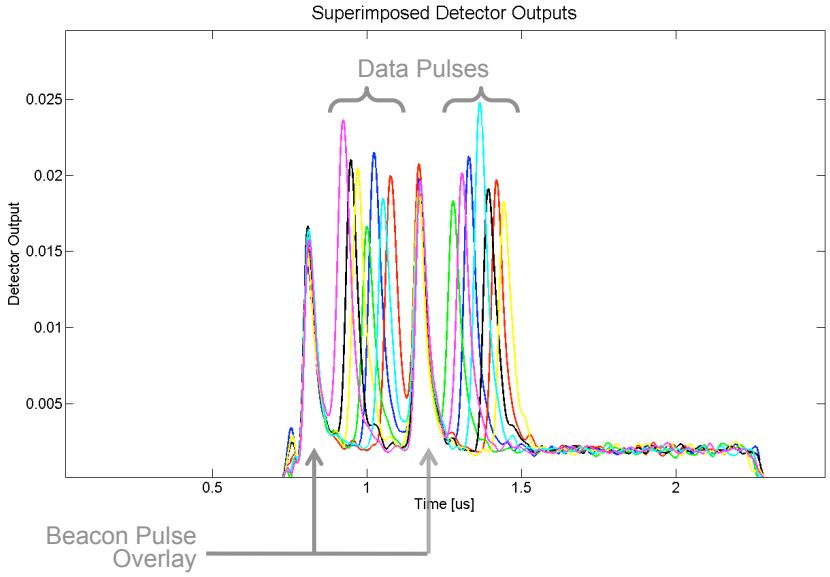

Figure 4.10: Pulses Received in Over-the-Air Test

Despite the matched time scale and pulse positions, there is a noticeable difference between the two figures. In Figure 4.9, the pulses have sharp rising and falling edges, with little overlap between neighboring pulses. In Figure 4.10 however, the rise and fall are rather gentle; adjacent data pulses also overlap at the base. This difference is caused by the fact that the bandwidth of the receiver front-end is narrower than the transmitted (reflected) pulses. So when the broad-band signal reaches the receive antenna and matching network in Figure 4.6, its sharp edge becomes gentle and its pulse width extends, causing certain degree of inter-symbol interference (ISI). The obvious solution is of course to redesign and broaden the receiver's bandwidth.

4.3.3 Range Test

With its basic function verified, the next step is to test the new radio's communication range. However the actual test was limited by low yield of chip packaging — out of eight packaged devices, only two were functional. The other six were either broken or with severe performance degradation. The cause for this low yield was traced down to poor quality in flip-chip packaging. The contact resistance between the micro-PCB antenna and the IC chip was 2-3 orders of magnitude higher than industry standard [13], which in turn caused substantial loss in antenna efficiency and reduction in modulation depth. Nevertheless, as many as possible tests were still carried out with the two remaining devices. The first device was used for power back-off test, an indirect measure of communication range, before it was damaged too; the second device was used for direct range measurement.

Figure 4.11 shows the setup for power back-off test, where the communication distance is fixed at about 1 mm. To keep the transponder powered at the proper level, the reader's radiation power is kept constant during the power phase. However the power level during the communication phase is allowed to vary. There are obviously two boundaries to this variable power. On one hand, it cannot be too high; or the synchronizer will fail to detect the transition from the power to the communication phase. On the other hand, it cannot be too low to bury the weakened reflected signal in total noise. Finding these two boundaries, especially the second one, is the purpose of this power back-off test.

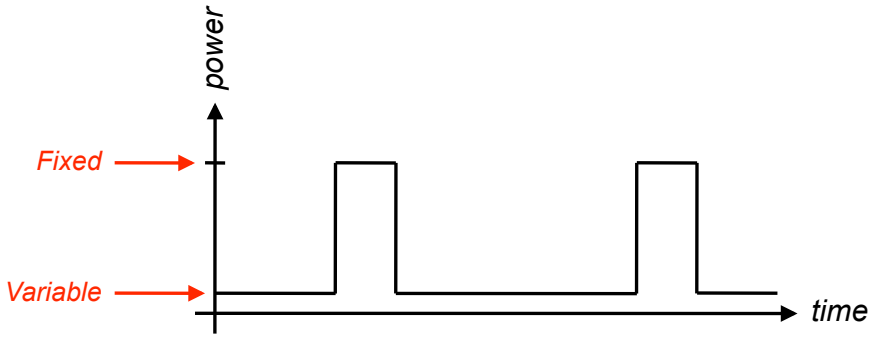

Figure 4.11: Setup for Power Back-off Test

Results from the power back-off test are shown in Figure 4.12. Output from the receiver decoder is plotted at each power back-off level. As can be seen, the pattern of a single beacon overlay followed by seven consecutive data positions is clearly identifiable when the power of the communication phase is only 10dB (the synchronizer threshold) below that of the power phase. When the power back-off level increases, above pattern becomes less distinctive. At 33dB, the last two data pulses collide into each other, although still discernible. At 35dB, separation between the last two pulses vanishes. It is therefore reasonable to conclude, although somewhat subjectively, that the upper bound of power back-off is 33dB. This upper bound can be potentially pushed higher with a broader-band receiver as it alleviates the ISI symptom clearly visible in Figure 4.12.

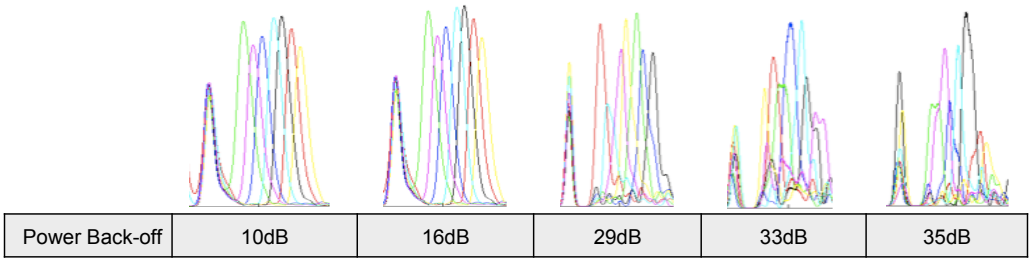

Figure 4.12: Receiver Decoder Output at Various Power Back-off Levels

Figure 4.13 illustrates the direct range test in the air. At each distance, the reader's radiation power is adjusted to properly power the transponder. The power back-off level on the other hand is kept at 12dB, the synchronizer threshold of the second test device.

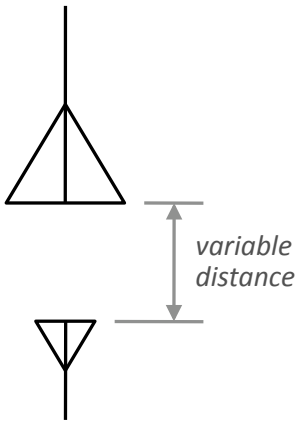

Figure 4.13: Setup for Direct Range Test

Results from direct range test are shown in Figure 4.14. Note that the pulses are now negative, in the form of valleys instead of peaks in their amplitude. At 5mm distance, the pattern of a beacon (in the middle of the chart) followed by seven data pulses is clear. At 13mm however, the pattern becomes barely discernible. The communication range of this second device is therefore about 13mm.

Finally Figure 4.15 plots the communication distance and the reader's output power for both devices tested above. "Sample 1" was the one used for power back-off test; "Sample 2" was for direct range test, which, as reported previously, demonstrated communication distance of up to 13mm. When put to direct range test, the first sample was actually able to communicate with less power from the reader than the second sample (the blue curve is 3-6 dB below the red curve). This difference was later attributed to different antenna-chip contact resistance between these two devices. What was unfortunate however was that the first sample was accidentally damaged in the middle of this direct

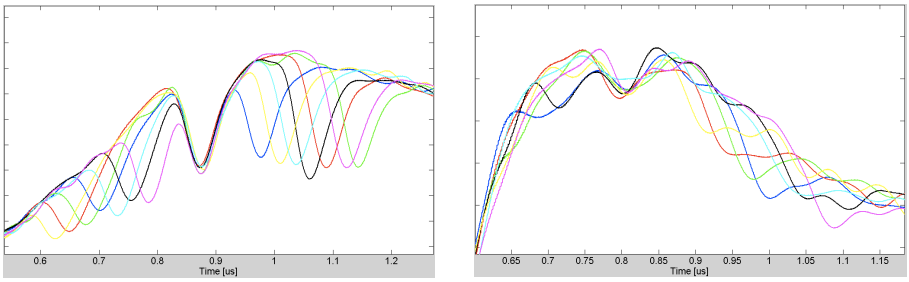

Figure 4.14: Receiver Decoder Output at Various Communication Distance

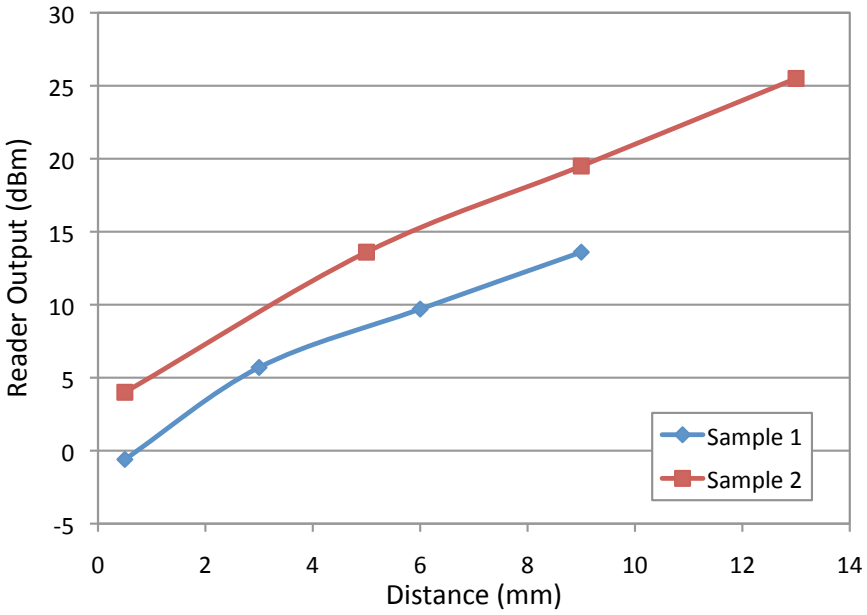

Figure 4.15: Communication Distance vs. Reader Output Power

range test when the receiver data pattern was still clearly discernible at 9mm distance. Otherwise, as shown in the trajectory in Figure 4.15, the device could have communicated over the air at 16mm or even longer distance.

4.3.4 Energy Efficiency Test

The key promise of a reflective impulse transmitter is its energy efficiency. While its absolute power consumption may not be as low as RFID, its data rate should be substantially higher. Likewise, while its data rate may not be as high as UWB, it should consume far less power. In other words, the energy per bit (power divided by data rate) of the new radio transmitter should be the lowest among the three.

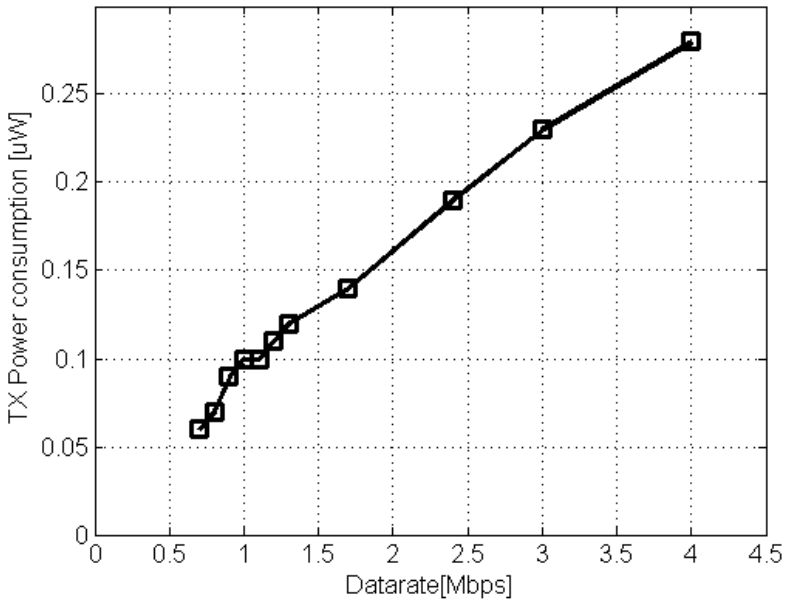

Figure 4.16: Transmitter Power Consumption vs. Data Rate

Figure 4.16 shows the measured circuit power of the neural transmitter with its data rate ranging from 700kbps to 4Mbps. The lower bound of the data rate is set by the maximum output power of the HP83732A Synthesized Signal Generator, because when data rate decreases the duty cycle of powering also diminishes, requiring higher output power from the signal generator during the power phase. The upper bound of 4Mbps, on the other hand, is limited by the maximum pulse modulation frequency of the HP83732A. The maximum data

rate could otherwise be 6.5 to 7 Mbps, as results in Figures 4.8, 4.9 and 4.10 clearly show that all data pulses are transmitted within a time window of 700ns. Adding an additional 25% time margin for the powering phase, the equivalent maximum data rate is 6.9Mbps. For applications that desire even higher data rate, the pulse generator circuit of the transmitter needs to be re-designed to support narrower pulse width.

Two observations can be made from Figure 4.16. First the circuit power consumption of the transmitter is below 300 nW, a new record for the neural application or any application requiring similar throughput. Second, the relationship between power consumption and data rate is fairly linear, demonstrating the promised scalability in Chapter 2.

While the results in Figure 4.16 indeed look encouraging, they include only the circuit power. What needs to be added to the total power consumption is the "hidden power" defined in Chapter 2. As an example, Figure 4.17 shows the reader power profile of the experiment in Figure 4.11 (for the case of 18dB power back-off). The average radiation power has been scaled up to 56mW, a limit set by health and safety regulations [43]. It is also reported that total power generated from this two phase operation is 8.1μW, with 2.5μW consumed by the regulator itself and an excess 5.6μW for the transmitter and other circuits powered by the regulator [13, 43].

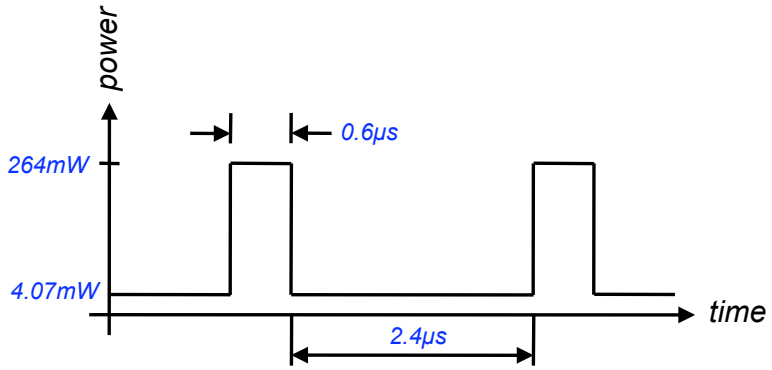

Figure 4.17: Reader Power Profile Example

Given above data points, computing the "hidden power" is straightforward. The amount of energy used for generating the 8.1μW power is

$$264mW \times 0.6\mu s = 158.4nJ$$

The amount of energy "wasted" during the communication phase is

$$4.07mW \times 2.4\mu s = 9.77nJ$$

Therefore if the energy during the communication phase were used for power rectification, it would have generated

$$8.1\mu W \times \frac{9.77nJ}{158.4nJ} = 500nW$$

So the hidden power is 500nW.

Adding above hidden power to the circuit power in Figure 4.16, total power consumption of the reflective impulse transmitter is 660nW for 2Mbps, still several orders of magnitude lower than the state of the art.

Table 4.1 summarizes the performance of the new transmitter in the context of other designs for the neural application. Not only is the whole transponder's area reduced by more than 20 times, it also achieves the highest data rate per area. Moreover total power consumption by the transmitter is reduced by over 1,000 time. Even on the energy per bit basis, the improvement is more than 50 times.

4.4 Future Improvement

While the new radio demonstrated record level of performance in over-the-air tests, unfortunately large animal (porcine) tests were not successful. The main reason was low yield and poor quality of flip-chip packaging. As reported previously, only two out of eight samples were functional. Furthermore, between the two remaining devices, one was also damaged during the range test and the other displayed higher than expected flip-chip contact resistance. It is therefore quite obvious that ***packaging*** is where much improvement is

Reference	**[44]**	**[45]**	**[46]**	**This Work**
Technology	0.6μm BiCMOS	0.13μm CMOS	0.35μm CMOS	**65nm CMOS**
Size (mm^2)	$>$ 5×5	10×15	8.8×7.2	**1.1×1.1**
TX Power	720μW	not stated	1.6mW	**660nW**
DataRate/mm^2	13.8kbps	<5.3kbps	1.4Mbps	**2Mbps**
Energy/bit	2.1nJ	not stated	18pJ	**330fJ**
Off-Chip	antenna+capacitor	antenna	antenna+clock	**antenna**
Verification	in vivo (cat)	air	ex vivo (snail)	**air**

Table 4.1: Comparison with State-of-the-Art Neural Transmitters

needed. Limited availability of functional devices also prevented us from testing in smaller size animals (e.g. rats or cats), even though they represented much better chance of success than pigs.

Besides packaging, there are several other areas where future improvements are desirable.

(1) Phase Noise

Analyzed in Chapter 3, the problem of phase noise is caused by self interference. There exist several options to address this problem. First, improving the (pedestal) phase noise of the signal source itself and that of the power amplifier will have a direct impact on overall SNR performance. Second, multiple interference cancellation loops, when possible at all with integrated implementations, can potentially identify noise signature from each interference path and provide more effective phase noise cancellation. The third option is the extension of the receiver bandwidth, the very next topic for discussion.

(2) Receiver Bandwidth

In the current receiver implementation, the bandwidth of the matching net-

work is substantially narrower than that of the reflected signal. Consequently, there is not only loss of signal energy, but also spectral distortion of the phase noise, degrading the overall SNR twice. The fundamental reason for the bandwidth limitation is the high impedance ratio between the two ports of the matching network. If that ratio can be reduced via a custom circulator of non-standard impedance or other devices like a transformer, the receiver bandwidth will expand and performance improvement can be gained, again twice.

(3) Decoder Algorithm

In its current implementation, the receiver uses an energy detection algorithm to locate the pulses (Figure 4.7). Although simple, it has substantial room for improvement too. Figure 4.18(a) illustrates the current algorithm on a Smith Chart. The two blue vectors represent the reflection coefficients of the transmitter antenna when the antenna switch is on and off respectively. What the energy detector detects then is the difference in amplitude between the blue vectors, shown as a new red arrow in the Chart. Imagine on the other hand that there exists an alternative scheme that detects not only the amplitude difference but also the phase difference between the blue vectors. The

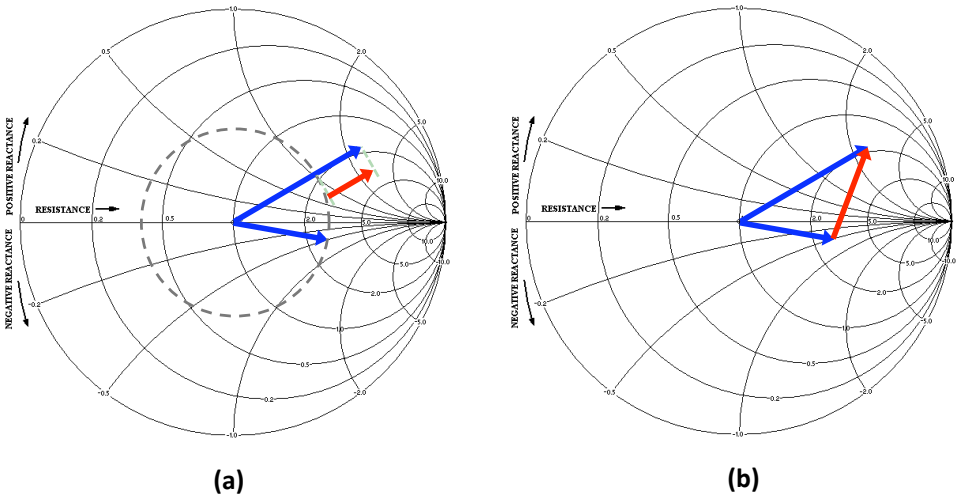

Figure 4.18: Decoder Algorithm Current vs. Ideal

result is shown Figure 4.18(b). Apparently the red arrow in (b) is longer than that in (a), demonstrating that with same reflections from the transmitter the alternative decoder algorithm can recover a stronger signal than the current implementation.

With all above improvements, the purpose is to increase the SNR by either suppressing the noise, enhancing the signal, or both. Obviously the larger the SNR, the better possibility that tests in large animals will succeed, a critical milestone towards actual application in human patients. But the most immediate challenge that needs to be addressed is again the quality of flip-chip packaging.

Chapter 5

Conclusion

Over the history of civilization, communication has evolved to be a major part of our life. A 1972 survey for example reported that office workers (professional, technical, administrative, and clerical) spent 50–80% of their work time communicating, all before the introduction of email or cellphones in regular workplaces [47]. Communication has essentially become how we are perceived as a person, as a society, and as a civilization in its thousands of years' evolution.

While 100 years may appear brief in the scale of history, wireless communication has surely made profound changes to our life since its invention about a century ago. Today, there are already over 5 billion cellphone subscribers in this world of 6.9 billion population [48]. Many smart phones are equipped with not only cellular connectivity but also Wi-Fi, Bluetooth, and GPS. Besides cellphones, laptops and other consumer electronics, applications such as machine-to-machine, RFID tracking, and wireless sensor networks have also emerged. It no longer comes as a surprise that there will be 1 trillion connected devices on the surface of the earth, soon [49].

The vision of pervasive and ubiquitous connectivity underlines the quest for ever smaller radios that consume ever lower power. This thesis provides one such data point — mm^3 in size, μW in power with Mbps type of capability.

It is enabled by first realizing the inherent link asymmetry in a class of sensor network applications then combining the operating principles of RFID and UWB. The powerful combination of low power consumption and high data rate allows the **Reflective Impulse Radio** to achieve a record level of energy efficiency.

Let us now pause for a moment and extrapolate to the extremes of above quest — what is the physical limit to size miniaturization? Can there be microscopic transmitters that consume 0 power? Before answering these questions, one should first realize that size is actually part of the power consumption question. Most radios, including the one presented in this thesis, are limited by the size of the antenna. While a sizable antenna does perform better, there is no limit to its downsizing other than the continuous sacrifice of its radiation efficiency. In other words, as long as the transmitter can afford the power, its size is not the constraint.

With respect to power, there is of course the Shannon limit. The transmitter has to transmit signals with sufficient energy to overcome noise. This limit however no longer holds for reflection based passive transmitters, like the Reflective Impulse Radio, where the signal energy is essentially transmitted by the receiver. What the transmitter consumes then is the power needed to modulate the reflection of the antenna, which in theory can be much lower than the Shannon limit. Moreover, it also allows the transmitter to benefit from technology scaling as well as from future technologies utterly different from CMOS [50].

While this chapter and this thesis have to end here, the quest for ever smaller and ever lower-power radios has just begun. Let us conclude by another extrapolative example in Figure 5.1 (Courtesy of Zettl Research Group, Lawrence Berkeley National Laboratory and University of California at Berkeley). When one day the radios are tiny enough to ride on a single blood cell and efficient enough to live off its ambient, the world where we live and our civilization thrives will be once again, vastly different.

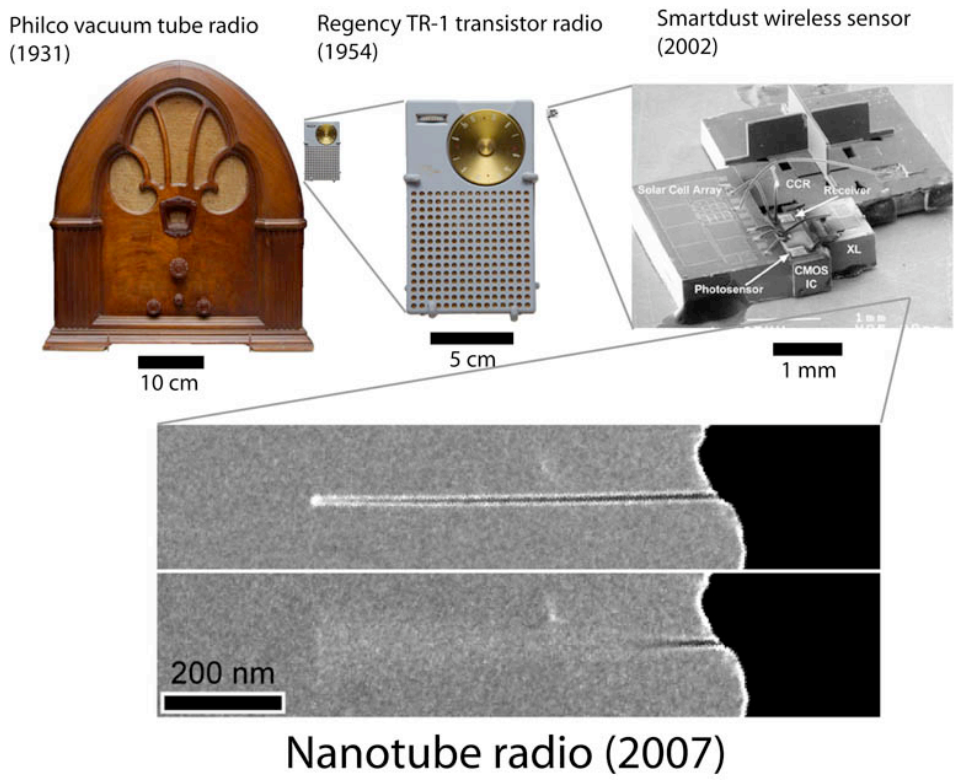

Figure 5.1: Progression of Radio: Timeline and Size Comparison [51]

Bibliography

[1] A. L. Nobunga, B. K. Go, R. B. Karunas, "Recent Demographic and Injury Trends in People Served by the Model Spinal Cord Injury Care Systems," *Arch Phys Med Rehabil*, vol. 80, pp. 1372–1382, 1999

[2] M. A. L. Nicolelis, "Brainmachine interfaces to restore motor function and probe," *Nature Reviews Neuroscience*, vol. 4, pp. 417–422, 2003

[3] E. M. Schmidt, "Single neuron recording from motor cortex as a possible source of signals for control of external devices," *Annals of Biomedical Engineering*, vol. 8, pp. 339–349, 1980

[4] J. M. Carmena, et al. "Learning to Control a BrainMachine Interface for Reaching and Grasping by Primates," *PLoS Biology*, vol. 1, pp. 001–016, 2003

[5] L. R. Hochberg, et al. "Neuronal ensemble control of prosthetic devices by a human with tetraplegia," *Nature*, vol. 442, pp. 164–171, 2006

[6] G. Santhanam, et al. "A high-performance braincomputer interface," *Nature*, vol. 442, pp. 195–198, 2006

[7] M. A. Lebedev, M. A. L. Nicolelis, "Brainmachine interfaces: past, present and future," *TRENDS in Neuroscience*, vol. 29, pp. 536–546, 2006

[8] J. N. Turner, et al. "Cerebral Astrocyte Response to Micromachined Silicon Implants," *Experimental Neurology*, vol. 156, pp. 33–49, 1999

[9] R. R. Harrison, et al. "A Low-Power Integrated Circuit for a Wireless 100-Electrode Neural Recording System," *IEEE Journal of Solid-State Circuits*, vol. 42, pp. 123–133, 2007

[10] R. Yu, K. Najafi, "Low-Power Interface Circuits for Bio-Implantable Microsystems," *Proceedings of IEEE International Solid-State Circuits Conference*, 2003

[11] M. Rizk, I. Obeid, S. H. Callender, P. D. Wolf, "A single-chip signal processing and telemetry engine for an implantable 96-channel neural data acquisition system," *Journal of Neural Engineering*, vol. 4, pp. 309–321, 2007

[12] M. Chae, et al. "A 128-Channel 6mW Wireless Neural Recording IC with On-the-Fly Spike Sorting and UWB Transmitter," *Proceedings of IEEE International Solid-State Circuits Conference*, 2008

[13] Michael Mark, *Powering mm-Size Wireless Implants for Brain-Machine Interfaces*, PhD Dissertation, University of California, Berkeley, 2010

[14] R. H. Olsson III, K. D. Wise, "A Three-Dimensional Neural Recording Microsystem with Implantable Data Compression Circuitry," *IEEE Journal of Solid-State Circuits*, vol. 40, pp. 2796–2804, 2005

[15] S. Borenstein, M. Jaske, A. Rosenfeld, "Dynamic pricing, advanced metering, and demand response in electricity markets, center for the study of energy markets," *White Paper*, 2002

[16] A. Faruqui, J. Hughes, M. Mauldin, "Real-time Pricing in California R&D Issues and Needs," *Report for the California Energy Commission*, 2002

[17] S. Ergen, et al. "The tire as an intelligent sensor," *IEEE Transactions on Computer-Aided Design of Integrated Circuits and Systems*, vol. 28, pp. 941–955, 2009

[18] K. Finkenzeller, *RFID Handbook: Fundamentals and Applications in Contactless Smart Cards and Identification*, John Wiley & Sons, 2003

[19] *Wikipedia*, http://en.wikipedia.org/wiki/Spark-gap_transmitter

[20] J. G. Proakis, *Digital Communication*, 4th edition, McGraw-Hill, 2001

[21] P. V. Nikitin, K. V. S. Rao, "Antennas and Propgagation in UHF RFID Systems," *Proceedings of 2008 IEEE International Conference on RFID*, 2008

[22] M. Sasaki, "A 12-mW 500-Mb/s 1.8-μm CMOS Pulsed UWB Transceiver Suitable for Sub-meter Short-range Wireless Communication," *Proceedings of 2008 IEEE Radio Frequency Integrated Circuits Symposium*, pp. 593–596, 2008

[23] T. Terada, et al. "A CMOS Ultra-Wideband Impulse Radio Transceiver for 1-Mb/s Data Communications and 2.5-cm Range Finding," *IEEE Journal of Solid-State Circuits*, vol. 41, pp. 891–898, 2006

[24] G. Mazurek, J. Szabatin, "Code-division multiple-access protocol for active RFID systems," *Proceedings of SPIE, the International Society for Optical Engineering*, Society of Photo-Optical Instrumentation Engineers, pp. 69373W-1, 2007

[25] G. Mazurek, "Active RFID System With Spread-Spectrum Transmission," *IEEE Transactions on Automation Science adn Engineering*, vol. 6, no. 1, pp. 25–32, 2009

[26] A. Loeffler, F. Schuh, H. Gerhaeuser, "Realization of a CDMA-based RFID System Using a Semi-active UHF Transponder," *Proceedings of the 2010 6th International Conference on Wireless and Mobile Communications*, pp. 5–10, 2010

[27] R. G. Gallager, *Principles of Digital Communication*, Cambridge University Press, 2008

[28] Steven D. Keller, *Design and Development of Directly-Modulated Antennas Using High-Speed Switching Devices*, PhD Dissertation, Duke University, 2008

[29] S. D. Keller, W. D. Palmer, W. T. Joines, "Direct antenna modulation: analysis, design, and experiment," *Proceedings of 2006 IEEE Antennas and Propagation Society International Symposium*, pp. 909–912, 2006

[30] W. Yao, Y. Wang, "Direct antenna modulation — a promise for ultra-wideband (UWB) transmitting," *Proceedings of 2004 IEEE MTT-S International Microwave Symposium Digest*, pp. 1273–1276, 2004

[31] J. M. Rabaey, A. Chandrakasan, B. Nikolić, *Digital Integrated Circuits*, 2nd Edition, Prentice-Hall, Upper Saddle River, NJ, 2003

[32] *EPCglobal*, http://www.epcglobalinc.org/tech/freq_reg/RFID_at_UHF_Regulations_20090318.pdf

[33] *FCC Rules and Regulations, Code of Federal Regulations Title 47, Part 15 Radio Frequency Devices*,http://wireless.fcc.gov/index.htm?job=rules_and_regulations

[34] *FCC Report and Order on Ultra-Wideband Transmission Systems*, http://hraunfoss.fcc.gov/edocs_public/attachmatch/FCC-02-48A1.pdf, February 14, 2002

[35] *EECS121 Introduction to Digital Communications*, University of California Berkeley, Spring 2008

[36] M. Mark, et al. "Wireless Channel Characterization for mm-size Neural Implants," *Proceedings of IEEE Engineering in Medical and Biological Society International Conference*, pp. 1565–1568, 2010

[37] B. C. Henderson, J. A. Cook, "Image-Reject and Single-Sideband Mixers," *Watkins-Johnson Company*, WJ Tech-note, vol. 12, no. 3 May/June, 1985

[38] *Avago FBAR Filters*, http://www.avagotech.com/pages/en/rf_microwave/fbar_filters/

[39] S. Lee, C. Nguyen, "Mechanically-coupled micromechanical resonator arrays for improved phase noise," *Proceedings of 2004 IEEE Intl. Frequency Control Symp. and Exhibition*, pp. 144–150, 2004

[40] J. M. Rabaey, et al. "Powering and Communicating with mm-size Implants," *Proceedings of DATE Design, Automation & Test in Europe*, 2011

[41] *FCC Rules and Regulations, Code of Federal Regulations Title 47, 1.1307(b), 2.1091, 2.1093*, http://wireless.fcc.gov/index.htm?job=rules_and_regulations

[42] *IEEE Standard for Safety Levels with Respect to Human Exposure to Radio Frequency Electromagnetic Fields, 3 kHz to 300 GHz*, IEEE Std C95.1, 2005

[43] M. Mark, et al, "A 1mm^3 2Mbps 330fJ/b Transponder for Implanted Neural Sensors," *Proceedings of Symposia on VLSI Technology and Circuits*, 2011

[44] R. R. Harrison, et al. "Wireless Neural Recording With Single Low-Power Integrated Circuit," *IEEE Transactions on Neural Systems and Rehabilitation Engineering*, vol. 17, no. 4, pp. 322–329, 2009

[45] Z. Xiao, C-M. Tang, C. M. Dougherty, R. Bashirullah, "A 20μW Neural Recording Tag with Supply-Current-Modulated AFE in 0.13μm CMOS," *Proceedings of IEEE International Solid-State Circuits Conference*, 2010

[46] M. S. Chae, Z. Yang, M. R. Yuce, L. Hoang, W. Liu, "A 128-Channel 6 mW Wireless Neural Recording IC with Spike Feature Extraction and UWB Transmitter," *IEEE Transactions on Neural Systems and Rehabilitation Engineering*, vol. 17, no. 4, pp. 312–321, 2009

[47] E. T. Klemmer, F. W. Snyder, "Measurement of Time Spent Communicating," *Journal of Communication*, vol. 22, issue 2, pp. 142–158, June 1972

[48] *Wikipedia*, http://en.wikipedia.org/wiki/List_of_countries_by_number_of_mobile_phones_in_use

[49] "A World of Connections," *The Economist*, April 26th, 2007

[50] F. Chen, et al. "Demonstration of Integrated Micro-Electro-Mechanical Switch Circuits for VLSI Applications," *Proceedings of IEEE International Solid-State Circuits Conference*, 2010

[51] *Nanotube Radio: Supplementary materials*, http://www.physics.berkeley.edu/research/zettl/projects/nanoradio/radio.html